# I. REACTIVELY SPUTTERED Ti-Si-N THIN FILMS FOR DIFFUSION BARRIER APPLICATIONS

# II. OXIDATION, DIFFUSION AND CRYSTALLIZATION OF AN AMORPHOUS $Zr_{60}Al_{15}Ni_{25}$ ALLOY

Thesis by

Xin Sun

In Partial Fulfillment of the Requirements

for the Degree of

Doctor of Philosophy

California Institute of Technology

Pasadena, California

1997

(Defended October 2, 1996)

© 1997

Xin Sun

All Rights Reserved

# Table of Contents


**Acknowledgments** vi

**Abstract** viii

**I. Reactively Sputtered Ti-Si-N Thin Films for Diffusion Barrier Applications**

Chapter 1 Introduction 1

Chapter 2 Synthesis and Properties of Ti-Si-N Thin Films 10

2.1 Deposition and experimental procedures 10

2.2 Composition of the films 12

2.3 Microstructure 15

2.3.1 Planar structure and crystallization 15

a. $TiSi_2$ target 15

b. $Ti_5Si_3$ target 17

c. $Ti_3Si$ target 19

2.3.2 Film texture and grain orientation 20

2.3.3 Discussion 22

2.4 Atomic density 24

2.5 Room temperature resistivity 26

2.5.1 General results 26

2.5.2 Effect of annealing 28

2.6 Temperature dependence of resistivity 31

2.6.1 Measurement procedures 31

2.6.2 Results 32

2.6.3 Discussion 33

2.7 Reactive ion etching 34

2.8 Conclusion 35

Chapter 3 Ti-Si-N Thin Films as Diffusion Barriers Between Si and Al 64

3.1 Experimental procedures 64

3.2 Results 65

3.2.1 Films from the $Ti_5Si_3$ target 65

3.2.2 Films from the $TiSi_2$ target 68

3.2.3 Films from the $Ti_3Si$ target 69

3.3 Discussion 70

3.4 Conclusion 72

Chapter 4 Ti-Si-N Thin Films as Diffusion Barriers Between Si and Cu 82

4.1 Experimental procedures 82

4.2 Results 83

4.2.1 Films from the $Ti_5Si_3$ target 83

4.2.2 Films from the $TiSi_2$ target 85

4.2.3 Films from the $Ti_3Si$ target 87

4.3 Discussion 88

4.3.1 General comments 88

4.3.2 Ti-Si films 89

4.3.3 Ti-Si-N films 90

4.3.4 Composition selection for an optimized diffusion barrier 91

4.4 Conclusion 93

## II. Oxidation, Diffusion and Crystallization of an Amorphous $Zr_{60}Al_{15}N_{25}$ Alloy


1. Introduction 108
2. Experimental procedures 110
3. Oxidation between 310 and 390 °C 111
   - 3.1 Oxide composition and growth law at 370 °C, with kinetic modeling 111
   - 3.2 Activation energy of growth process from 310 to 390 °C 117
4. Oxidation at 410 °C and above 118
   - 4.1 Oxidation at 410 °C 118
   - 4.2 Oxidation at 430 °C 120
   - 4.3 Oxidation at 450 °C 120
5. Oxidation at 290 °C and below 121
6. Remarks on preferential oxidation 121
7. Oxidation of $Zr_{72.5}Al_{15}Ni_{12.5}$ at 330 °C 124
8. Conclusion 125

## Acknowledgments

First and foremost, I would like to thank my advisor, Prof. Marc. A. Nicolet, for his support and guidance. This thesis is made possible through his efforts. I have benefited enormously from his scientific disposition towards research, his abundance of knowledge, and his resourcefulness in ideas.

I am especially indebted to Dr. Elzbieta Kolawa. She had introduced me to the research of ternary diffusion barriers, which constitutes the major part of my thesis. She never hesitated to contribute ideas and offer help in case of difficulties. Her rich knowledge and experience are always my resource.

I owe thanks to many people who helped me in one way or another during my graduate years at Caltech. Prof. Johnson had initiated the project of the oxidation of Zr-Al-Ni metallic glasses, together with Prof. Nicolet, which led to the second part of this thesis. Drs. Susan and Uli Geyer are my close collaborators on this project. I will always remember their assistance and friendship.

Carol Garland has kept a very enjoyable environment in the transmission electron microscopy lab. She was always there for help whenever I needed assistance in sample preparation and imaging. She especially went through all the steps helping me prepare a hard-to-make cross-sectional sample out of which came beautiful photos (Fig. 2.13). Ron Ruiz at Jet Propulsion Laboratory helped me with scanning electron microscopy imaging, which contributes significantly to this thesis.

Other collaborators who deserve thanks are George Mclane at Army Research Office who carried out reactive ion etching experiment, and Ken Ellis at Cornell University who did the x-ray photoelectron spectroscopy study on a Ti-Si-N film, through the introduction of Dr. David Lilienfeld. Dr. Paula Grunthaner at Jet Propulsion Laboratory had taken her time assisting me analyzing the x-ray photoelectron spectrum. Technical supports from Rob Gorris and Mike Easterbrook at Caltech are gratefully acknowledged.

Many of the groupmembers had enriched my stay at Caltech with their assistance and friendship. They are Jen-Sue Chen, Jason Reid, Wen-Shu Liu, Segoen Park, Andreas Bächli, Stefan Gasser, Seongil Im and Thorsten Kacsich. Thank you.

The Army Research Office provided most of the financial support for the work I report here. Dr. John Prater, of that office, deserves to be mentioned and thanked here particularly. Without his farsightedness, interest and perseverance, neither this thesis, nor the development of the highly successful ternary amorphous transition metal-Si-N films would now exist.

I am grateful to my parents and my grandma for their blessing, their support and their encouragement, which accompany me during the preparation and writing of this thesis.

Finally, I want to thank my husband, Chuan Xie, for his unconditional love and support, care and patience. This thesis is dedicated to him.

## Abstract

Films of Ti-Si-N obtained by reactively sputtering a $TiSi_2$, a $Ti_5Si_3$, or a $Ti_3Si$ target are either amorphous or nanocrystalline in structure. The atomic density of some films exceeds $10^{23}$ at./cm$^3$. The room-temperature resistivity of the films increases with the Si and the N content. A thermal treatment in vacuum at 700 °C for 1 hour decreases the resistivity of the Ti-rich films deposited from the $Ti_5Si_3$ or the $Ti_3Si$ target, but increases that of the Si-rich films deposited from the $TiSi_2$ target when the nitrogen content exceeds about 30 at. %.

$Ti_{34}Si_{23}N_{43}$ deposited from the $Ti_5Si_3$ target is an excellent diffusion barrier between Si and Cu. This film is a mixture of nanocrystalline TiN and amorphous $SiN_x$. Resistivity measurement from 80 K to 1073 K reveals that this film is electrically semiconductor-like as-deposited, and that it becomes metal-like after an hour annealing at 1000 °C in vacuum. A film of about 100 nm thick, with a resistivity of 660 μΩcm, maintains the stability of Si $n^+p$ shallow junction diodes with a 400 nm Cu overlayer up to 850 °C upon 30 min vacuum annealing. When used between Si and Al, the maximum temperature of stability is 550 °C for 30 min. This film can be etched in a $CF_4/O_2$ plasma.

The amorphous ternary metallic alloy $Zr_{60}Al_{15}Ni_{25}$ was oxidized in dry oxygen in the temperature range 310 °C to 410 °C. Rutherford backscattering and cross-sectional transmission electron microscopy studies suggest that during this treatment an amorphous

layer of zirconium-aluminum-oxide is formed at the surface. Nickel is depleted from the oxide and enriched in the amorphous alloy below the oxide/alloy interface. The oxide layer thickness grows parabolically with the annealing duration, with a transport constant of $2.8\times10^{-5}$ $m^2/s \times \exp(-1.7$ eV/kT). The oxidation rate is most likely controlled by the Ni diffusion in the amorphous alloy.

At later stages of the oxidation process, precipitates of nanocrystalline $ZrO_2$ appear in the oxide near the interface. Finally, two intermetallic phases nucleate and grow simultaneously in the alloy, one at the interface and one within the alloy.

# I. Reactively Sputtered Ti-Si-N Thin Films for Diffusion Barrier Applications

## Chapter 1 Introduction

The design and technology of the metal/silicon contact and of the metallization for interconnection lines of integrated circuits are continually gaining in emphasis as the density of components on a chip increases, the size of a single component shrinks, and the width of the interconnect lines and vias decreases. In that trend, diffusion barriers play an ever more critical role. In the metal/silicon contact, the diffusion barrier is a conductive layer introduced between the silicon or the silicide and the metal interconnect to prevent intermixing of the layers during processing. In a review paper by H. Kattelus and M-A. Nicolet [1], four basic categories of diffusion barriers are discussed — elemental barriers, stuffed barriers, inert barriers, and amorphous barriers. Elemental polycrystalline films are normally poor barriers. Even when they are thermodynamically stable with the metal overlayer and the Si below and when they do not exhibit substantial solubility for and in them, the grain boundaries in the film can provide fast diffusion path for atoms of the overlying metal film or of the Si. For example, Cu diffuses through a 100 nm of Ta layer at 450 °C, and affects the Si device below [2]. Recognizing this problem, the idea of stuffed barriers was introduced where the grain boundaries of the films are decorated with impurity atoms such as C, N, or O. These impurities can strongly hinder the diffusion along grain boundaries or extended defects. The diffusion is

further reduced by using highly refractory compounds ("inert barriers"), such as interstitial alloys whose melting point is extremely high. Amorphous compound barriers were proposed to completely eliminate grain boundary diffusion.

Ti/TiN bilayers are the most widely used adhesion/barrier scheme in industry for Al interconnects, and frequently with W as the via material [3]. To circumvent the use of W, Al reflow [4-7] and forcefill techniques are under development [4,8-11]. Such technologies also rely on a sturdy diffusion barrier.

As the line width and the via size shrink to sub-0.25 micron dimensions, industry faces new challenges, which call for yet further performance improvement of diffusion barriers. For example, sputtering gives non-uniform step coverage in the via. Even with a collimator, the thickness of the barrier at the top of a via opening is about twice that at the bottom [12-15]. To sustain subsequent heat treatments, a few tens of nanometers of TiN are required at the via bottom. In such instances, the excess TiN at the top corner of the via becomes a severe limitation. Chemical-vapor-deposited TiN has been developed in the recent past to circumvent this step-coverage problem [16]. For vias of sub 0.25 μm dimensions, the allowable barrier thickness is projected to decrease toward 5-10 nm. TiN barriers cannot currently meet this goal. Truly robust barriers are needed to satisfy such future requirements.

The shrinking via dimensions imposes stringent conditions on the electrical characteristics of a diffusion barrier. It is estimated that a via resistivity of 1 Ω is desired to satisfy the demand of speed [17]. That requirement calls for a barrier material that has

a bulk resistivity of less than 100 μΩcm if the barrier is 100 nm thick, or 1000 μΩcm if the barrier is 10 nm thick. Also, the contact resistance must be less than $10^{-9}$ $\Omega cm^2$.

Copper is presently considered as an interconnect material for the sub-0.25 μm era of ULSI to replace Al which is now commonly used [18-21]. The advantages of Cu are its low resistivity (1.7 μΩcm vs. 2.7 μΩcm for Al) and superior resistance to electromigration and stress voiding [22-23]. TiN is a natural choice as a barrier for Cu metallization because Cu is thermodynamically stable with TiN. In an early investigation, Cheung et al. reported a 650 °C maximum temperature of stability for 30 min vacuum annealing, when 100 nm of reactively sputtered TiN is used as a barrier between Cu and Si [24]. That result is based on Rutherford backscattering analysis. A review of the diffusion barriers for Cu can be found in ref. 25.

Experiments have been carried out to explore the mechanism of diffusion of Si, Al and Cu in TiN [26-28]. The results are listed in table 1.1. They indicate that the Al diffusivity in TiN is orders of magnitude higher than that of Si and Cu at 550 °C. The diffusion of Cu is substantial at 800 °C and faster than that of Si. All authors claim that diffusion mainly takes place at grain boundaries and defects.

Amorphous ternary diffusion barriers were first reported in 1988. Ternary thin films of the type TM-Si-N (TM=Ta, Mo or W) have shown outstanding barrier performance to Si devices for Al as well as for Cu metallizations [2,29-34]. W-Si-N films have also been found as excellent barriers for GaAs/Au contact [35,36]. The films are structurally amorphous and chemically inert with Cu and Si, two attributes that promote the low diffusivity and the high chemical stability that a good diffusion barrier

should process. From the reported Arrhenius laws [28,34], the diffusivity of Cu in an amorphous $Ta_{36}Si_{14}N_{50}$ film is lower than that in TiN at 800 °C (Table 1.1).

The first part of this thesis discusses in a systematic way the experimental results on ternary films of the type Ti-Si-N. The films are synthesized by reactively sputtering targets of $TiSi_2$, $Ti_5Si_3$, or $Ti_3Si$, in an $Ar/N_2$ mixture. The close compositional relationship of Ti-Si-N with the well-established TiN as thin-film diffusion barrier is a major advantage of this system over ternary films of other transition metals in terms of compatibility with established technology, and hence their acceptability.

In chapter 2, we report on the microstructure, atomic density and electrical resistivity of the films. The evolution of these properties upon heat treatment is considered as well. To clarify the mechanism of electrical conduction, the resistivity of $Ti_{34}Si_{23}N_{43}$ films, both as-deposited and annealed, is measured from 80 K to 1073 K. Results of reactive ion etching of the as-deposited $Ti_{34}Si_{23}N_{43}$ film in a $CF_4/O_2$ plasma are also discussed. The effectiveness of the Ti-Si-N films as diffusion barriers between Si and Al or Cu are reported and discussed in Chapters 3 and 4. A comparison of the Ti-Si-N films with TiN and other ternary TM-Si-N (TM=Ta, W, or Mo) films is provided to facilitate an evaluation of their applicability.

| | Diffusivity ($cm^2/s$) | | Activation energy | ref. |
|---|---|---|---|---|
| | at 550 °C | at 800 °C | (eV) | |
| Si diffusion in TiN | $8.3\times10^{-17}$ | $1.6\times10^{-16}$ | 0.27 | 26 |
| Al diffusion in TiN | $1.4\times10^{-15}$ | | 0.5 | 27 |
| Cu diffusion in TiN | $6.9\times10^{-20}$ | $1.4\times10^{-13}$ a) | 4.4 | 28 |
| Al diffusion in $Ta_{36}Si_{14}N_{50}$ | * | * | | 34 |
| Cu diffusion in $Ta_{36}Si_{14}N_{50}$ | $2.1\times10^{-19}$ | $1.9\times10^{-15}$ a) | 2.7 | 34 |

* self-sealing AlN layer forms between Al and $Ta_{36}Si_{14}N_{50}$, diffusivity is below resolution of secondary ion mass spectroscopy up to 700 °C heat treatment for 10 hours [34].

a) data extrapolated from Arrhenius relationship given in the reference.

Table 1.1 Diffusivity of Si, Al and Cu in TiN, and that of Al and Cu in $Ta_{36}Si_{14}N_{50}$ at 550 and 800 °C.

## REFERENCES

1. H. P. Kattelus, and M-A. Nicolet, in *Diffusion Phenomena in Thin Films and Microelectronic Materials*, edited by D. Gupta, and P.S. Ho, Noyes, NJ, 1988, Ch. 8.

2. E. Kolawa, J.M. Molarius, C.W. Nieh, and M-A. Nicolet, J. Vac. Sci. Technol. **A8**, 3006 (1990).

3. T. Ohba, MRS Bulletin, **34**, 46 (1995).

4. K. Kikuta, MRS Bulletin, **34**, 53 (1995).

5. S. Ogawa, H. Nishamura, T. Kouzaki, and R. Sinclare, in *Adavanced for ULSI Applications*, editted by T.S. Cale and F.S. Pintchovske (Mate. Res. Soc. Proc., Pittsburgh, 1992) p345.

6. G. Yao, S. Lee, H. Zhang, P. Ding, V. Lam, H. Kieu, Z. Xu, and F. Chen, in *Proc. 12th VLSI Multilevel Interconnect Conference*, edited by T.E. Wade (Santa Clara, CA, 1995) p220.

7. D.S. Gardner, Thin Solid Films, **262,** 104 (1995).

8. G.A. Dixit, M.F. Chisholm, M.K. Jain, T. Weaver, L.M. Ting, S. Poarch, K. Mizobuchi, R.H. Havemann, C.D. Dobson, A.I. Jeffryes, P.J. Holverson, Paul Rich, D.C. Butler, and J. Hems, in *IEEE International Electron Device Meeting Technical Digest*, (San Francisco, 1994) p105.

9. Shterenfeld-Lavie, et al. in *Proc.12th VLSI Multilevel Interconnect Conference*, edited by T.E. Wade (Santa Clara, CA, 1995) p31.

10. G.A. Dixit, W.Y. Hsu, K.H. Hamamoto, M. K. Jain, L.M. Ting, R.H. Havemann, C.D. Dobson, A.I. Jeffryes, P.J. Holverson, P. Rich, D.C. Butler, and J. Hems, Semiconductor International, August, 79 (1995).

11. A.J. Mcgeown, in *Adavanced Matallization and Interconnect Systems for ULSI Applications in 1995*, editted by R.C. Ellwanger and S.-Q. Wang (Mate. Res. Soc. Proc., Pittsburgh, 1996) p635.

12. R.V. Joshi, and S. Brodsky, in *Proc. 9th VLSI Multilevel Interconnection Conf.*, edited by T.E. Wade, (1992) p310.

13. J.G. Ryan, S.B. Brodsky, T. Katata, M. Honda, N. Shoda, and H. Aochi, MRS bulletin, **20** (11), 42 (1995).

14. T. Hara, T. Nomura, and S.C. Chen, Jpn. J. Appl. Phys. **31**, L1746 (1992).

15. H. Ito, K. Takada, N. Kajita, M. Hanai, Y. Hashimoto, and N. Tanaka, in *Advanced for ULSI Applications in 1993*, editted by D.P. Favreau, Y. Shicham-Diamand, and Y. Y. Horiike (Mate. Res. Soc. Proc., Pittsburgh, 1993) p.201.

16. See, for example, M. Eizenberg, MRS Bulletin, **20** (11), 38 (1995).

17. G. Bai, Intel Corporation, private conversation with M.-A. Nicolet.

18. J. Li, Y. Schacham-Diamand, and J.W.Meyer, Mater. Sci. Rep., **9**, 1 (1952).

19. J. Li, T.E. Seidel, and J.W. Mayer, MRS Bulletin, **19** (8), 15 (1994).

20. Y. Arita, N. Awaya, K. Ohno, and M. Sato, MRS Bulletin, **19** (8), 68 (1994).

21. For a review, see S.P. Murarka, and S.W. Hymes, CRC Crit. Rev. Solid State Mater. Sci. **20** (2), 87 (1995).

22. Y. Arita, Semiconductor World, 158 (Dec. 1993).

23. J. Tao, N.W. Cheung, and C. Hu, IEEE Electron Device Letters, **14**, 249 (1993).

24. N. Cheung, H. von Seefeld, and M-A. Nicolet, proceedings of the Symposium on Thin Film Interfaces and Interconnections, edited by J. E. E. Baglin and J. M. Poate (The Electrochemical Society, Inc., Princeton, New Jersey, 1980), p323.

25. For a review, see S.-Q. Wang, MRS Bulletin **19** (8),30 (1994).

26. K.G. Grigorov, G.I. Grigorov, M. Stoyanova, J.-L. Vignes, J.-P. Langeron, P. Denjean, and J. Perriere, Appl. Phys. **A 55**, 502, (1992).

27. K.G. Grigorov, G.I. Grigorov, M. Stoyanova, J.-L. Vignes, J.-P. Langeron, and P. Denjean, Appl. Phys. **A 57**, 195, (1993).

28. M.B. Chamberlain, Thin Solid Films, **91**, 155 (1982).

29. E. Kolawa, J.S. Chen, J.S. Reid, P.J. Pokala, and M-A. Nicolet, J. Appl. Phys. **70**, 1369 (1991).

30. J.S. Reid, E. Kolawa, R.P. Ruiz, and M-A. Nicolet, Thin Solid Films, **236**, 319, (1993).

31. J.S. Reid, E. Kolawa, C.M. Garland, M-A. Nicolet, F. Cardone, D. Gupta, and R.P. Ruiz, submitted to J. Appl. Phys.

32. J.S. Chen, E. Kolawa, R.P. Ruiz, and M-A. Nicolet, Mat. Res. Soc. Symp. Vol. 300, 285 (1993).

33. M-A. Nicolet, Applied Surface Science, 91, 269 (1995).

34. J.S. Reid, Ph.D. thesis, California Institute of Technology (1995).

35. H. Sugahara, J. Nagano, Appl, Surf. Sci., **41** 207 (1989).

36. K. Onodera, M. Tokumitsu, S. Sugitani, Y. Yamane, and K. Asai, IEEE Elec. Dev. Lett. **9**, 417 (1988).

# Chapter 2 Synthesis and Properties of Ti-Si-N Thin Films

## 2.1 Deposition and experimental procedures

The films were deposited by reactively sputtering a $TiSi_2$, a $Ti_5Si_3$, or a $Ti_3Si$ target in an rf magnetron sputtering system equipped with a cryopump and a cryogenic baffle. The targets are 3 inch in diameter, 1/8 inch in thickness, and were purchased from Cerac corporation. They were powder-pressed and have a purity level of 99.99%. They were bonded to 1/8 inch-thick Cu or Al backing plates using ECCOBOND® CT5047-2 silver-filled epoxy adhesive. The bonded targets were then mounted on one of the three target holders at the top of the sputtering system. The base pressure of the evacuated sputtering chamber is about $5 \times 10^{-7}$ Torr, but it rises to $2 \times 10^{-6}$ Torr with the cryopump throttled for sputtering. A net forward sputtering power of 300 W was applied. The substrates were placed on a holder about 3 inches below the target. The holder was grounded during deposition and could be rotated to place five separate sets of substrates below the target without interrupting the deposition process. A gas mixture of Ar and $N_2$ was used during sputtering. The flow rates of the gases are adjusted by MKS flow controllers. The sensitivity of the controllers is 0.1 $cm^3$/min. The Ar flow rate is fixed at 56 $cm^3$/min for all depositions, while the $N_2$ flow rate is varied from 0 to 4 $cm^3$/min. The substrates used are silicon wafers, either bare, or covered with either thermally-grown silicon dioxide or stripes of photoresist. Pieces of graphite tape were also included, which provide samples with a clean background for the N and O signals in their backscattering spectra. The thickness of the films is about 200 nm as measured by a

stylus profilometer using the patterned films and acetone lift-off. Some films on a thermally oxidized Si substrate were annealed in a quartz-tube furnace at a pressure less than $1\times10^{-6}$ Torr for an hour in the 400 to 1000 °C temperature range, for crystallization study and for sheet resistance measurement. Those on graphite substrates were annealed at 900 °C for 1 hour for composition and density analysis, and for comparison with the as-deposited sample.

The properties of the films, as-deposited and annealed, were characterized by 2.0 MeV $^{4}He^{2+}$ backscattering spectrometry, 12°-glancing angle and theta-twotheta x-ray diffractometry with Co $K_{\alpha}$ (0.179 nm) or Cu $K_{\alpha}$ (0.154 nm) sources, and four-point-probe sheet resistance measurement.

The microstructure of the films was characterized by transmission electron microscopy with either a Philips EM301 or a EM430 microscope. For these analyses, 20 nm-thick films were deposited on 3 mm-diameter Cu grids covered with holey carbon.

The experimental procedures described here are general. When a specific technique or analytical method was used to study a certain film, the details are described in the text. Experimental techniques and procedures used for x-ray photoelectron spectroscopy, cross-sectional transmission electron microscopy, resistivity measurement as a function of temperature, and reactive ion etching are described in the respective sections.

## 2.2 Composition of the films

The increase in the nitrogen content of the films with rising $N_2$ partial flow rate is shown in Fig. 2.1. The data were derived from the relative signal height of the elements in the backscattering spectra of the films on graphite substrates. For example, Fig. 2.2 displays the 2.0 MeV $^4He^{2+}$ backscattering spectrum of a 140 nm-thick $Ti_{34}Si_{23}N_{43}$ film deposited from the $Ti_5Si_3$ target on a graphite substrate. The extensions of the Ti peak on its high- and low-energy sides come from the low-abundance isotopes of Ti and the Ar impurity in the film. There is a 5% uncertainty in the atomic composition determined due to the resolution limitation of MeV $^4He^{2+}$ backscattering spectrometry and statistical errors. The multiple data points in Fig. 2.1 are the result of repeated depositions with the same sputtering parameters. We attribute the observed composition variations to the uncertainty in the $N_2$ partial flow rate, due to the sensitivity limit of the $N_2$ flow-meter, combined with the errors from the backscattering spectrometry measurement. The as-deposited Ti-Si-N films generally contain 2 to 5 at.% of oxygen. The oxygen is distributed uniformly within the film and with an increased amount at the surface. The oxygen content increases with the $N_2$ flow rate and therefore can be associated with oxygen introduced by the $N_2$ gas. The increase in oxygen content may also be related to the drop in sputtering rate with increasing $N_2$ partial pressure. The Ar content in the film cannot be accurately measured by backscattering spectrometry as its signal partly overlaps that of Ti, but it is estimated below 5 at.%. With increasing nitrogen concentration, the color of the as-deposited films changes from shiny silverish to dark gray, sometimes light brown with high nitrogen concentration.

In Fig. 2.1, the filled symbols stand for an amorphous structure and the dotted symbols for a nanocrystalline structure of the films, as determined by transmission electron microscopy (discussed in section 2.3.1). No such analysis was performed where open symbols are used. In the films deposited from the two Ti-rich targets, the nitrogen concentration increases initially steeply with the $N_2$ partial flow rate. A limitation of around 50 at.% is reached with a 4% nitrogen partial flow rate. With the Si-rich $TiSi_2$ target, a lower nitrogen concentration is achieved for the same nitrogen partial flow rate: 50 at.% is not reached at a nitrogen flow rate as high as 8%, and no sign of a saturation in the nitrogen content of the film is observed till that point.

The ternary composition of the films, as derived from their backscattering spectra, is reported in the phase diagram of Fig. 2.3a, using the symbols defined in the caption of Fig. 2.1. This phase diagram, suggested by Beyer et al. [1] and valid at 1000 °C, is a simplified version that does not show the existence range of the phases. A version that includes the non-stoichiometry and solubility of various phases of this diagram is reported by Sambasivan and Petuskey (Fig. 2.3b) [2]. Another ternary phase diagram by Rogl et al. (Fig. 2.3c) [3], based on experimental results and supported by recent calculations [4], shows a tie-line between $Si_3N_4$-$TiSi_2$ instead of Si-TiN. Their diagram also differs from that of Fig. 2.3b in the existence ranges of TiN with the $Si_3N_4$ and with the titanium silicide phases.

As can be seen from Fig. 2.3a, the Ti to Si ratio in these films is always close to that of the targets, because the compositions fall close to the straight dashed lines connecting N with the respective target phase. Previous studies of ternary thin films

deposited by reactive or non-reactive sputtering of TM-Si (TM=Ta, Mo, or W) targets reveal that the films are usually more metal-rich than the target [5,6]. The excess in metal content of the films decreases with increasing Si or N content in the film. This effect is not observed in the Ti-Si-N films.

The preferential sputtering of a compound target by ion bombardment is well known. The subject is summarized and discussed by, for example, G. Betz and G. K. Wehner [7]. A preferential sputtering process at the target does not affect the composition ratio of the emitted atoms, and hence that of the deposited film, as long as the target is sufficiently presputtered and a steady-state concentration is established at the target surface, assuming that the sticking coefficients of all species to the substrate are equal. However, a preferential re-emission can also take place at the substrate, or the surface of the growing film. This process enhances the fraction of heavy elements, or elements with higher binding energy, in the film. Titanium and silicon have atomic weights (47.90 and 28.09) that do not differ enough to cause a significant preferential enrichment of one of them in the film. The absence of this effect is an advantage in practice.

The uptake of nitrogen levels off for both Ti-rich film types as the nitrogen concentration reaches about 50 at.% (Fig. 2.1). This saturation occurs as the overall film composition nears the TiN-$Si_3N_4$ tie-line and is in accord with the behavior expected from the phase diagram (Fig. 2.3a). One would correspondingly predict a similar effect for the Si-rich films if their nitrogen content were to approach 60 at.%. A very similar saturation is observed for TM-Si-N (TM=Ta, W, Mo) and W-B-N films [6,8].

The loss of nitrogen or the gain of oxygen was roughly monitored by comparing the signal heights of the Ti in the film relative to that of the Si in the oxidized substrate, before and after one hour of annealing in vacuum at 900 °C. The drawback of this method is that it cannot distinguish between nitrogen loss and oxygen gain. A direct composition evaluation was also conducted with samples on graphite substrates. Unlike the Mo- and W-based ternary films (Mo-Si-N, W-Si-N and W-B-N) [6,8], no release of nitrogen or uptake of oxygen is detected in all Ti-Si-N films listed in Table 2.1 after vacuum annealing up to 900 °C for an hour, with both methods.

The composition and other information of some films selected for detailed analysis are listed in Table 2.1. Films with less than 20 at.% of nitrogen are absent in the table and the following figures. The practical difficulty of controlling small partial nitrogen flow rate in our deposition system prevents us from controllably synthesizing such films.

## 2.3 Microstructure

### 2.3.1 Planar structure and crystallization

#### a. $TiSi_2$ target

Figure 2.4 shows high-resolution transmission electron micrographs of three as-deposited films derived from the $TiSi_2$ target with different nitrogen content, namely, $Ti_{34}Si_{66}$ (a1), $Ti_{24}Si_{49}N_{27}$ (a2), and $Ti_{19}Si_{40}N_{41}$ (a3). The images indicate an amorphous structure of the films. The weak and broad rings in the diffraction patterns further

evidence that fact. No peak indicative of a crystalline microstructure appears in the x-ray diffraction spectra of these films.

The films were annealed for an hour in vacuum from 400 to 1000 °C at 100 °C intervals, using a virgin film for each temperature. Their crystallization temperatures and products were determined by x-ray diffractometry. The films of $Ti_{34}Si_{66}$ (a1) and $Ti_{24}Si_{49}N_{27}$ (a2) crystallize at 500 and 1000 °C, respectively. The $TiSi_2$ phase ($ZrSi_2$ structure type) [9] and the TiN and Si phases can be identified from the x-ray diffraction spectra.

The x-ray spectra of the as-deposited and annealed samples of $Ti_{19}Si_{40}N_{41}$ (a3) are shown in Fig. 2.5. No Bragg peak is visible, until the temperature is raised to 1000 °C, where TiN peaks emerge. This annealed film is brown in color, which resembles that of a reactively sputtered TiN film with a high oxygen level or a low density [10].

Figure 2.6 compares the bright-field images of $Ti_{19}Si_{40}N_{41}$ (a3) films as-deposited and annealed at 800 °C for one hour. A transmission electron microscopy specimen of an annealed film was obtained by depositing the film on an oxidized Si substrate, and etching from the back side with an $HF/HNO_3$ solution after the heat treatment until a tiny hole was formed on the film. In contrast to the amorphous structure of the as-deposited film, the annealed film contains nanocrystalline grains of sizes up to 5 nm. TiN is identified from the electron diffraction pattern. These nano-sized grains are not detected by x-ray diffraction (see Fig. 2.5). By the composition of the film, the phases of Si and $Si_3N_4$ are also expected at equilibrium. They are not observed, most probably because Si and N still form an amorphous phase.

**b. $Ti_5Si_3$ target**

High-resolution transmission electron microscopy was performed on as-deposited films with three different nitrogen contents (Fig. 2.7). The micrographs of $Ti_{62}Si_{38}$ (b1) and $Ti_{47}Si_{30}N_{23}$ (b2) display an image of randomly scattered intensities at the atomic-scale, which is characteristic of a disordered structure. The electron diffraction patterns show two board rings in both cases. In conclusion, both films are amorphous.

The micrograph of the $Ti_{34}Si_{23}N_{43}$ (b3) film reveals lattice fringes of several periods, randomly oriented and embedded in an apparent amorphous matrix. Rings can be discerned in the electron diffraction pattern that match the NaCl structure type of TiN. A bright-field and dark-field pair of the same as-deposited film is shown in Fig. 2.8. They again demonstrate a nanocrystalline structure. The grain size measured from the dark-field micrograph is 3 nm or less.

The bonding characteristic of the as-deposited $Ti_{34}Si_{23}N_{43}$ (b3) film was also investigated by x-ray photoelectron spectroscopy. The sample used consists of a 5 nm film on a Si substrate pre-cleaned in HF. The spectrum is calibrated with the C 1s line at 284.6 eV which corresponds to the C-C bond [11].

The line shape of the N 1s transition consists of two contributions (Fig. 2.9). A major one amounts to 80% of the signal. The electron binding energy of the signal maximum at 396.7 eV lies close to that reported for TiN (396.7-397.4 eV) [12-16]. The minor peak at 398.3 eV can be attributed to a $SiN_x$-like bonding. The electron binding

energy of sputtered amorphous $SiN_x$ was reported at 397.8 eV when x=0.91 and at 398.3 eV when x=1.33 [17].

The Ti 2p signal consists of two doublet peaks. One pair is at 455.8 and 458.5 eV and attributable to the Ti $2p_{1/2}$ line. The other pair is at 461.6 and 464.0 eV and attributable to the $2p_{3/2}$ line. Among the four sub-climaxes, the ones at 458.5 and 464.0 eV match the electron binding energy in TiN [12], the others correspond to $TiO_2$ bonds of rutile [12].

The above spectra identify the presence of bonding characteristics of TiN, $TiO_2$ and $SiN_x$. The rutile signal most probably emanates from a surface oxide of Ti formed during sample transfer from the deposition system to the XPS chamber. These results combined with the structural information from the micrographs suggest that the $Ti_{34}Si_{23}N_{43}$ (b3) film is phase-separated into nanocrystalline TiN and amorphous $SiN_x$.

The microstructure of a film with the same composition and deposited under the same conditions has been reported previously [18]. Other studies by x-ray spectrography, extended energy-loss fine structure (EXELFS), transmission electron microscopy and x-ray photoelectron spectroscopy of similar films have identified the presence of nanocrystalline TiN and amorphous $Si_3N_4$ phases [19-21]. Our results are consistent with those described there. When examined by x-ray diffraction with glancing-angle Cu $K_\alpha$ radiation on a Read-camera, or with Co $K_\alpha$ radiation and an Inel position-sensitive semi-ring detector, the b3 film (100 nm thick) shows no characteristic peaks or lines on either the photographic film or the spectrum.

By x-ray diffraction, the film $Ti_{62}Si_{38}$ (b1) crystallizes into the $Ti_5Si_3$ phase after 1 hour of annealing at 700 °C or above, and the films of $Ti_{47}Si_{30}N_{23}$ (b2) and $Ti_{34}Si_{23}N_{43}$ (b3) crystallize at or above 900 and 1000 °C respectively. The diffraction spectra suggest the formation of TiN and TiSi in the former and TiN in the latter (see Table 2.1). The color of the $Ti_{34}Si_{23}N_{43}$ (b3) film changes from dark gray to brown after annealing at 1000 °C.

**c. $Ti_3Si$ target**

Figure 2.10 presents the 12°-glancing angle x-ray diffraction spectra of three as-deposited films, $Ti_{76}Si_{24}$ (c1), $Ti_{50}Si_{17}N_{33}$ (c2) and $Ti_{35}Si_{13}N_{52}$ (c3), sputtered from the $Ti_3Si$ target. The spectra of $Ti_{76}Si_{24}$ (c1) and $Ti_{50}Si_{17}N_{33}$ (c2) contain only broad peaks. On the other hand, two sharp peaks are clearly discerned in the spectrum of $Ti_{35}Si_{13}N_{52}$ (c3). The width of these peaks implies that the grains are about 10 nm in size. These two peaks can be ascribed to diffraction from the (111) and (220) lattice planes of TiN.

The microstructure of these films is illustrated by the bright-field micrographs and the electron diffraction patterns shown in Fig. 2.11. Note that the magnification of this figure is 16 times less than in Fig. 2.4 and 2.7. The nitrogen-free film $Ti_{76}Si_{24}$ (c1) is amorphous. The $Ti_{50}Si_{17}N_{33}$ (c2) and $Ti_{35}Si_{13}N_{52}$ (c3) films are crystalline with grain sizes up to 5 and 10 nm, respectively. The TiN phase is again identified from the diffraction patterns. For a one hour annealing duration, the $Ti_{76}Si_{24}$ (c1) crystallizes at 500 °C or above. X-ray diffraction reveals the phase $Ti_3Si$ [22], as expected from its composition.

The as-deposited $Ti_{35}Si_{13}N_{52}$ (c3) film was also analyzed with theta-twotheta x-ray diffractometry. Other than the Si (111) peak from the substrate, only the (111) and (222) peaks of TiN are seen in the spectrum (Fig. 2.12). Presumably, the film also contains an amorphous phase of mostly Si and N that is not detected.

### 2.3.2 Film texture and grain orientation

Recognizing that the texture of the films may affect the performance of a diffusion barrier, we have analyzed the $Ti_{34}Si_{23}N_{43}$ (b3) and the $Ti_{35}Si_{13}N_{52}$ (c3) films by cross-sectional transmission electron microscopy.

Three films, $Ti_{53}N_{47}$, $Ti_{34}Si_{23}N_{43}$ (b3), and $Ti_{35}Si_{13}N_{52}$ (c3), are subsequently deposited on a 6H-SiC substrate. A cross-sectional transmission electron microscopy specimen was obtained by thinning a couple of sample slices, glued together face to face, using sandpaper and diamond paste. Afterwards, the specimen was dimpled until a tiny hole was formed close to the interface. It was then treated by glancing-angle ion milling, until the interface becomes transparent under the electron microscope. A SiC substrate was chosen as its hardness better matches that of TiN and Ti-Si-N than Si does, which lessens the preferential etching of the substrate by ion milling.

Fig. 2.13 presents a bright and dark-field pair of cross-sectional transmission electron micrographs of the layers (substrate not shown) taken at a 160 k magnification with a 20 μm objective aperture. The bottom layer is about 200 nm thick, and the two top layers are 100 nm each. Although the $Ti_{34}Si_{23}N_{43}$ (b3) film is nanocrystalline (see Fig. 2.7), the grains are not revealed in Fig. 2.13 taken under the above-specified conditions,

most likely due to the higher thickness of the sample as compared to the plan-view one (Fig. 2.7). The micrograph shows that the film is homogeneous without detectable preferred orientations. Conversely, the $Ti_{35}Si_{13}N_{52}$ (c3) film possesses a highly columnar grain structure. The $Ti_{53}N_{47}$ films preferably grows perpendicular to the surface, but to a lesser degree than the $Ti_{35}Si_{13}N_{52}$ (c3) film. The lateral grain size is larger than that of the $Ti_{35}Si_{13}N_{52}$ (c3) film.

Fig. 2.14 (top) shows a diffraction pattern of the trilayer with a 0.5 μm selective area diffraction aperture and a parallel beam. The pattern matches NaCl type TiN. The rings display a symmetrical angular contrast, especially clear on the (200) and (220) rings. The aperture used is the smallest one available on our microscope, so that a selective area diffraction pattern of the individual layers cannot be obtained. However, diffraction patterns were taken with the beam focused on a single layer. That of the $Ti_{34}Si_{23}N_{43}$ (b3) layer as shown in Fig. 2.14 (bottom) is basically continuous, indicating no obvious preferred orientation of the film. Those of the other two layers (not shown) include clearly oriented spots, which reflects a selective orientation of the columnar grains.

Fig. 2.15 (top) shows a diffraction pattern taken on a separate cross-sectional sample (micrograph not shown) of a single layer of $Ti_{35}Si_{13}N_{52}$ (c3) on an oxidized Si substrate. The pattern consists of broken parts of the TiN (111) and (200) rings. The arrangement of the heavily contrasted dots closely resemble the standard pattern for the <110> zone axis of a fcc crystal [23] (Fig. 2.15, bottom): both the distance ratio of the diffraction spots from the central spot of the transmission beam and the angles between

them agree with that pattern. This electron diffraction pattern is consistent with the theta-twotheta x-ray result of Fig. 2.12 which indicates that the grains have a <111> preferred orientation perpendicular to the substrate.

### 2.3.3 Discussion

Several cases were described in section 2.3.1 where a film appears amorphous by x-ray diffraction, while its transmission electron micrograph reveals a nanocrystalline structure and sharp rings appear in the electron diffraction pattern (e.g., Fig. 2.5 and 2.6). As a consequence, the crystallization temperature inferred from x-ray diffraction can exceed that deduced from transmission electron microscopy by as much as 200 °C, as for the film of $Ti_{19}Si_{40}N_{41}$ (a3). More significantly, the micrograph of the $Ti_{34}Si_{23}N_{43}$ (b3) film reveals a nanocrystalline structure of the film already in the as-deposited stage, whereas its crystalline structure is not discerned by x-ray diffractometry until after a 1000 °C-heat treatment. High resolution transmission electron microscopy and electron diffractometry analysis become essential in such instances. A similar case is described in ref. 18 for a $Ta_{36}Si_{14}N_{50}$ film deposited from a $Ta_5Si_3$ target.

Although the phase diagrams of Fig. 2.3 represent phase equilibria at 1000 °C, it serves well as a basis for discussion of the as-deposited films. In agreement with it, crystalline TiN phase is detected by transmission electron microscopy in the most titanium- and nitrogen-rich films. The nitrogen saturation at around 50 at.% in the films sputtered from the $Ti_3Si$ and $Ti_5Si_3$ targets is clearly related to the presence of a tie-line between TiN and $Si_3N_4$.

When the amorphous films crystallize at 900 or 1000 °C, the phases detected by x-ray diffractometry are polycrystalline Si in $Ti_{24}Si_{49}N_{27}$ (a2) and TiSi in $Ti_{47}Si_{30}N_{23}$ (b2), plus TiN in both. These phases are those one would expect from the diagram of Fig. 3a and 3b. Thus we further consider these diagrams.

Results in the previous section reveal that the NaCl-type TiN (or $Ti_{1-x}N_x$) phase exerts a dominant presence in the reactively sputtered Ti-Si-N films. This phase has a wide existence range from x=0.32 to x=0.55 [2]. According to Fig. 2.3b, it coexists with Si, $TiSi_2$ and TiSi only near the stoichiometric concentration where x=0.50. On the titanium-rich side, $Ti_{1-x}N_x$ forms a significant two phase area with the nitrogen-stabilized $Ti_5Si_3N_y$ phase. On the nitrogen-rich side, $Ti_{1-x}N_x$ equilibrates with $Si_3N_4$ over only a narrow composition range. All the ternary compositions we studied belong to equilibrium triangles with stoichiometric phases and near-stoichiometric TiN as vertexes. That being so, the phase diagram of Fig. 3a should constitute an acceptable simplification for the present study, and is therefore referred to in the following discussion.

The metal-to-silicon ratio of the films is close to that of the targets so that the compositions are all located near the straight lines connecting nitrogen with the corresponding titanium silicides (Fig. 2.3a). These lines intersect with the tie-line between TiN and Si (β line) at nitrogen concentrations of about 25 at.% for $TiSi_2$ and near 40 at.% for $Ti_5Si_3$ and $Ti_3Si$. Above these concentrations, $Si_3N_4$ equilibrates the two phases TiN and Si, and Si and titanium silicides below them.

Pure reactively sputtered films of TiN usually grow in polycrystalline form. The crystalline TiN phase also appears in the as-deposited $Ti_{34}Si_{23}N_{43}$ (b3), $Ti_{50}Si_{17}N_{33}$ (c2),

and $Ti_{35}Si_{13}N_{52}$ (c3) films, with reduced grain size. It can thus be concluded that films with a composition in the vicinity of TiN favor this structure. Conversely, sputtered films of the terminal phases $Si_3N_4$, Si, or titanium silicides are usually amorphous. We correspondingly find that the as-deposited films are amorphous when their composition places them in the vicinity of these phases. In the films where the crystalline TiN phase is detected, an amorphous phase with Si and N as major constituents coexists, as confirmed by the x-ray photoelectron spectroscopy result. A separate study by T. Iijima et al. [18] has also identified the $Si_3N_4$ phase in a similar film with the same method. For a nitrogen-rich film ($Ti_{29}Si_{22}N_{49}$), a study of the extended fine structure on the K-Si edge has also revealed a Si-N bonding close to that in amorphous $Si_3N_4$ [18]. In total, the available facts convincingly evidence that the microstructure of the as-deposited films is related to the position of their atomic composition in the ternary phase diagram. One can infer from the above results that at the atomic scale, the structure and bonding of these films bear close resemblance to the equilibrium phases of the respective three phase field. Resistivity results discussed in section 2.5 further evidenced the statement.

The film texture analysis by cross-sectional transmission electron microscopy establishes that a Si to Ti (or $SiN_x$ to TiN) ratio exceeding 1:3 is required in the Ti-Si-N films to avoid a columnar structure which is undesirable for a diffusion barrier.

### 2.4 Atomic density

The atomic density of the films versus the nitrogen concentration is plotted in Fig. 2.16 for the three targets. The density was derived by dividing the areal atomic density of

the films extracted from their backscattering spectra by the measured film thickness. The error of the data is within 10%. The atomic densities of some silicides phases are marked on the right axis. The non-reactively sputtered films of $Ti_{34}Si_{66}$ (a1) and $Ti_{62}Si_{38}$ (b1), obtained from the $TiSi_2$ and the $Ti_5Si_3$ targets, both have the atomic density of $6.3\times10^{22}$ $cm^{-3}$, which is 7% and 2% less than their bulk values of $6.94\times10^{22}$ $cm^{-3}$ ($TiSi_2$) and $6.43\times10^{22}$ $cm^{-3}$ ($Ti_5Si_3$) [24]. The $Ti_{76}Si_{24}$ (c1) film sputtered from the $Ti_3Si$ target has a lower density of $6.0\times10^{22}$ $cm^{-3}$. The bulk density of that phase is $6.04\times10^{22}$ $cm^{-3}$, as derived from the crystal structure of $Ti_3Si$ reported in ref. 22. For a common nitrogen concentration, the Si-rich films reactively sputtered from the $TiSi_2$ target always have higher densities than the Ti-rich films deposited with the $Ti_5Si_3$ or the $Ti_3Si$ target, except when the nitrogen concentration is low. The films of $Ti_{19}Si_{40}N_{41}$ (a3), $Ti_{34}Si_{23}N_{43}$ (b3), and the $Ti_{35}Si_{13}N_{52}$ (c3) are 10.2, 8.9 and 8.9 $\times10^{22}$ $/cm^3$ respectively in atomic density. No change in areal density is observed in these films by backscattering spectrometry after an hour annealing at 900 °C.

When they exist, amorphous phases usually have lower densities than their crystalline counterparts. The amorphous nitrogen-free silicides we have synthesized conform to this rule (Fig. 2.16). Of the terminal crystalline phases in the ternary Ti-Si-N phase diagram, TiN has the highest atomic density by virtue of its densely packed interstitial structure. Over its existence range of $0.32\leq x\leq0.55$, $Ti_{1-x}N_x$ has an atomic density that ranges from 7.6 to $10.5\times10^{22}$ $cm^{-3}$, and is $10.5\times10^{22}$ $cm^{-3}$ at exact stoichiometry. These values are derived from the lattice constant data in ref. 25, assuming that deviation from stoichiometry is caused by the deficiency of nitrogen or

titamium atoms in the cell. The density of the bulk α-$Si_3N_4$ phase is $9.5\times10^{22}$ $cm^{-3}$ [24]. That of its amorphous modification is several percent less than that ($8.4$-$9.3\times10^{22}$ $cm^{-3}$) at exact stoichiometry and up to 20% less ($7.4\times10^{22}$ $cm^{-3}$) when the composition departs from stoichiometry. The above quoted atomic densities of $Si_3N_4$ were derived from weight densities of chemical vapor deposited films listed in ref. 26. The terminal titanium silicide phases, on the other hand, have the lowest atomic densities (Fig. 2.16). A simple linear interpolation from the densities of the terminal phases would thus predict a monotonic increase of the atomic density with increasing nitrogen content, which is indeed observed in Fig. 2.16. Such a simple idea does not quantitatively explain the facts, though, as the measured atomic density of the film $Ti_{19}Si_{40}N_{41}$ (a3) exceeds those of $Ti_{34}Si_{23}N_{43}$ (b3) and amorphous $Si_3N_4$, and is close to the upper limit for TiN, while it is located further from the TiN and closer to the $Si_3N_4$ phase in the ternary phase diagram (see Fig. 2.3 and 2.16). Such data may point towards the existence of composition regions where a dense amorphous clustering of the three atomic species can be accomplished particularly efficiently.

## 2.5 Room temperature resistivity

### 2.5.1 General results

The resistivity of the films before and after 1 hour vacuum annealing at 700 °C is plotted in Fig. 2.17 and also reported in Table 2.1. The error of the measurement is estimated to be about 10%. The resistivity of the films rises monotonically with the nitrogen content for all three targets regardless of annealing, and decreases with

increasing Ti/Si ratio at all nitrogen concentrations. The higher resistivity of the two as-deposited nitrogen-free silicides, $Ti_{34}Si_{66}$ (a1) and $Ti_{62}Si_{38}$ (b1), over that of the crystalline bulk phases [27,28] (Table 2.1) can be attributed to the amorphous structure of the films. We were unable to find the resistivity of the bulk $Ti_3Si$ phase in literature. The effect of nitrogen incorporation on the resistivity increase is least pronounced for the $Ti_3Si$-derived films and strongest for the $TiSi_2$-originating films. The resistivity of these films also rises very steeply with the nitrogen concentration as it approaches 50 at.%. For example, the as-deposited $Ti_{17}Si_{35}N_{48}$ film has a resistivity of 40 mΩcm, which is ten times higher than that of the $Ti_{19}Si_{40}N_{41}$ (a3) film (4.2 mΩcm), although the nitrogen concentration in the films differs only by 7 at.%.

It is revealing to compare the plots of resistivity versus nitrogen content of the films (Fig. 2.17) with their overall composition reflected by their location in the ternary phase diagram of Fig. 2.3a. Figure 2.17 actually shows how the resistivity rises (before and after 1 hour annealing at 700 °C) along the dashed lines connecting the silicide phase of the target with the nitrogen at the apex in Fig. 2.3a. Several trends are recognizable:

- The films derived from the $Ti_3Si$ and $Ti_5Si_3$ targets that fall below or close to the TiN-$TiSi_2$ tie-line (labeled $\gamma$) all have resistivities below 300 μΩcm. Their resistivity rises weakly with nitrogen content. The equilibrium phases that correspond to their compositions are all metallic.

- As the film composition crosses the tie-line between TiN and Si ($\beta$-line), the resistivity rise of the films accelerates with nitrogen content. These crossings are indicated in Fig. 2.17 by the nitrogen concentration limits labeled $\beta$. The equilibrium phases that

correspond to compositions beyond the β-line have one metallic phase (TiN) and two semiconducting phases (Si and $Si_3N_4$).

- The resistivity of the films obtained from the $TiSi_2$ target whose compositions remain below the β-line (< 25 at.% nitrogen) rises more rapidly with nitrogen content than that of the other films (Fig. 2.17). The equilibrium phases corresponding to these compositions include a semiconductor (Si) and two metallic phases.

- When the composition of the $TiSi_2$-derived films nears the TiN-$Si_3N_4$ tie-line (labeled α) in the ternary phase diagram, the resistivity rises with nitrogen even more steeply than before. The dominant equilibrium phase that corresponds to these compositions is $Si_3N_4$, which is an insulating wide-band-gap semiconductor.

Although the trends elucidated here are only approximately fulfilled, the overall correlation between the resistivity of a film in Fig. 2.17 and its compositional position in the ternary phase diagram in Fig. 2.3a is clearly real. Such a correlation would not be a surprise for crystalline films but it is non-obvious for amorphous films. That a macroscopic parameter of an amorphous film such as its resistivity can be meaningfully related to its composition in an equilibrium phase diagram can only mean that at the atomic scale, the sputtered Ti-Si-N films have a bonding character that replicates at least approximately those of the equilibrium phases.

### 2.5.2 Effect of annealing

Upon one hour vacuum annealing at 700 °C, the resistivity of all films decreases, with the exception of those that are Si-rich and have more than about 30 at.% nitrogen

(above the β tie-line in Fig. 2.3a). For instance, resistivity of the $Ti_{34}Si_{23}N_{43}$ (b3) from the $Ti_5Si_3$ target decreases from its as-deposited value of 660 μΩcm to 410 μΩcm after the heat treatment. A decrease of the resistivity upon annealing is common for sputter-deposited conducting films. The effect is usually ascribed to a relaxation of the atomic disorder in amorphous materials, or of the intergranular strain in crystalline films and the effect of grain growth.

The rise in the resistivity of the Si-rich films with more than 30 at.% nitrogen is a phenomenon that is plausibly associated with the formation, segregation and redistribution of a $SiN_x$-like structure and bonding, since $SiN_x$ is the only high-resistivity phase in the ternary system. The increase in resistivity of films from a $TiSi_2$ target with a high nitrogen concentration is very significant. The $Ti_{19}Si_{40}N_{41}$ (a3) film has an as-deposited resistivity of 4.2 mΩcm, and it rises to 24 mΩcm following the annealing.

Another relevant observation one can extract from Fig. 2.17 is that a film derived from the $TiSi_2$ target with about 30 at.% nitrogen concentration has a resistivity that remains unchanged upon annealing. The resistivity of films from the $Ti_3Si$ target with about 50 at.% of nitrogen also changes little with annealing. Such a characteristic is desirable for thin films resistor applications.

The resistivity of three films, $Ti_{24}Si_{49}N_{27}$ (a2), $Ti_{19}Si_{40}N_{41}$ (a3), and $Ti_{34}Si_{23}N_{43}$ (b3), as-deposited and after annealing from 500 to 1000 °C for an hour are plotted with respect to temperature in Fig. 2.18. The as-deposited films of $Ti_{24}Si_{49}N_{27}$ (a2), $Ti_{19}Si_{40}N_{41}$ (a3) from the $TiSi_2$ target are amorphous, and that of $Ti_{34}Si_{23}N_{43}$ (b3) from the $Ti_5Si_3$ target is nanocrystalline. All three films have an x-ray crystallization

temperature of 1000 °C. Their resistivity change with temperature differs radically. The resistivity of the Si-rich films $Ti_{24}Si_{49}N_{27}$ (a2) and $Ti_{19}Si_{40}N_{41}$ (a3) decreases slightly at first, reaching a minimum respectively at 800 and 500 °C, and rises abruptly afterwards, while that of the Ti-rich film $Ti_{34}Si_{23}N_{43}$ (b3) drops monotonically with annealing temperature.

The above observations are tentatively explained here by correlating the resistivity to the microstructure of the films. We concentrate our discussions on the nitrogen-rich films of $Ti_{19}Si_{40}N_{41}$ (a3) and $Ti_{34}Si_{23}N_{43}$ (b3). The as-deposited and low-temperature-annealed films of $Ti_{19}Si_{40}N_{41}$ (a3) have an amorphous structure. The bonding between the atoms is presumably partially metallic. At higher temperatures, the film partially crystallizes into the TiN phase. For simplicity, we model the films macroscopically as conductive cubes, orderly arranged, and embedded in a matrix of insulating material, as illustrated by Fig. 2.19. Such a structure is generally insulating and its resistivity does not change with the grain dimension when the ratio a to b is fixed. However, if the insulating gap b is sufficiently small, tunneling of electrons across the insulating gap b becomes important. For electron tunneling, the resistivity of an insulator slab increases exponentially with b [29], resulting in a sharp rise of the overall resistivity with the annealing temperature as the grains grow. Although this model over-simplifies the situation, it gives a possible qualitative explanation for the resistivity increase upon heat treatment.

In the $Ti_{34}Si_{23}N_{43}$ (b3) film, TiN is a dominant phase and presumably percolates through the insulating phase, making the overall structure conductive. Further discussion is given in section 2.6.

## 2.6 Temperature dependence of resistivity

### 2.6.1 Measurement procedures

For comparison, a TiN film is also included in this investigation. A TiN film with the composition $Ti_{53}N_{47}$ was deposited on thermally oxidized silicon substrate by reactively sputtering a 3-inch-diameter Ti target in an $Ar/N_2$ discharge. A forward power of 550 W and a substrate bias of -60 V were applied. The thickness of the films was measured by a Dektak profilometer on samples that had been patterned photolithographically for lift-off to provide a sequence of sharp steps for the measurements. The estimated error from the thickness variation caused by deposition and the resolution of the equipment is about 10%.

The sheet resistance measurement from 50 °C to 800 °C was performed in a vacuum better than $1\times10^{-6}$ Torr with a four-point-probe made of gold-coated stainless steel. The sample was placed on a hot copper stage heated resistively and the temperate was regulated by a thermal controller. Measurement below ambient temperature was done in a vacuum of mTorr using the same type of probes as for the high-temperature tests. The sample stage was first cooled down to liquid nitrogen temperature and then left to warm up on its own accord. The measurement was performed during that warming up period, which takes 3 to 4 hours.

### 2.6.2 Results

Figures 2.20 and 2.21 show the resistivity versus temperature from 80 K to 1073 K for $Ti_{53}N_{47}$, and to 873 K for $Ti_{34}Si_{23}N_{43}$ (b3). Two runs were performed on each sample above room temperature. The data obtained for the two runs differ by at most 2% in all cases. This agreement ensures that if changes were induced in the films by the heat treatment, they remained insignificant for the present measurements for both types of films.

The resistivity of as-deposited $Ti_{53}N_{47}$ starts from about 41 μΩcm at 80 K, rising linearly to about 51 μΩcm at around 300 K. It increases further up to a faint maximum of 64 μΩcm at between 700 to 800 K, beyond which it falls very slightly to about 62 μΩcm. The above results show that this film is metal-like.

The as-deposited $Ti_{34}Si_{23}N_{43}$ (b3) film shows a quite different temperature behavior (Fig. 2.21, top). The resistivity decreases monotonically with increasing temperature from 670 μΩcm at 80 K to 570 μΩcm at 873 K. At room temperature, the resistivity of the film is about 635 μΩcm, which is an order of magnitude larger than that of $Ti_{53}N_{47}$.

We have also performed the measurement on a $Ti_{34}Si_{23}N_{43}$ (b3) films from 80 to 1073 K after it is annealed at 1000 °C for an hour. The result is shown in Fig. 2.21 (bottom). The shape of the curves now looks similar to that of the as-deposited TiN. The resistivity of annealed $Ti_{34}Si_{23}N_{43}$ (b3) increases with temperature until it reaches a maximum (~290 μΩcm) at around 823 K, 1.9 % higher than that at 80 K (~150 μΩcm).

### 2.6.3 Discussion

The electric conductance of TiN films at room temperature or below is well documented and summarized by J.-E. Sundgren in a review paper [30]. The room temperature resistivity is variously quoted as ranging from 18 to hundreds of μΩcm. The resistivity is known to sensitively depend on the composition of film. The minimum usually occurs at exact stoichiometry. The resistivity value is also affected by other film properties like impurity level (especially oxygen), grain size, and defects. These are also the crucial factors that determine the temperature dependence of resistivity, as voids and impurities are both effective scattering centers. A linear relationship between the resistivity and temperature is usually observed from liquid nitrogen to room temperature. Temperature coefficients of resistivity that vary from negative to plus a few thousands $ppmK^{-1}$ have been reported [31-36], but the coefficient is usually 1000 to 2000 $ppmK^{-1}$ at stoichiometry. The temperature coefficient of resistivity derived from our measured data is 880 $ppmK^{-1}$ at 300 K.

The electrical properties of Ti-Si-N films deposited in a triode sputtering system have been reported from 70 K to 470 K by W. Posadowski, who considers the material for application as thin film resistors [37]. The TiN to $SiN_x$ ratio in those films was estimated from x-ray spectrography. Posadowski reports that films with less than 80% of TiN behave “dielectrically”, and follow a $\ln \rho = AT^{-1/2}$ relationship. This “dielectric” behavior was observed and modeled before in granular metal thin films [29] where nanometer-sized metallic particles are isolated by insulating materials and current

transport is only possible by tunneling of the charge carriers between isolated metal particles. We know that at the atomic level our $Ti_{34}Si_{23}N_{43}$ (b3) film is compositionally nonuniform with nanocrystalline regions of TiN embedded in an amorphous matrix of principally $SiN_x$ bonded atoms. It is likely that the TiN grains percolate through the $SiN_x$ phase at most places, giving rise to its low resistivity despite the existence of the insulating $SiN_x$ phase. On the other hand, tunneling could play an important role in as-deposited $Ti_{34}Si_{23}N_{43}$ (b3), as its resistivity curve manifests. After one hour heat treatment at 1000 °C, Bragg peaks appear in x-ray diffraction, which reflects a redistribution and growth of the crystalline islands. Plausibly, the conductive crystallites now percolate through the amorphous insulator. Tunneling is no longer an important mechanism and thus can be ignored. The resistivity curve thus manifests the characteristic of the metallic TiN phase.

## 2.7 Reactive ion etching

Reactive ion etching of the $Ti_{34}Si_{23}N_{43}$ (b3) film was investigated by G.F. McLane at the Army Research Office using a $CF_4/O_2$ gas mixture [38]. The etch depth is found proportional to the etching duration without initial delay (Fig. 2.22). Fig. 2.23 shows the etch rate verses oxygen partial flow rate at 40 sccm total flow, 80 mTorr pressure and 140 W cathode power. The plasma etches most efficiently at 20% $O_2$, resulting in a rate of about 10 nm per minute. Adding $O_2$ to $CF_4$ initially releases F atoms by forming molecules such as $CO_2$, CO, and $COF_2$, but excess $O_2$ dilutes the

concentration of etching species and finally causes a reduction in the etching rate at a fixed total flow.

The etch rate peaks at 140 mTorr gas pressure. In a plasma, the cathode voltage and ion bombardment energy decrease with increasing gas pressure. This effect causes a drop in the etch rate at higher pressure. The etch rate is essentially independent of cathode power over the range 90-190 W.

A depletion in Si and N is detected in the surface region of the etched sample. In contrast, no preferential etching is observed in the $Ta_{36}Si_{14}N_{50}$ film with the same plasma [39]. These results reflect the nonvolatility of Ti-fluoride and the moderate volatility of Ta-fluoride. Also, the etch rate of $Ti_{34}Si_{23}N_{43}$ (b3) is lower than that of $Ta_{36}Si_{14}N_{50}$.

### 2.8 Conclusion

The as-deposited films of Ti-Si-N have either an amorphous or a nanocrystalline plan-view structure. The fine-scale structure is beyond the resolution of x-ray diffractometry and must be monitored by transmission electron microscopy and electron diffraction. A mixed structure of crystalline TiN and amorphous $SiN_x$ is proposed for some nitrogen-rich films. After thermal treatment, the film composition and density remain unchanged.

We find, furthermore, that in the nitrogen-rich films, the grain structure is strongly affected by the Si concentration. With about 10-15 at.% of Si in the films, the crystal size of TiN is reduced to 10 nm or less, but the grains remain highly columnar, and <111>

oriented, as they typically are in TiN films. When the Si content is increased to 20-25 at.%, the grain size is further reduced to 3 nm or less, and the film becomes textureless.

The correlation between the resistivity of a film and its compositional position in the ternary phase diagram, evident even for amorphous films, indicates that at the atomic scale, the spatial arrangement of atoms in Ti-Si-N films and their bonding character must replicate approximately those of the terminal equilibrium phases.

Electrical measurement from 80 K to 1073 K shows that TiN is metallic. The as-deposited $Ti_{34}Si_{23}N_{43}$ (b3) films possess a resistivity that decreases with temperature. Possibly the current is conducted by tunneling of the electrons between isolated islands. After annealing for 1 hour at 1000 °C, the $Ti_{34}Si_{23}N_{43}$ (b3) film shows a metallic behavior similar to TiN. We postulate that in the b3 film, TiN grains percolate through the amorphous $SiN_x$ matrix, and thus establish metallic conduction.

## REFERENCES

1. R. Beyers, R. Sinclair, and M.E. Thomas, J. Vac. Sci. Technol. B **2**, 781 (1984).

2. S. Sambasivan, and W.T. Petuskey, J. Mater. Res. **9**, 2362 (1994).

3. P. Rogl and J.C. Schuster (eds), *Phase Diagrams of Ternary Boron Nitride and Silicon Systems*, ASM International, Materials Park, OH (1992).

4. A. M. Dutrom and C. Bernard, to be published.

5. E. Kolawa, J.M. Molarius, C.W. Nieh, and M-A. Nicolet, J. Vac. Sci. Technol. **A8**, 3006 (1990).

6. J.S. Reid, E. Kolawa, R.P. Ruiz, and M-A. Nicolet, Thin Solid Films, **236**, 319, (1993).

7. G. Betz, and G.K. Wehner, in *Sputtering by Particle Bombardment*, edited by R. Behrisch (Springer-Verlag, Berlin, 1983), Chap. 2.

8. J.S. Reid, R.Y. Liu, P.M. Smith, R.P. Ruiz, and M-A. Nicolet, Thin Solid Films, **262**, 218 (1995).

9. P.G. Cotter, J.A. Kohn, and R.A. Potter, J. Am. Ceram. Soc. **39**, 11 (1956).

10. See, for example, N. Kumar, J.T. McGinn, K. Pourrezaei, B. Lee, and E.C. Douglas, J. Vac. Sci. Technol. A**6** (3), 1602 (1988).

11. P. Grunthaner, private conversation.

12. C.D. Wagner, W.M. Riggs, L.E.Davis, J.F. Moulder, and G.E. Muilenberg, *Handbook of X-Ray Photoelectron Spectroscopy* (Perkin-Elmer, Physical Electonics Division, Eden Prairie, MN, 1979).

13. M. Delfino, J.A. Fair, and D. Hodul, J. Appl. Phys. **71**, 6079 (1992).

14. B.J. Burrow, A.E. Morgan, and R.C. Ellwanger, J. Vac. Sci. Technol. **A4**, 2463 (1986).

15. H. Bender, J. Portillo, and W. Vandervorst, Surf. Interface Anal. **14**, 337 (1989).

16. M.J. Vasile, A.B. Emerson, and F.A. Baiocchi, J. Vac. Sci. Technol., **A8**, 99 (1990).

17. G.M. Ingo, and N. Zacchetti, High Temperature Science, **28**, 137 (1990).

18. J.S. Reid, Ph.D. thesis, California Institute of Technology, 1995 (unpublished).

19. J.S. Reid, X. Sun, E. Kolawa, and M-A. Nicolet, IEEE Eletron. Devices Lett. **15**, 298 (1994).

20. W. Posadowski, Thin Solid Films, **162**, 111 (1988).

21. T. Iijima, Y. Shimooka, G. Minamihaba, and K. Suguro, in *Proc. Adavanced Matallization and Interconnect Systems for ULSI Applications in 1995*, editted by R.C. Ellwanger and S.-Q. Wang (Material Research Society, Pittsburgh, PA, 1996) p325.

22. K. Schubert, A. Raman, and W. Rossteutscher, Naturwissenschaften, **51**, 506 (1964).

23. J.W. Edington, *Practical Electron Microscopy in Material Science* (Philips, Eindhoven, 1976).

24. *TAPP* (A database of Thermochemical And Physical Properties, computer software, 1994).

25. H.J. Goldschmidt, *Interstitial Alloys* (Butterworth & Co., London, 1967), Chap. 5.

26. J.W. Mayer, S.S. Lau, *Electronic Material Science* (Macmillan Publishing Company New York, 1990), pp 225.

27. G.V. Samsonov, and I.M. Vinitskii, *Handbook of Refractory Compounds* (IFI/ Plenum Press, New York, 1980).

28. P.T.B. Shaffer, *Plenum Press Handbook of High-Temperature Materials*, No. 1. (Plenum Press, New York, 1964).

29. B. Abeles, Ping Sheng, M. D. Coutts, and Y. Arie, Adv. Phys. **24,** 407 (1975).

30. J.-E. Sundgren, Thin Solid Films, **128**, 21 (1985).

31. J.-E. Sundgren, B.-O. Johansson, S.-E. Karlsson, and H.T.G. Hentzell, Thin Solid Films, **105**, 367 (1983).

32. Y. Igasaki, and H. Melchior, Thin Solid Films, **70**, 17 (1980).

33. W. Posadowski, L. Krol-Stepniewska, and Z. Ziolowski, Thin Solid Films, **62**, 347 (1979).

34. J.M. Poitevin, G. Lemperiere, and J. Tardy, Thin Solid Films, **97**, 69 (1982).

35. G. Lemperiere, and J.M. Poitevin, Thin Solid Films, **117**, 339 (1984).

36. Y. Igasake, and H. Mitsuhashi, Thin Solid Films, **70**, 17 (1980).

37. W. Posadowski, Thin Solid Films, **162**, 111 (1988).

38. G.F. Mclane, T. Monahan, X. Sun, J.S. Reid, M-A. Nicolet, to be published.

39. G.F. Mclane, L. Casas, J.S. Reid, E. Kolawa, M-A. Nicolet, J. Vac. Sci. **B12**, 2352 (1994).

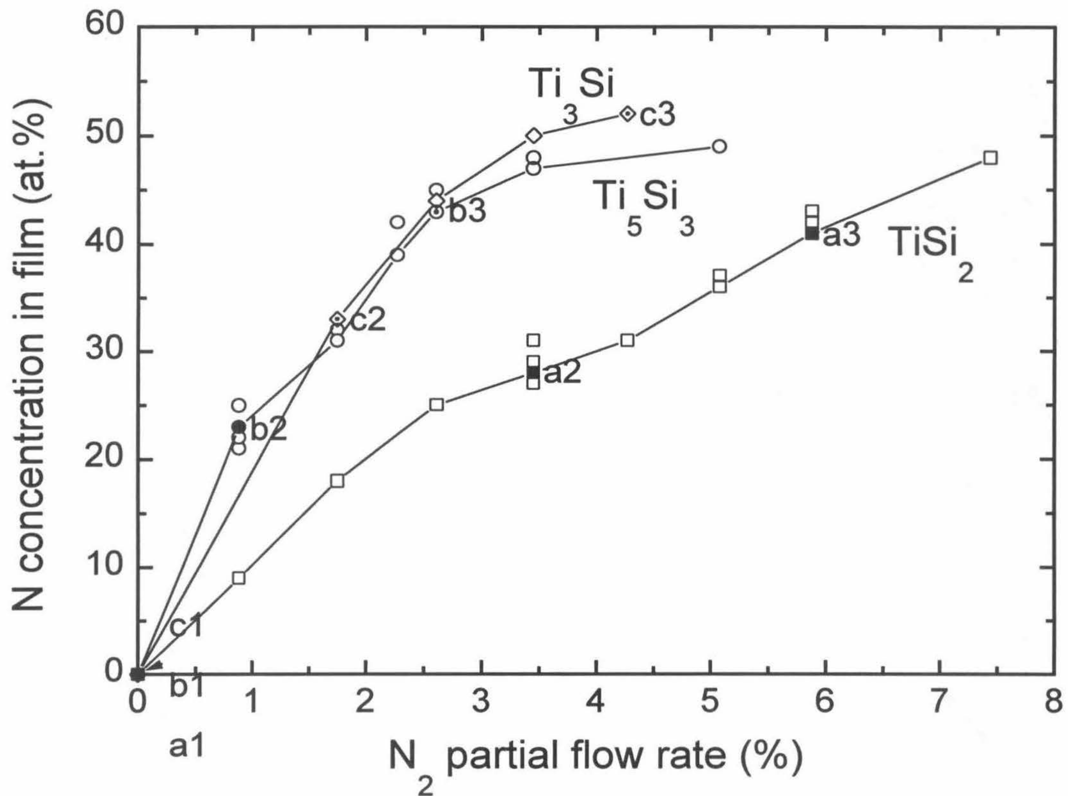


FIG. 2.1. Percentage concentration of N atoms in the films reactively sputtered from $TiSi_2$, $Ti_5Si_3$, or $Ti_3Si$ target, with respect to the nitrogen partial flow rate. The filled symbols represents an amorphous structure and the dotted symbols, a nanocrystalline structure of the films, as determined by transmission electron microscopy (see Fig. 2.3). No such analysis was performed where open symbols are used.

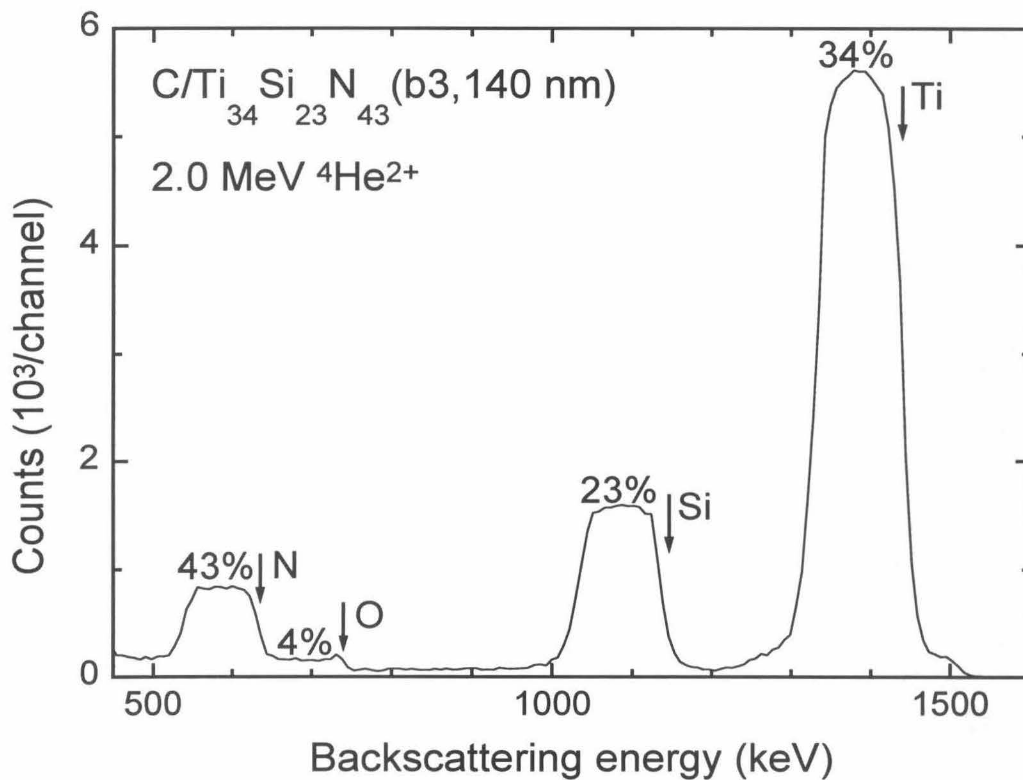


FIG. 2.2. 2.0 MeV $^4He^{2+}$ backscattering spectrum of ~140 nm $Ti_{34}Si_{23}N_{43}$ film on graphite substrate (5°-off normal beam incidence; scattering angle of detected particles is 170°).

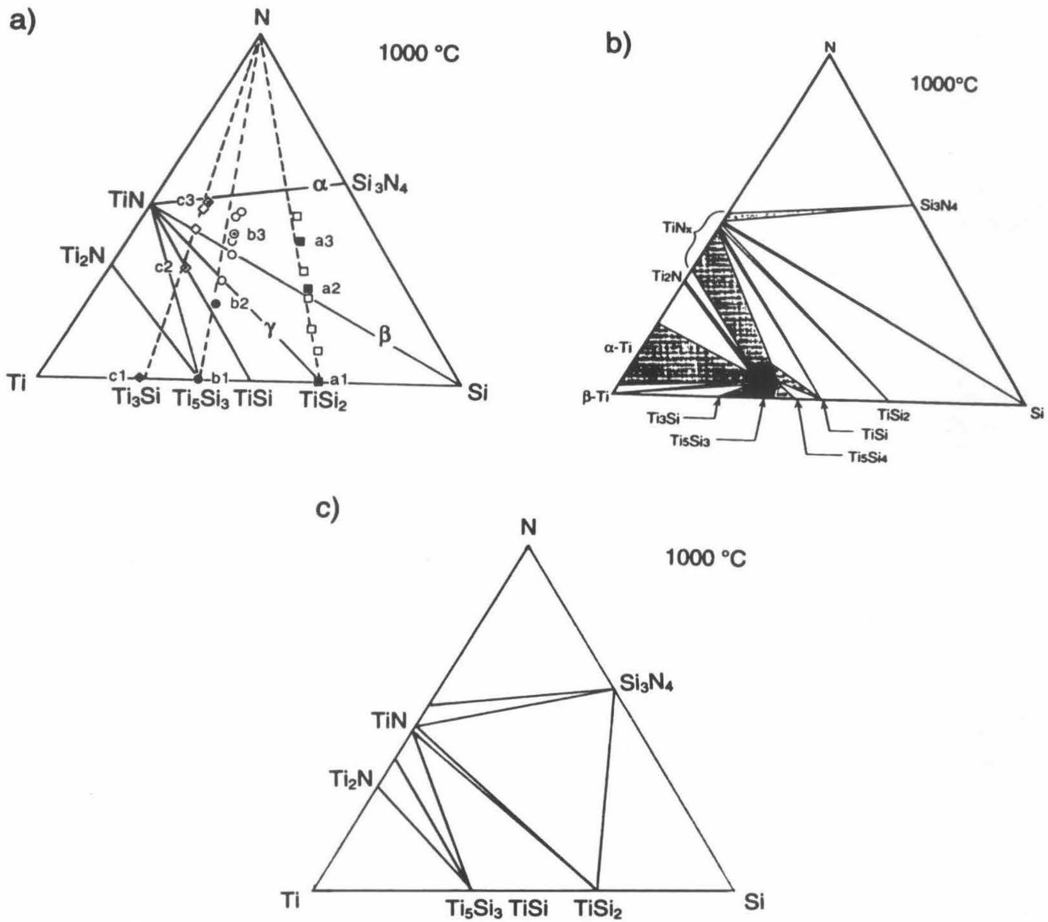


FIG. 2.3. Simplified (a) and complete (b) Ti-Si-N phase diagrams in the 700 to 1000 °C temperature range (replotted from ref. 1 and 2). Compositions of the films are marked with symbols as defined in the caption of Fig. 2.1. Another version from ref. 3 is also plotted (c).

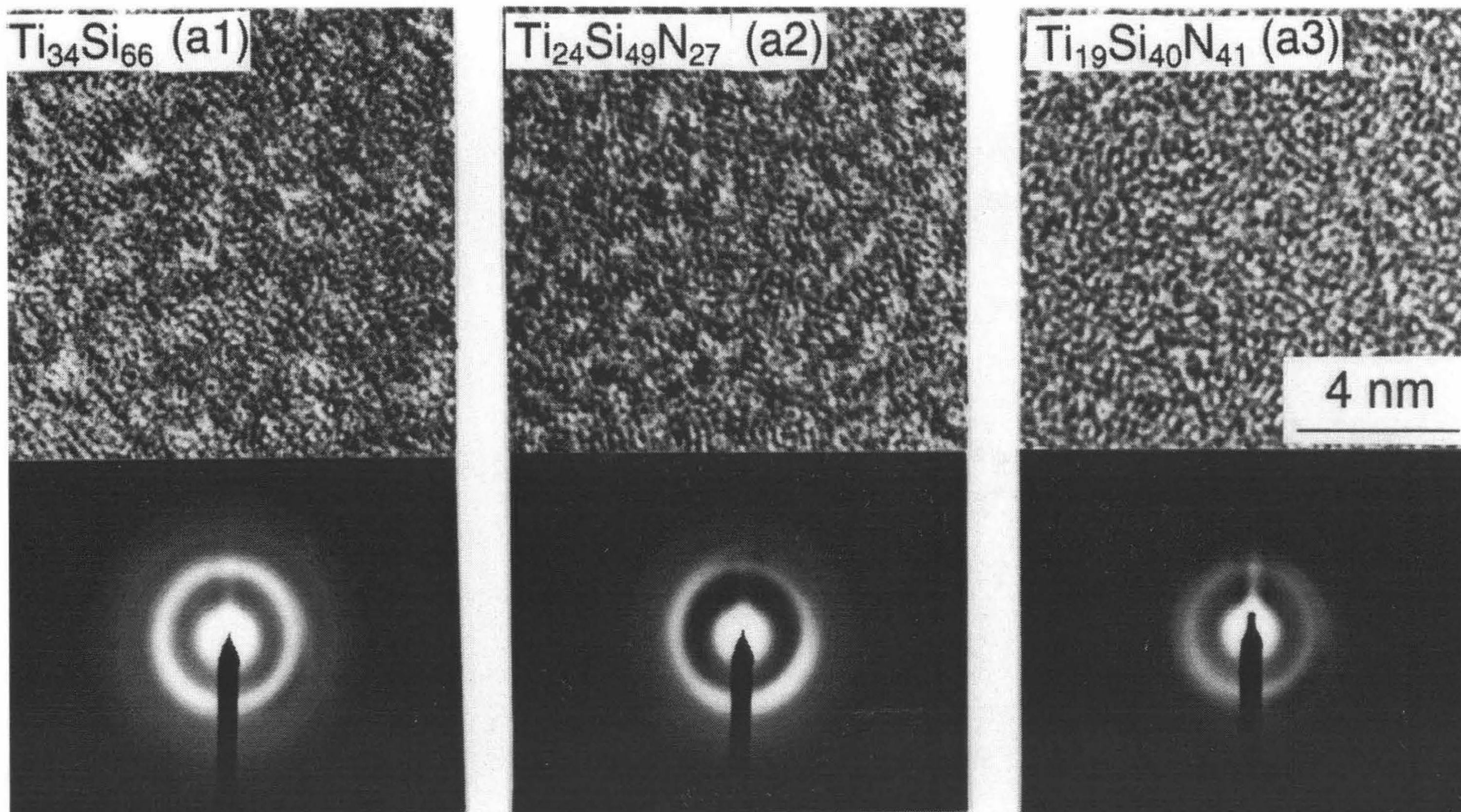


FIG. 2.4. High-resolution transmission electron micrographs(plan-view) of as-deposited $Ti_{34}Si_{66}$ (a1), $Ti_{24}Si_{49}N_{27}$ (a2), and $Ti_{19}Si_{40}N_{41}$ (a3) films reactively sputtered from a $TiSi_2$ target, with electron diffraction patterns.

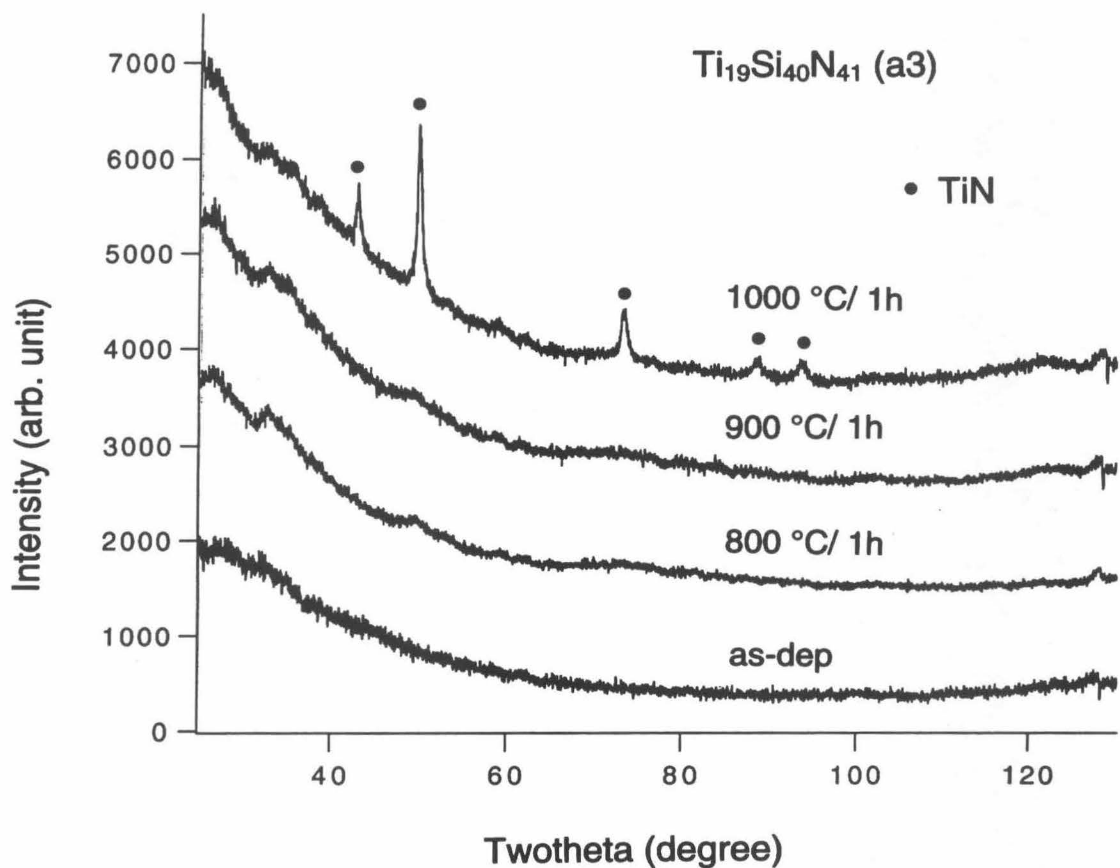


FIG. 2.5. 12°-glancing angle x-ray diffraction spectra of the $Ti_{19}Si_{40}N_{41}$ (a3) film as-deposited and after 1 hour annealing at 800, 900 and 1000 °C, taken with Co $K_{\alpha}$ radiation (0.179 nm).

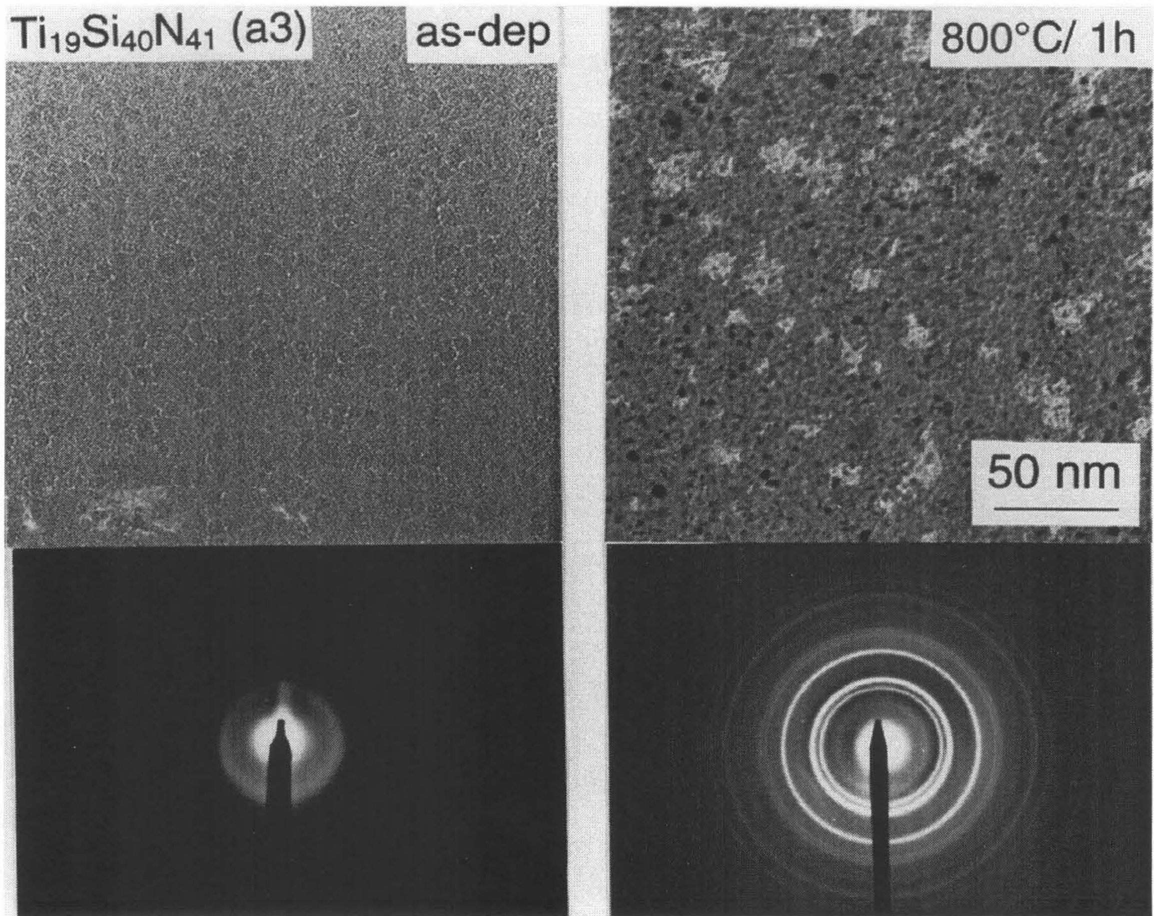


FIG. 2.6. Bright-field transmission electron micrographs of the $Ti_{19}Si_{40}N_{41}$ (a3) film as-deposited and after 1 hour annealing at 800 °C, with electron diffraction patterns. Compare with Fig. 2.5.

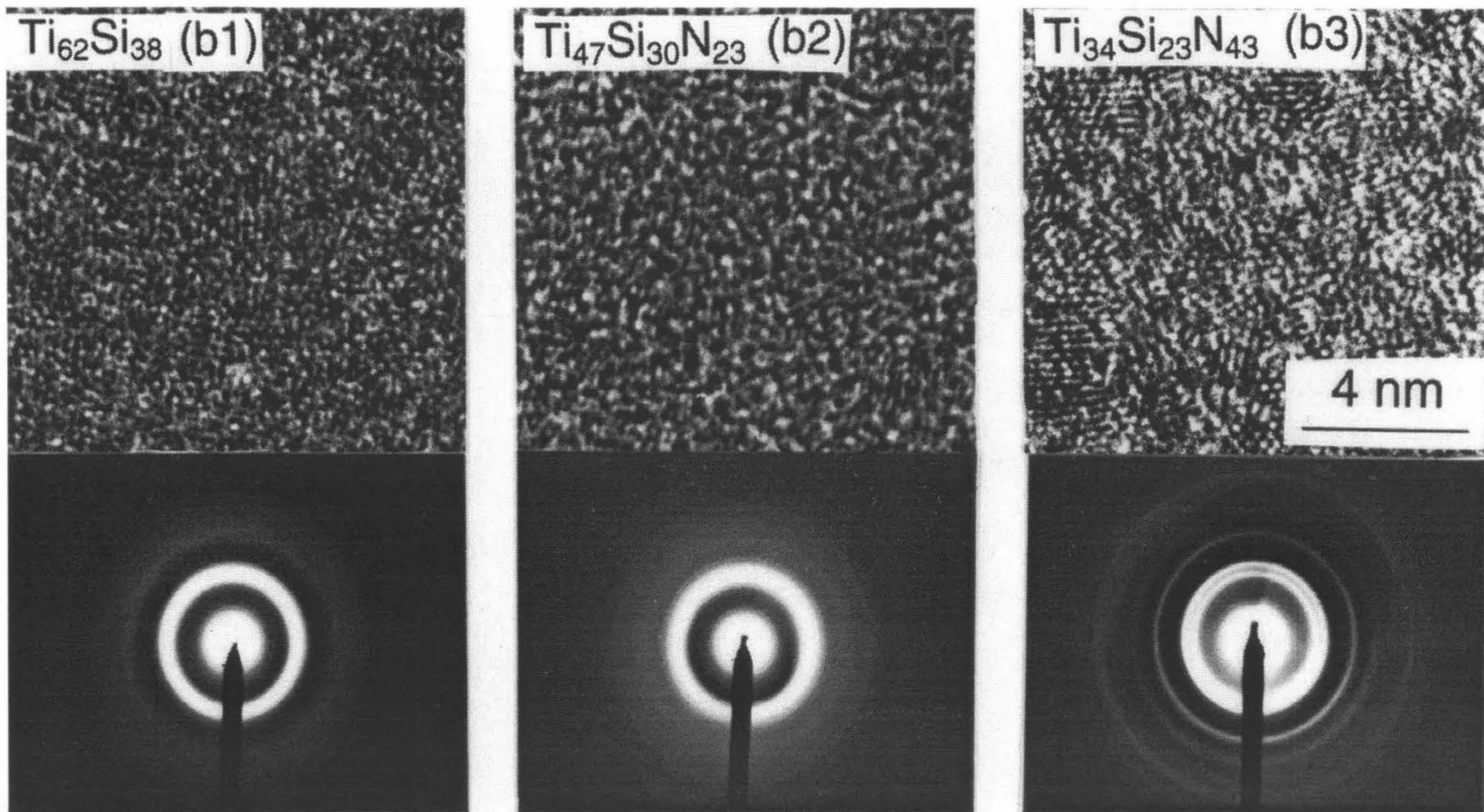


FIG. 2.7. High-resolution transmission electron micrographs (plan-view) of as-deposited $Ti_{62}Si_{38}$ (b1), $Ti_{47}Si_{30}N_{23}$ (b2), and $Ti_{34}Si_{23}N_{43}$ (b3) films reactively sputtered from a $Ti_5Si_3$ target, with electron diffraction patterns.

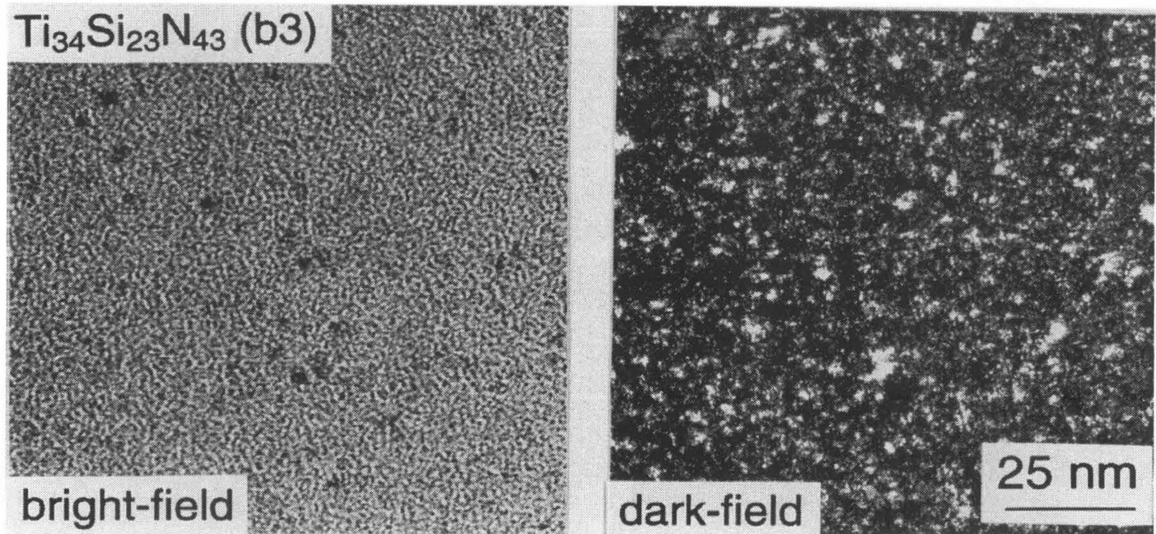


FIG. 2.8. Bright and dark-field transmission electron micrographs (plan-view) of the as-deposited $Ti_{34}Si_{23}N_{43}$ (b3) film reactively sputtered from a $Ti_5Si_3$ target, with electron diffraction patterns.

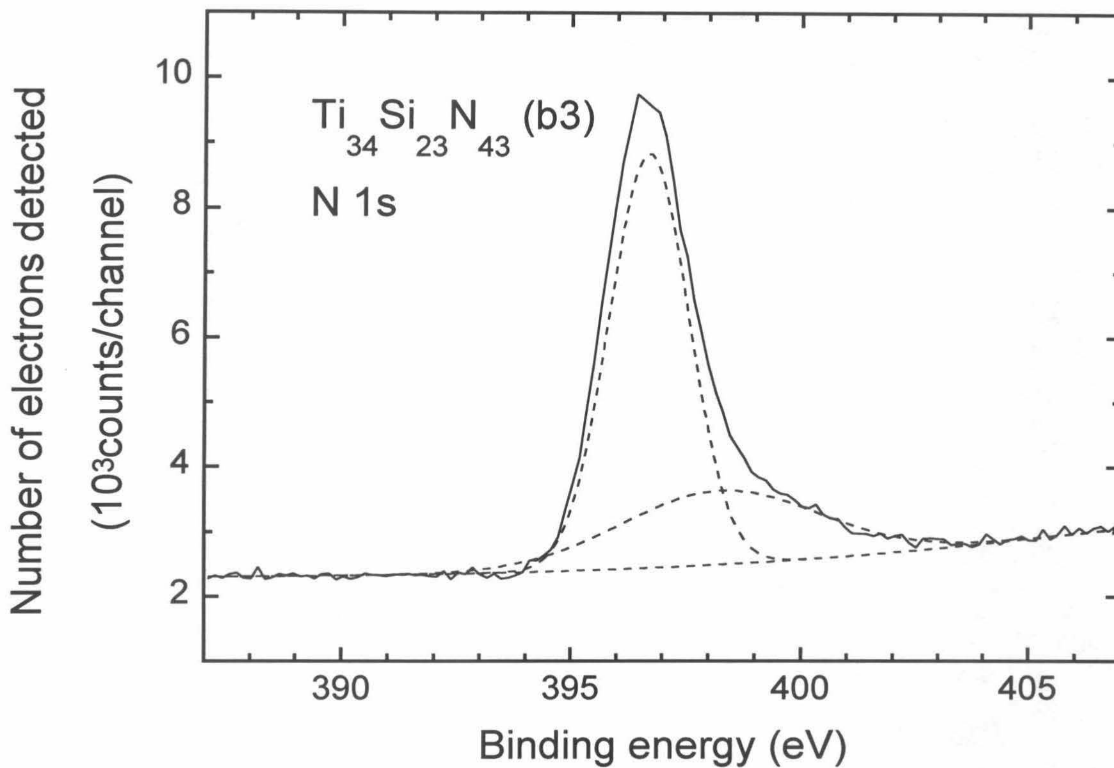


FIG. 2.9. The N-1s photoemission spectrum of $Ti_{34}Si_{23}N_{43}$ (b3) film, with double Gaussian simulation.

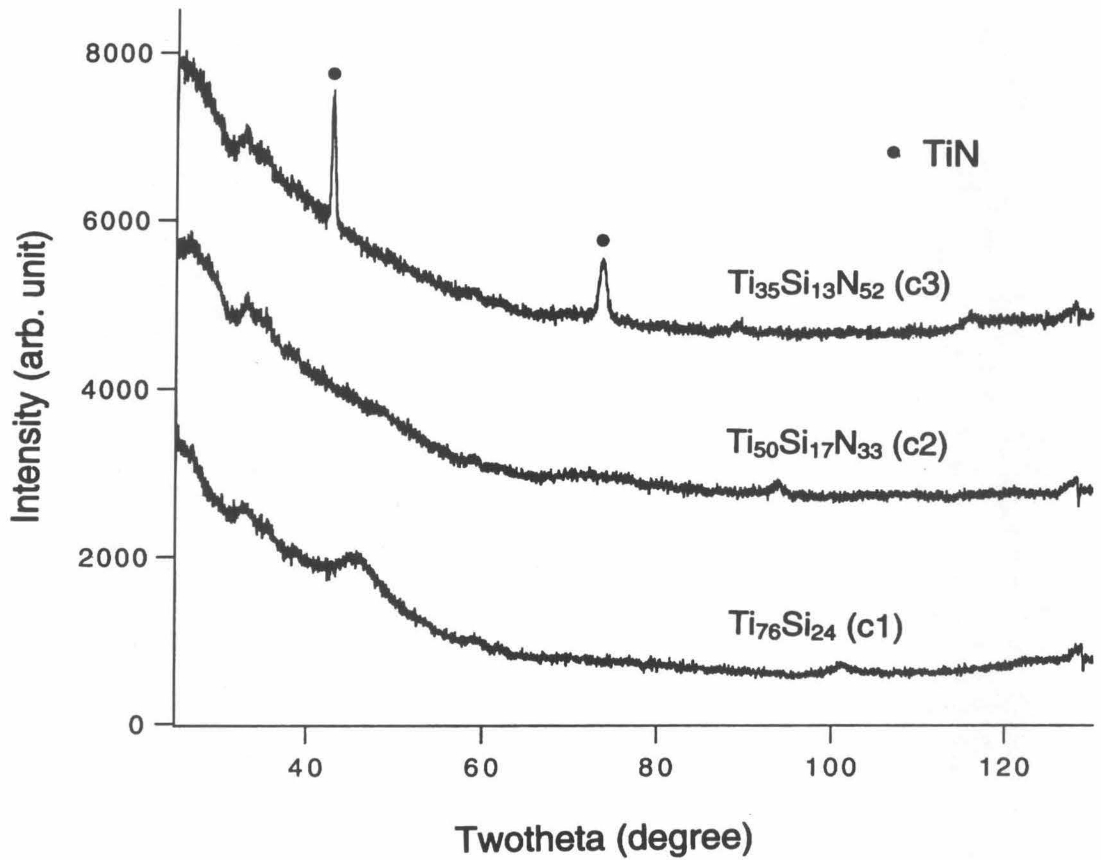


FIG. 2.10. 12°-Glancing angle x-ray diffraction spectra of as-deposited $Ti_{76}Si_{24}$ (c1), $Ti_{50}Si_{17}N_{33}$ (c2), and $Ti_{35}Si_{13}N_{52}$ (c3) films, taken with Co $K_{\alpha}$ radiation (0.179 nm).

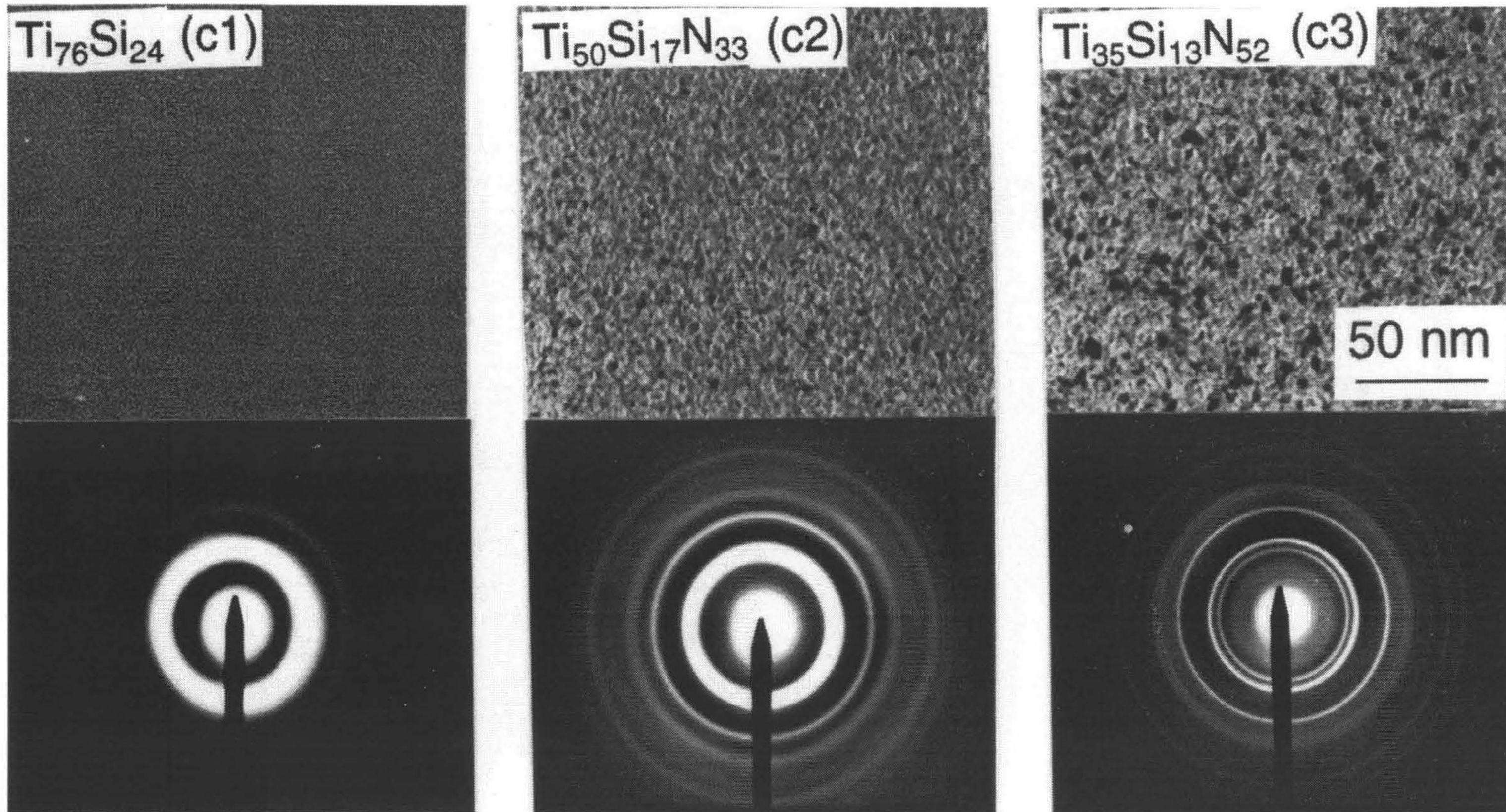


FIG. 2.11. Bright-field transmission electron micrographs (plan-view) of as-deposited $Ti_{76}Si_{24}$ (c1), $Ti_{50}Si_{17}N_{33}$ (c2), and $Ti_{35}Si_{13}N_{52}$ (c3) films reactively sputtered from a $Ti_3Si$ target. Compare with Fig. 2.10

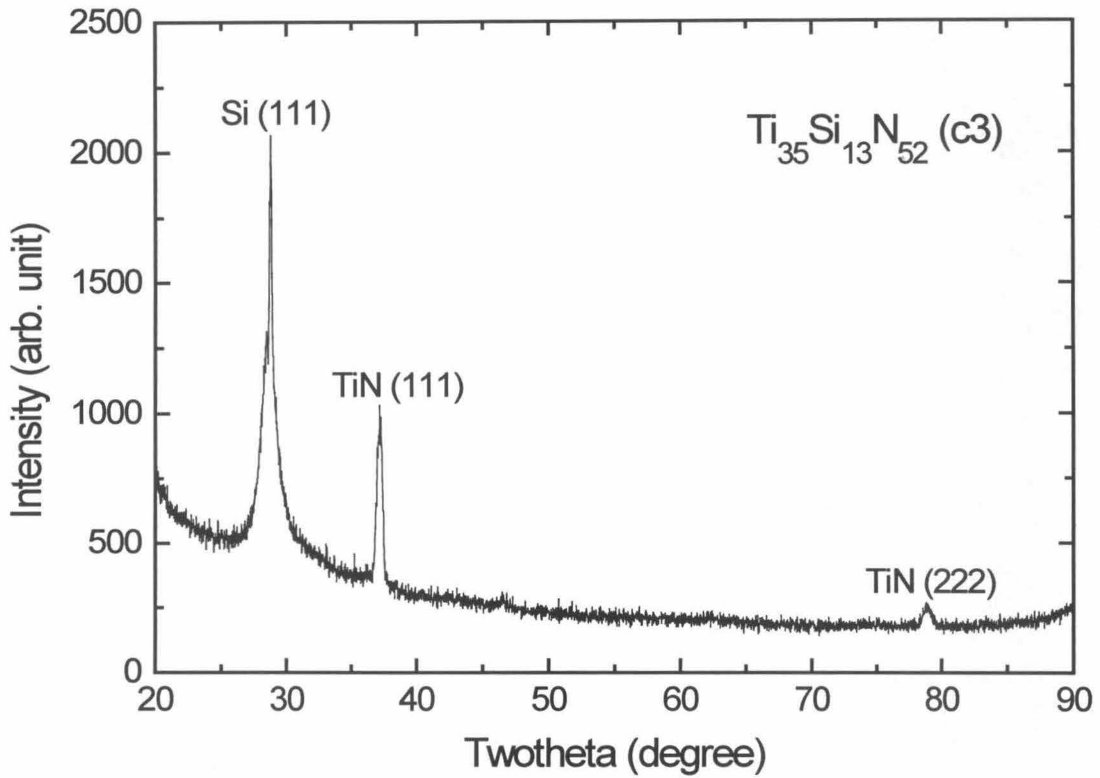


FIG. 2.12. Theta-twotheta x-ray diffraction spectrum of $Ti_{35}Si_{13}N_{52}$ (c3) film on oxidized Si substrate, taken with Cu $K_{\alpha}$ radiation (0.154 nm).

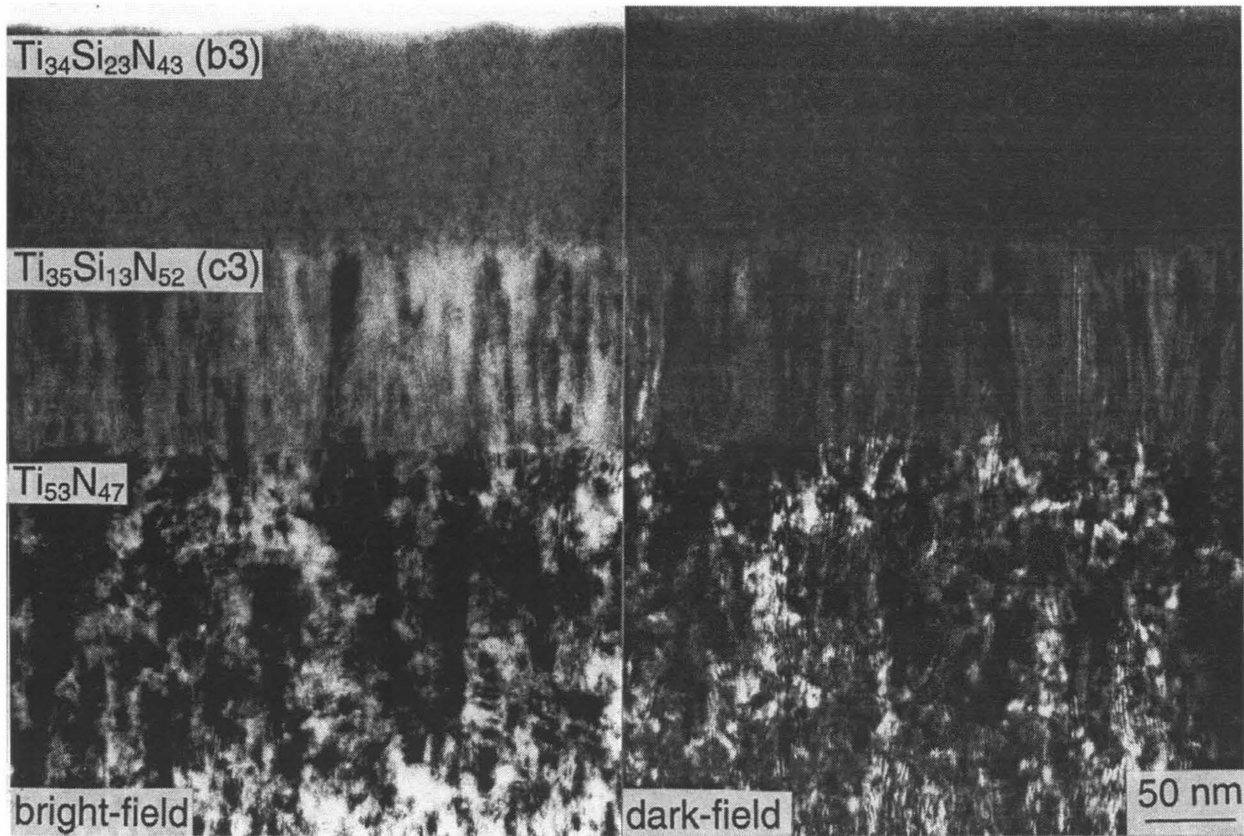


FIG. 2.13. Cross-sectional transmission electron micrographs (bright-field and dark-field pair) of three layers of reactively sputtered TiN (bottom), $Ti_{34}Si_{23}N_{43}$ (b3, center) and $Ti_{35}Si_{13}N_{52}$ (c3, top) films on a 6H-SiC substrate.

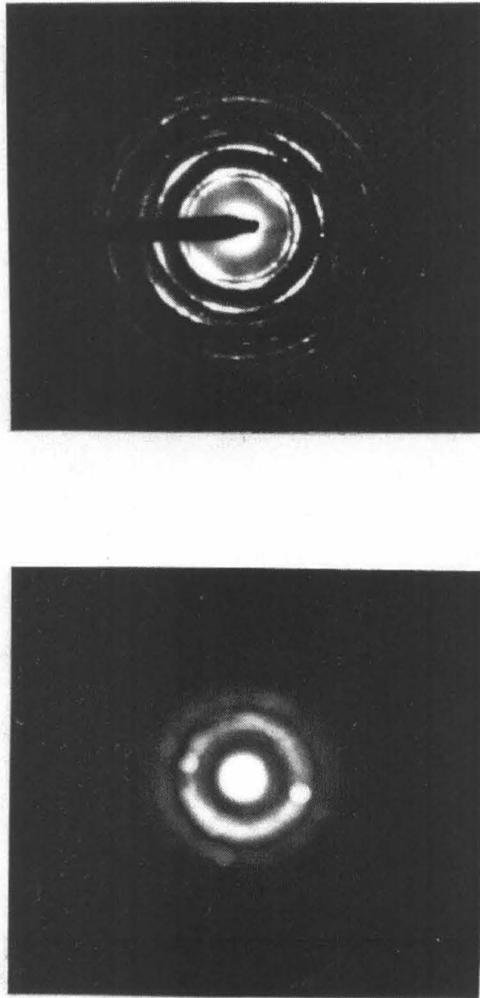

FIG. 2.14. Diffraction pattern of the three layers shown in Fig. 2.13 with a 0.5 μm aperture and a parallel beam (top), and that of the $Ti_{34}Si_{23}N_{43}$ (b3) layer with no aperture and a focused beam (bottom).

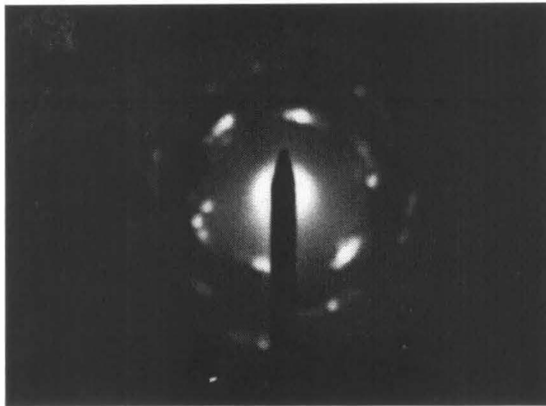

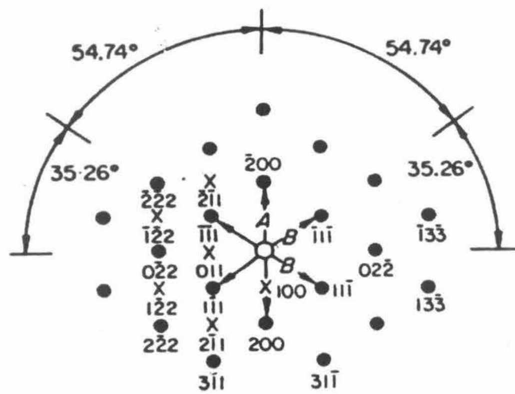


$$\frac{A}{B} = \frac{2}{\sqrt{3}} = 1.155 \qquad B = z = \langle 110 \rangle$$

FIG. 2.15. Electron diffraction pattern of the $Ti_{35}Si_{13}N_{52}$ (c3) film (top) on oxidized Si substrate; and that of standard for the <110> zone axis of an fcc lattice (bottom).

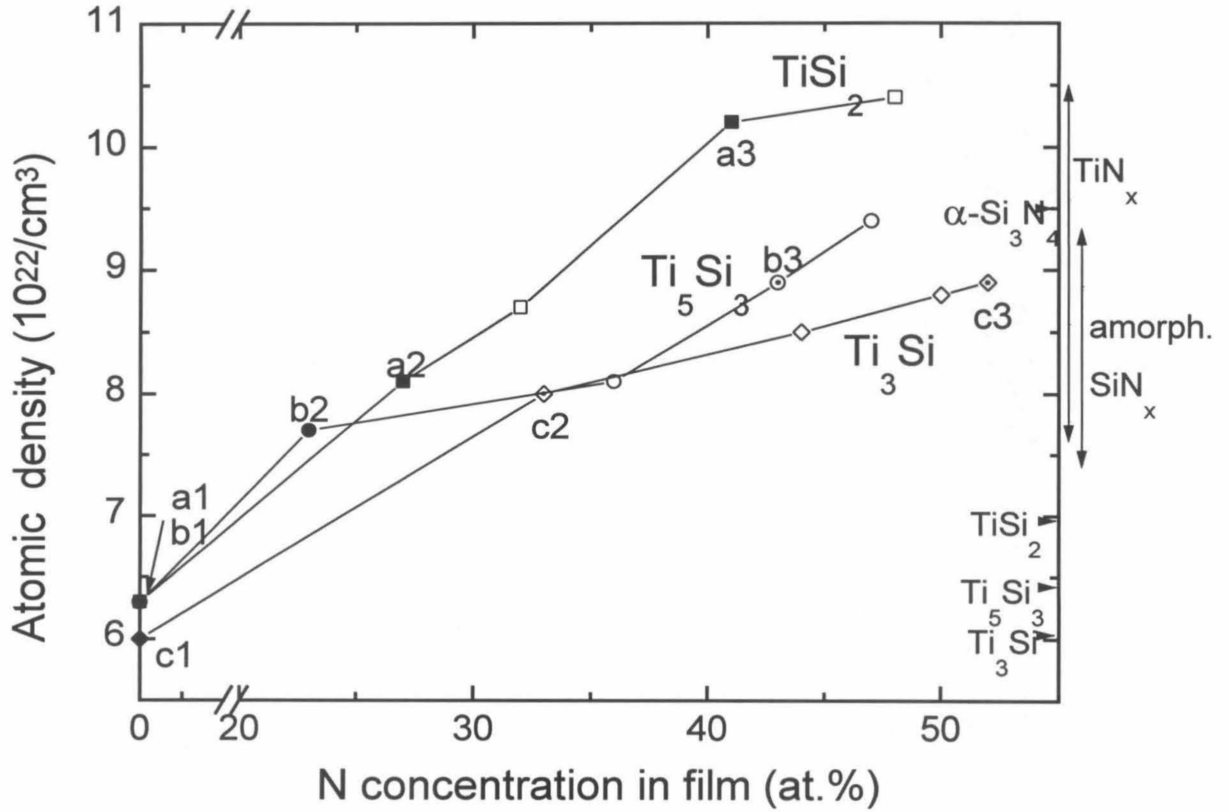


FIG. 2.16. Atomic density of the Ti-Si-N films reactively sputtered from a $TiSi_2$, a $Ti_5Si_3$, or a $Ti_3Si$ target. The symbols used agree with those in Fig. 2.1.

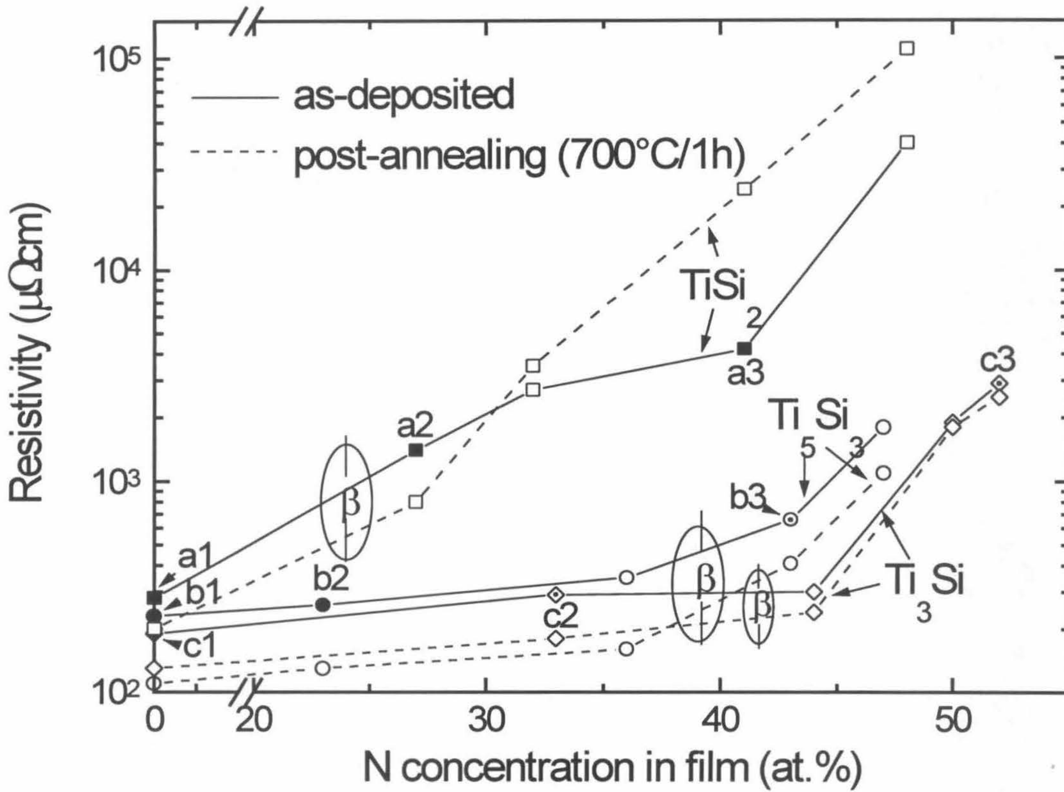


FIG. 2.17. Resistivity of Ti-Si-N films reactively sputtered form a $TiSi_2$, a $Ti_5Si_3$, or a $Ti_3Si$ target, as-deposited and annealed at 700 °C for an hour. The symbols used agree with those in Fig. 2.1.

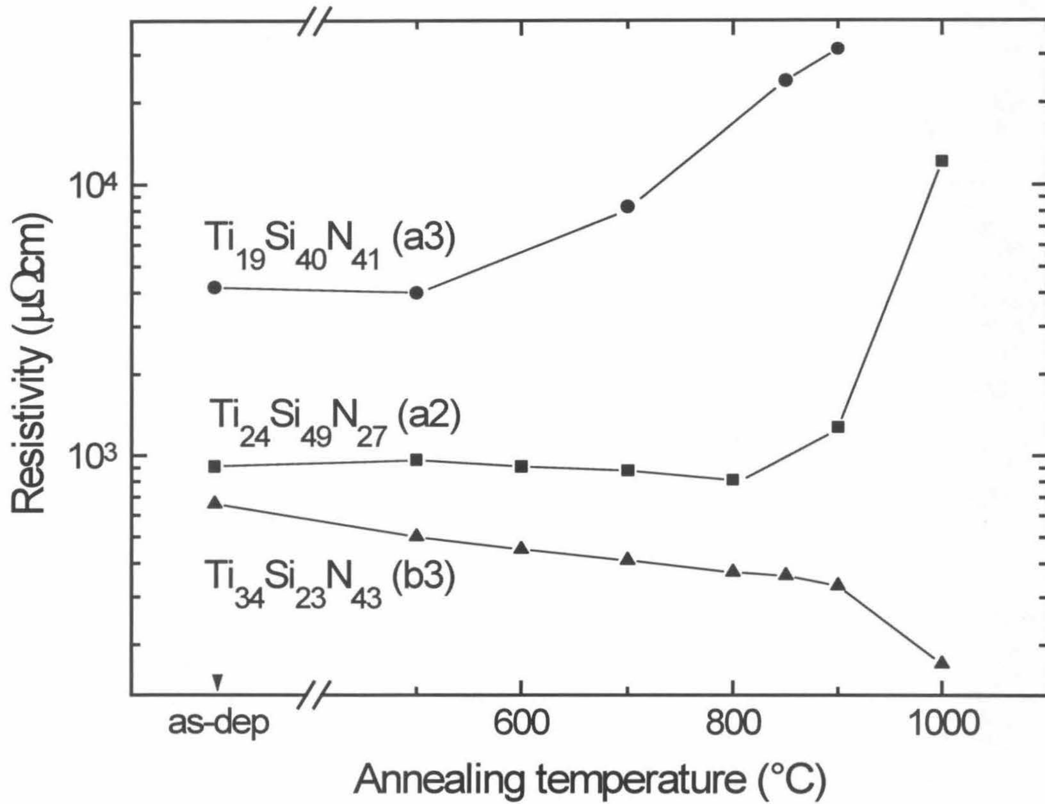


FIG. 2.18. Resistivity of $Ti_{34}Si_{23}N_{43}$ (b3), $Ti_{24}Si_{49}N_{27}$ (a2), and $Ti_{19}Si_{40}N_{41}$ (a3) films as-deposited and after 1 hour annealing at a temperature ranging from 500 to 1000 °C.

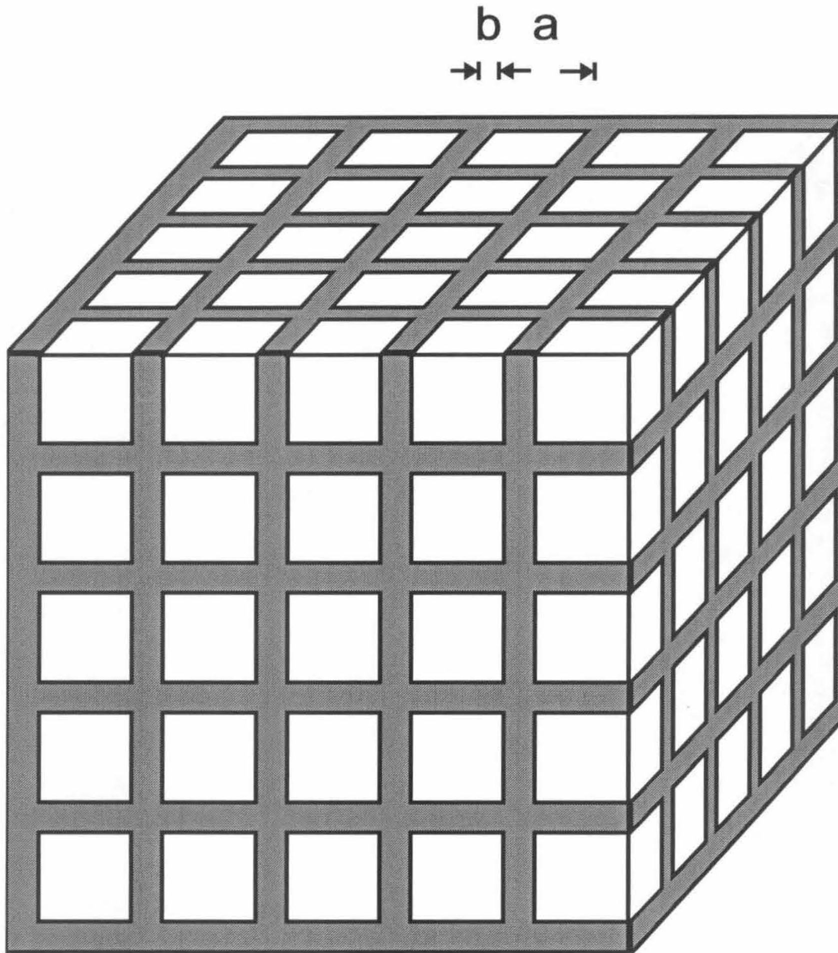


FIG. 2.19. Simplified structure model of annealed $Ti_{19}Si_{40}N_{41}$ (a3) films, for resistivity analysis.

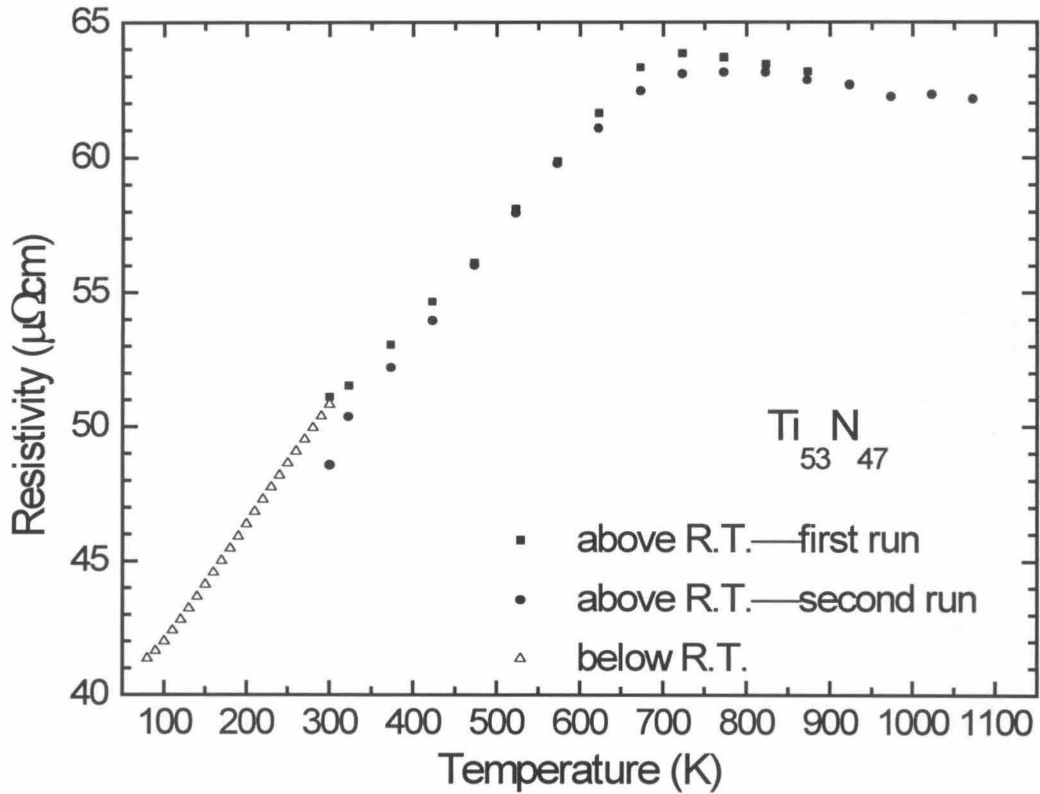


FIG. 2.20. Resistivity of the as-deposited $Ti_{53}N_{47}$ film from 80 to 1073 K.

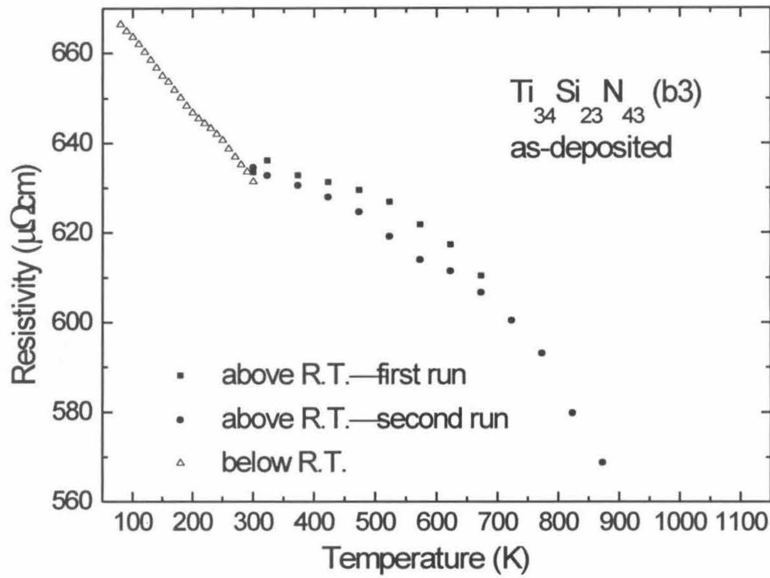


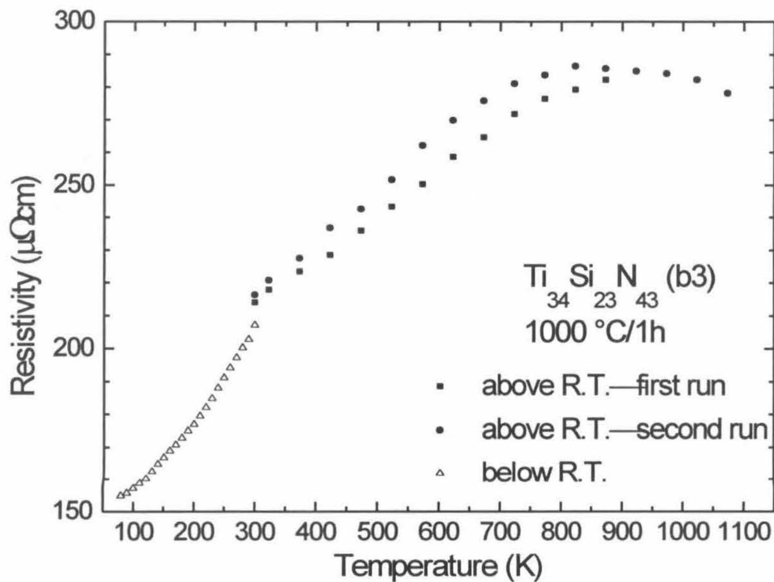


FIG. 2.21. Resistivity of the as-deposited $Ti_{34}Si_{23}N_{43}$ (b3) film from 80 to 873 K (top), *I dem* for a sample after 1 hour vacuum annealing at 1000 °C, from 80 to 1073 K (bottom).

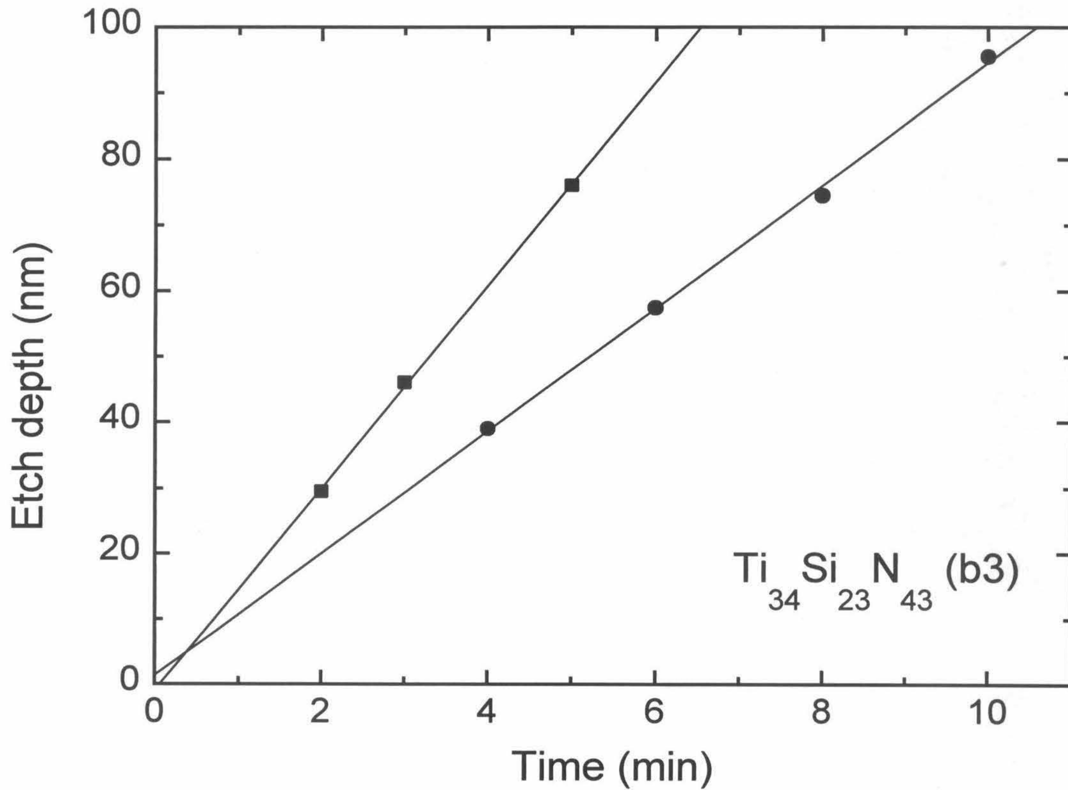


FIG. 2.22. $Ti_{34}Si_{23}N_{43}$ (b3) etch depth as a function of etch duration for 20 % $O_2$:80 % $CF_4$ gas composition, 40 sccm total flow rate, 80 mTorr pressure, 140 W cathode power (circle), and 50% $O_2$:50% $CF_4$ gas composition, 40 sccm total flow rate, 150 mTorr pressure, 140 W cathode power (square).

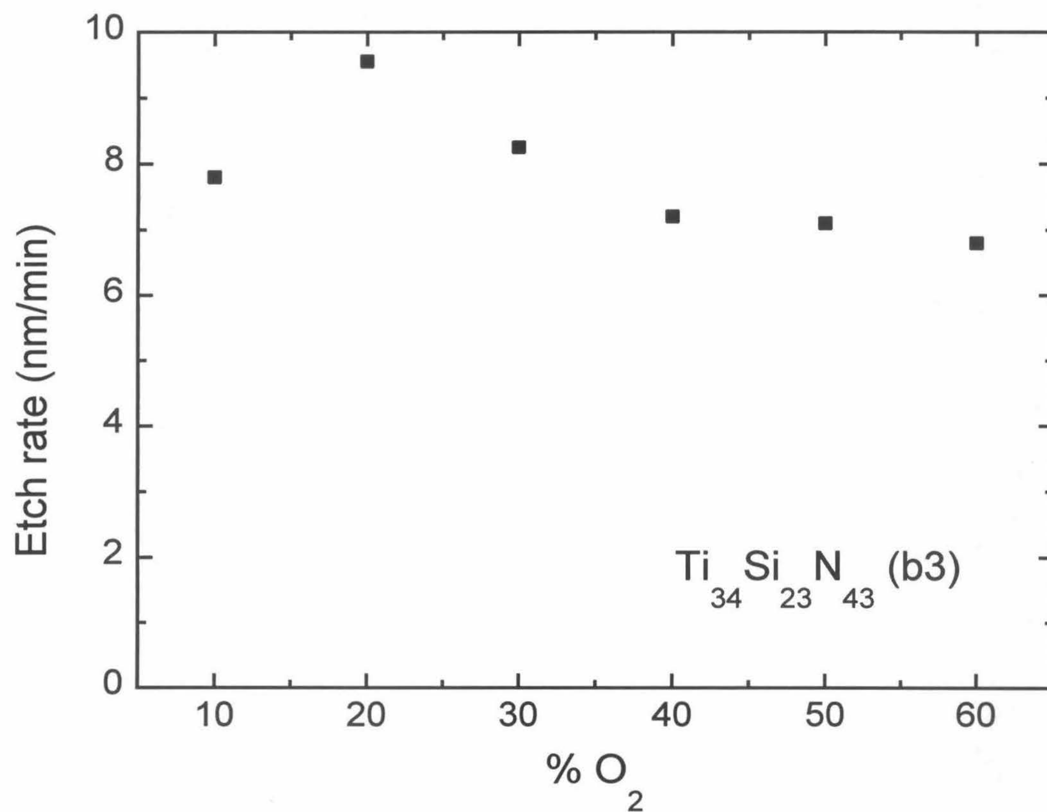


FIG. 2.23. $Ti_{34}Si_{23}N_{43}$ (b3) etch rate as a function of $O_2$ addition to $O_2/CF_4$ gas mixture, with 40 sccm total flow rate, 80 mTorr pressure, 140 W cathode power.

| target | composition | deposition rate (nm/min) | atomic density ($10^{22}$ /cm$^3$) | structure and phases | | resistivity (μΩcm) | |
|---|---|---|---|---|---|---|---|
| | | | as-dep. | as-dep. phase, by TEM | phases at crystallization temp. (°C), by x-ray | as-dep. | 700°C/1h |
| $TiSi_2$ | $Ti_{34}Si_{66}$(a1) | 41 | 6.3 | amorphous | $TiSi_2$ (500) | 280 (17)** | 200 |
| | $Ti_{24}Si_{49}N_{27}$(a2) | 34 | 8.1 | amorphous | TiN+Si (1000) | 1400 | 800 |
| | $Ti_{23}Si_{45}N_{32}$ | 33 | 8.7 | | | 2700 | 3500 |
| | $Ti_{19}Si_{40}N_{41}$(a3) | 28 | 10.2 | amorphous | TiN (1000) | 4200 | 24,000 |
| | $Ti_{17}Si_{35}N_{48}$ | 24 | 10.4 | | | 40,000 | 110,000 |
| $Ti_5Si_3$ | $Ti_{62}Si_{38}$(b1) | 28 | 6.3 | amorphous | $Ti_5Si_3$ (700) | 230 (55)** | 110 |
| | $Ti_{47}Si_{30}N_{23}$(b2) | 19 | 7.7 | amorphous | TiN+TiSi (900) | 260 | 130 |
| | $Ti_{43}Si_{26}N_{31}$ | 19 | 8.1 | | | 350 | 160 |
| | $Ti_{34}Si_{23}N_{43}$(b3) | 19 | 8.9 | TiN (<3 nm) | TiN (1000) | 660 | 410 |
| | $Ti_{31}Si_{22}N_{47}$ | 18 | 9.4 | | | 1800 | 1100 |
| $Ti_3Si$ | $Ti_{76}Si_{24}$(c1) | 35 | 6.0 | amorphous | $Ti_3Si$ (500) | 190 | 130 |
| | $Ti_{50}Si_{17}N_{33}$(c2) | 26 | 8.0 | TiN (<5 nm) | * | 290 | 180 |
| | $Ti_{42}Si_{14}N_{44}$ | 20 | 8.5 | | | 300 | 240 |
| | $Ti_{37}Si_{13}N_{50}$ | 20 | 8.8 | | | 1900 | 1800 |
| | $Ti_{35}Si_{13}N_{52}$(c3) | 18 | 8.9 | TiN (<12 nm) | * | 2900 | 2500 |

* as-deposited crystalline by x-ray

** resistivities in parentheses are those of the crystalline bulk phases [26,27].

TABLE 2.1. Properties of Ti-Si-N films reactively sputtered from a $TiSi_2$, a $Ti_5Si_3$ or a $Ti_3Si$ target.

# Chapter 3 Ti-Si-N Thin Films as Diffusion Barriers Between Si and Al

## 3.1 Experimental procedures

Substrates used in the experiment include bare and oxidized planar (100) Si wafers and wafers patterned with 250×250 $\mu m^2$ $n^+p$ shallow junction diodes. The bare planar Si wafers and those patterned with diodes were cleaned in a solution of concentrated HF diluted with water just before being loaded into the sputtering chamber. The base pressure of the evacuated chamber is around $5 \times 10^{-7}$ Torr, but it rises to $2 \times 10^{-6}$ Torr with the cryopump throttled for sputtering. Ti-Si-N films, about 100 nm thick, were deposited by reactively sputtering a $TiSi_2$, a $Ti_5Si_3$ or a $Ti_3Si$ target in an rf-magnetron sputtering system. The system and the deposition conditions of the barriers are described further in section 2.1. Afterwards, about 350 nm of Al was deposited on top of the Ti-Si-N films without breaking vacuum. The sputtering of the Al was carried out at 300 W forward power and in Ar with 5 mTorr pressure. The substrate holder was set in a rotation mode, in which the samples cyclically pass under an orifice beneath the target where they spend only 1/10 of the total sputtering duration. In this way, the sample surface is kept at a moderate temperature to avoid a rough surface morphology, or excessively heating the photoresist, when present on the substrate. The substrate holder was biased at -50 V during the metal depositions. Some samples were then annealed in a quartz-tube furnace at a pressure of less than $1 \times 10^{-6}$ Torr.

Ti-Si-N films of five different compositions were deposited from each target and their barrier performance was evaluated with Al overlayers. The results are summarized

in Table 3.1. The maximum temperature of stability we quote is for 30 min vacuum annealing when, at a 50 °C higher temperature, changes in the layers can readily be detected by optical microscopy or backscattering spectrometry. If no failure was detected by the above methods at temperatures higher than 500 °C, the stability of the barriers was further tested electrically using Si wafers patterned with the $n^+p$ shallow junction diodes, and the maximum temperature of stability, defined in analogous fashion, was then established by monitoring the change in the reverse current of the diodes at -4 V bias. Some barriers were further investigated by 2.0 MeV $^4He^{2+}$ backscattering spectrometry, executed throughout with a 170 ° scattering angle for the detected particles and a 5 °-off-normal beam incidence. X-ray diffractometry with Co $K_\alpha$ radiation ($\lambda$=0.179 nm) and an Inel position-sensitive semi-ring detector, optical microscopy, and scanning electron microscopy equipped with energy-dispersive x-rays analysis were also applied.

A film derived from the $Ti_5Si_3$ target is one of the best barriers between Si and Al in Ti-Si-N system. We thus begin with this type of films and subsequently discuss films obtained from the $TiSi_2$ and $Ti_3Si$ targets in lesser details.

## 3.2 Results

### 3.2.1 Films from the $Ti_5Si_3$ target

The amorphous nitrogenless film of $Ti_{62}Si_{38}$ (b1) is an effective barrier between a Si substrate and Al overlayer up to 500 °C for 30 min annealing in vacuum. Raising the nitrogen content in the film improves the barrier strength slightly (Table 3.1). A

maximum temperature of stability of 550 °C is achieved when the nitrogen concentration exceeds 40 at.%.

The backscattering spectra of three samples with 100 nm nanocrystalline $Ti_{34}Si_{23}N_{43}$ (b3) and 360 nm Al bilayers on Si substrate, as-deposited and those after 30 min annealing at 550 and 600 °C, are presented in Fig. 3.1. In the spectrum of the as-deposited sample, the signal of Si in the barrier layer partly overlaps that of the Al layer. The tail that extends from the right edge of the Ti signal towards its surface energy corresponds to a Ti impurity in the Al layer intermixed during Al sputtering. The spectrum of the 550 °C-annealed sample is equal to that of the as-deposited sample, besides an insignificant difference in the thickness of the layers. After annealing at 600 °C, the backscattering profiles indicate a severe intermixing of the Al and Si layers. Also, the Ti signal has moved to higher energy and changed to a diffuse shape, in accord with a penetration of the Al into the barrier.

The surface morphology of samples with that barrier, as deposited and annealed, was examined by scanning electron microscopy (Fig. 3.2). The as-deposited sample has a smooth surface. After heating at 550 °C, the sample surface roughens and displays hillocks. This sample was dipped in a 40% aqueous solution of HCl at room temperature for 2 min to remove elemental Al. The micrograph of this etched sample shows some tiny white protrusions, one micron or less in size. After sintering at 600 °C, the sample's surface becomes very rough. A large number of "bumps" are presented, with sizes up to 30 μm, and heights of a few microns. They have the appearance of a solidified liquid. An energy-dispersive analysis of x-rays emitted by a 10 keV electron beam (~1 μm

penetration depth) reveals an extreme compositional inhomogenity in the 600 °C-annealed sample. The protrusions are composed mostly of Al, which is depleted in the surrounding area. After this sample is etched in HCl, its SEM micrograph shows an irregular surface, with white protrusion, larger in size than after annealing at 550 °C, and dark areas. An energy-dispersive mapping by electron induced x-rays shows that the white protrusions at the interface after both 550 and 600 °C-annealing are rich in Al and Si and lean in Ti and N.

X-ray diffraction spectra of the as-deposited and annealed samples are shown in Fig. 3.3. That of the as-deposited sample contains only Al peaks. The spectrum remains unchanged after annealing at 550 °C. At 600 °C, the Al peaks sharpen, indicating coarsening of the Al grains. Three new peaks emerge that all belong to the Si phase. The Al-Si binary phase diagram has an eutectic at 577 °C with 12 at.% Si [1]. The above results can thus be explained by the formation of polycrystalline Si precipitates after the solidification of an Al-Si eutectic.

Electrical measurements were performed on Si shallow $n^+p$ junctions with the same barrier and Al overlayers (Fig. 3.4). The histogram of the 42 diodes after 550 °C-annealing displays no statistically significant increase in the reverse current density compared to diodes annealed at 250 °C. The 250 °C heat treatment improves the diode characteristic by annealing out defects generated by sputtering. This result indicates that the shallow junctions are not affected although some white objects are presented at the interface. All diodes are shorted after the 600 °C annealing, with reverse current densities

exceeding $10^{-2}$ A/cm$^2$. That result is consistent with the idea of extensive local eutectic reactions at 600 °C, which consumes Si down through the pn junction of the diodes.

### 3.2.2 Films from the $TiSi_2$ target

The Si-rich barriers obtained from the $TiSi_2$ target are effective between Si and Al up to 400-500 °C. Raising the nitrogen content in the films gradually improves the stability of the metallizations. Table 3.1 shows that with similar nitrogen content, the barriers obtained from the $TiSi_2$ target are less stable than those from the $Ti_5Si_3$ target.

Fig. 3.5 shows a series of scanning electron micrographs of a planar sample with the amorphous $Ti_{19}Si_{40}N_{41}$ (a3) barrier. The as-deposited sample has a smooth surface. Annealing at 300 °C induces the formation of hillocks with a typical size about 1 μm. Aluminum is the only element detected by energy-dispersive x-ray analysis with a 5 keV energy beam (~0.3 μm penetration), both on the planar area and the hillocks. The interface between Al and the barrier film remains smooth, as becomes evident when the Al layer is selectively etched off. These hillocks commonly appear upon annealing at a few hundred degrees in Al films on Si. They are the result of compressive stress relief in the Al film. After annealing at 550 °C, the concentration of hillocks on the surface increases and new features appear, some are as large as 10 μm. Aluminum remains the only element detected with emitted x-rays. When the Al layer is stripped off, a pockmarked surface appears, indicating an obvious selective chemical attack. An energy dispersive x-ray mapping reveals that the lightly-colored protrusions are more silicon-rich and titanium-lean than the surrounding areas. X-ray diffraction of the unetched sample

reveals the formation of $AlTi_3$. Aluminum thus has reacted with the $Ti_{19}Si_{40}N_{41}$ (a3) barrier.

Electrical measurements on shallow junction diodes show that the reverse current remains unchanged after heat treatment up to 500 °C. At 550 °C, all diodes show an increased reverse current. Some interaction with the Si has thus occurred.

### 3.2.3 Films from the $Ti_3Si$ target

The maximum temperature of stability for films derived from the $Ti_3Si$ target reaches 550 °C also. This maximum is achieved with 40 at.% of nitrogen or higher. The surface of the sample <Si>/$Ti_{42}Si_{14}N_{44}$/Al annealed at 550 °C displays only minor hillocking 0.5 μm or less in size, similar to what is observed with the $Ti_{34}Si_{23}N_{43}$ (b3) barrier (Fig. 3.2) at the same temperature. The backscattering spectrum reveals no detectable degradation of the layers. The stability of the layers at this temperature is further certified by electrical measurement of the metallization on shallow junctions. The barrier fails at 600 °C with droplets formation similar to that shown in Fig. 3.2. The polycrystalline Si phase is also detected by x-ray diffractometry. The $Ti_{42}Si_{14}N_{44}$ film has a lower as-deposited resistivity (300 μΩcm) than that of $Ti_{34}Si_{23}N_{43}$ (b3, 660 μΩcm) obtained from the $Ti_5Si_3$ target. That advantage apart, the nitrogen-rich barriers attained from the $Ti_3Si$ and the $Ti_5Si_3$ targets perform very similarly.

### 3.3 Discussion

For both reactively sputtered and chemically vapor-deposited TiN diffusion barriers between Si and Al, a maximum stable temperature of 500 to 550 °C is usually reported in literature [2-8]. The reaction of Al with TiN is one mechanism responsible for this limitation [2]. The interdiffusion of Al and/or Si through the barrier is another mechanism that has been invoked [5]. Both processes have a strongly localized character, usually attributed to the typically columnar structure of TiN films. This structure creates grain boundaries and even microvoids that can extend across the whole film.

The results presented in section 3.2 show that the highest stable temperature achievable with Ti-Si-N barriers between Si and Al is also 550 °C. The as-deposited $Ti_{34}Si_{23}N_{43}$ (b3) consists of nanometer-sized TiN grains embedded in an $SiN_x$-like amorphous matrix (see section 2.3).

The simplified Al-Ti-N and Al-Si-N ternary phase diagrams [9,10] are displayed in Fig. 3.6. The dashed tie-line between Al and $Si_3N_4$ indicates that the formation of a very thin interfacial AlN layer can sometimes block the reactions and establish a metastable condition. The $TiAl_3$ is the only stable phase between Ti and Al. A tie-line connects $TiAl_3$ and AlN, and these two phases equilibrate with TiN or Al. The AlN equilibrates with $Si_3N_4$ and Si. Neither TiN nor $Si_3N_4$ is thus stable in contact with Al, although both are stable with Si.

An experiment with a bilayer of $Ti_{34}Si_{23}N_{43}$ (b3) and Al on a $SiO_2$ substrate shows that the layers react strongly at 600 °C. It thus appears that the failure of the near-amorphous $Ti_{34}Si_{23}N_{43}$ (b3) layer is initiated by its reaction with Al. Once this reaction

has brought Al and Si into (local) contact with each other and the temperature exceeds their eutectic point at 577 °C, a liquid phase can appear. An eutectic exist in the Al-Si diagram at 577 °C [1]. The presence of the apparently solidified droplets after a 600 °C annealing strongly suggests such an eutectic reaction in the final stages of the breakdown.

The barrier of $Ti_{42}Si_{14}N_{44}$ obtained from the $Ti_3Si$ target has the same maximum temperature of stability as $Ti_{34}Si_{23}N_{43}$ (b3) from the $Ti_5Si_3$ target. The breakdown occurs at 600 °C also and in a very similar fashion. The Si-rich films obtained from the $TiSi_2$ target are generally slightly inferior barriers between Al and Si compared to those deposited from the other two targets.

Some ternary amorphous barriers of the class TM-Si-N (TM=Ta, Mo, W) can successfully sustain annealing above the Al melting point, although they are also thermodynamically unstable with Al [11,12]. It was established that thin (3 nm) AlN layer forms at the interface in the case of the amorphous barrier $W_{36}Si_{14}N_{50}$ with an Al overlayer and blocks further reaction [12]. In contrast, the $Ti_{34}Si_{23}N_{43}$ (b3) investigated here is a phase-separated layer on the nanometer scale. We conjecture that in this case, a laterally uniform reaction between Al and the barrier may not occur, and that this is the reason why the reaction between Al and the barrier can proceed.

Hillocks on the Al layer form most pronouncely on the amorphous $Ti_{19}Si_{40}N_{41}$ barrier (a3) obtained from the $TiSi_2$ target and to a lesser degree on the nanocrystalline $Ti_{34}Si_{23}N_{43}$ (b3) and the $Ti_{42}Si_{12}N_{44}$ from the $Ti_5Si_3$ and the $Ti_3Si$ targets respectively. Hillock formation is the result of the different thermal expansion of Al ($25\times10^{-6}$ $K^{-1}$) and

Si ($3\times10^{-6}$ $K^{-1}$) [13]. Why the number and size of the hillocks differ for the various barriers is not clear.

Exactly how the barrier performance is enhanced by adding nitrogen to the film is a matter that is hard to decide on the basis of our experiments.

### 3.4 Conclusion

Using Ti-Si-N films as diffusion barriers between Si and Al, stability of the metallization against thermal treatment improves with increasing N content, with a fixed Ti to Si ratio. The highest temperature at which large-area shallow $n^+p$ Si diodes patterned with a ~100 nm thick Ti-Si-N barrier and an Al overlayer can be heated for 30 min without degradation is 550 °C, using barriers derived from the $Ti_5Si_3$ or the $Ti_3Si$ targets with ~ 45 at.% of nitrogen or higher. This maximum temperature of stability is the same as, or slightly higher than, that of TiN barriers of the same thickness. The failure takes place at 600 °C and is initiated by a reaction of Al with the barrier layer.

## REFERENCES

1. J.L. Murray, and A.J. MacAlister, in *Binary Alloy Phase Diagrams*, edited by T. B. Massalski, Vol. 2 (The Materials Information Society, Material Parks, Ohio, 1990).

2. M. Wittmer, J. Appl. Phys. **53**, 1007 (1982).

3. N. Cheung, H. von Seefeld, and M-A. Nicolet, proceedings of the Symposium on Thin Film Interfaces and Interconnections, edited by J. E. E. Baglin and J. M. Poate (The Electrochemical Society, Inc., Princeton, New Jersey, 1980), p323.

4. H. Norström, S. Nygren, P. Wilund, M. Östling, R. Buchta, and C.S. petersson, Vacuum **35**, 547 (1985).

5. S.O. Hyatt, B.S. Chao, and H. Yamauchi, Vacuum, **44**, 1025 (1992).

6. H. Norström, T. Donchev, M. Östling, and C.S. Petersson, Physica Scripta, **28** 633 (1983).

7. L. Krustin-Elbaum, M. Wittmer, C.-Y. Ting, and J.J. Cuomo, Thin Solid Films **104**, 81 (1983).

8. M. Okihara, N. Hirashita, K. Hashimoto, H. Onoda, Appl. Phys. Lett. **66**, 1328 (1995).

9. R. Beyers, R. Sinclair, and M. E. Thomas, J. Vac. Sci. Technol. B **2**, 781 (1984).

10. A.S. Bhansali, D.H. Ko, and R. Sinclair, J. Electron. Mater. **19**, 1171 (1990).

11. E. Kolawa, J.M. Molarius, C.W. Nieh, and M-A. Nicolet, J. Vac. Sci. Technol. **A8**, 3006 (1990).

12. J.S. Reid, E. Kolawa, C.M. Garland, M-A. Nicolet, F. Cardone, D. Gupta, and R.P. Ruiz, J. Appl. Phys., **79**, 1109 (1995).

13. R.E. Bolz, and G.L. Tuve (eds), *CRC Handbook of Tables for Applied Engineering Science* (the Chemical Rubber Co., Cleveland, OH, 1970) pp265-266.

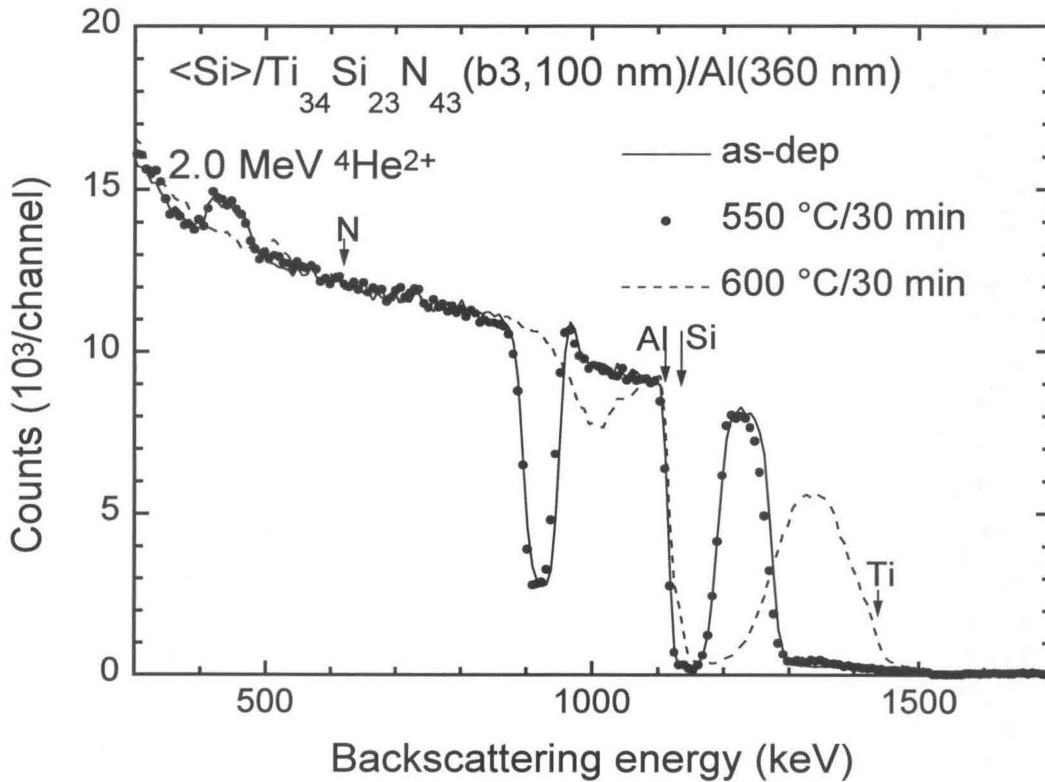


FIG. 3.1. 2.0 MeV $^{4}He^{2+}$ backscattering spectra of a sample <Si>/$Ti_{34}Si_{23}N_{43}$(b3,100 nm)/Al(360 nm), as-deposited and after 30 min annealing in vacuum, at 550 or 600 °C a $SiO_2$ substrate

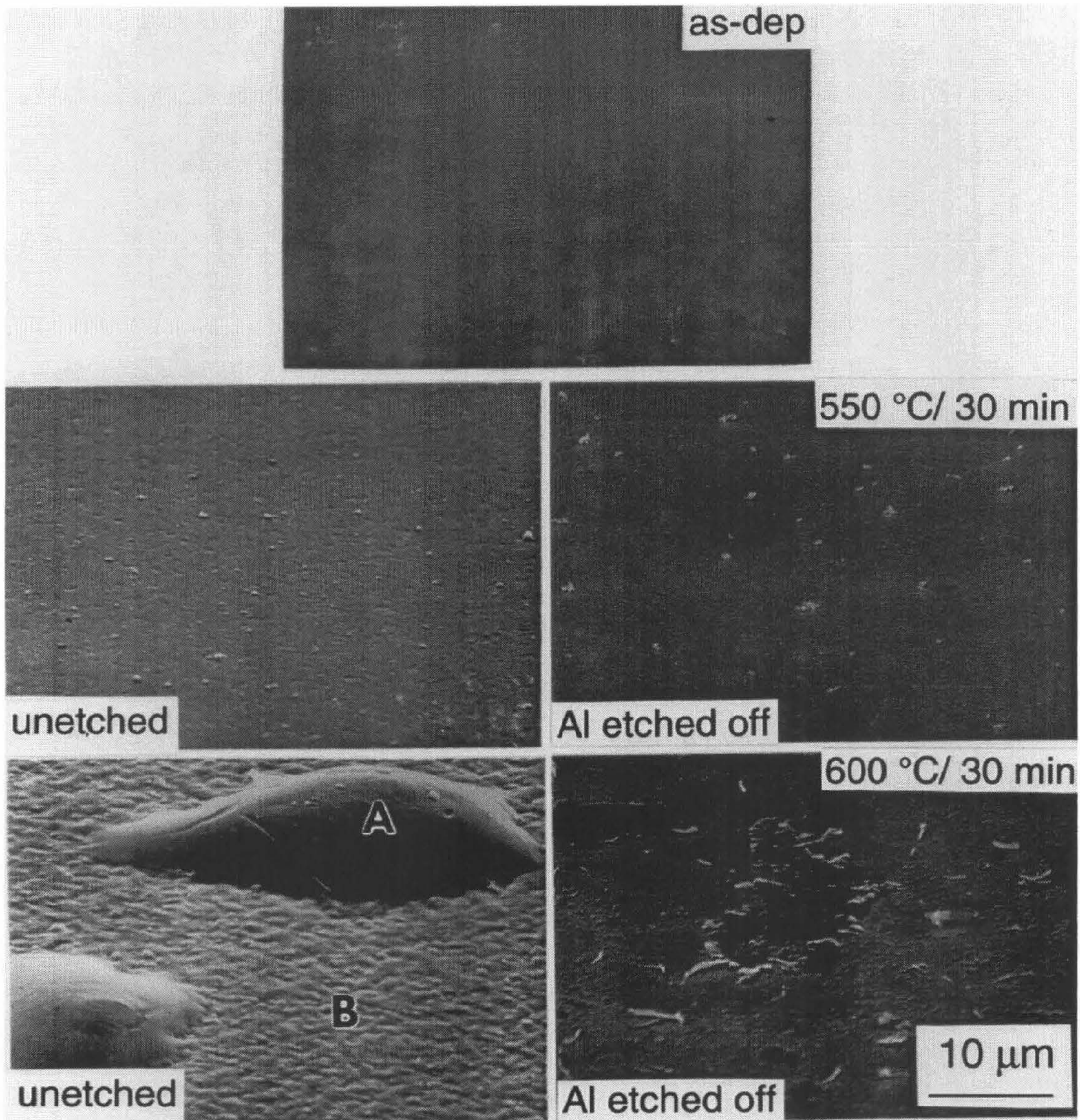


FIG. 3.2. Scanning electron micrograph of a sample <Si>/$Ti_{34}Si_{23}N_{43}$(b3,100 nm)/Al(360 nm), as deposited (top) and after 30 min annealing at 550 (center) or 600 °C (bottom), before (left) and after (right) selective etching in 40% HCl for 2 min at room temperature. The barrier layer (b3) is nanocrystalline.

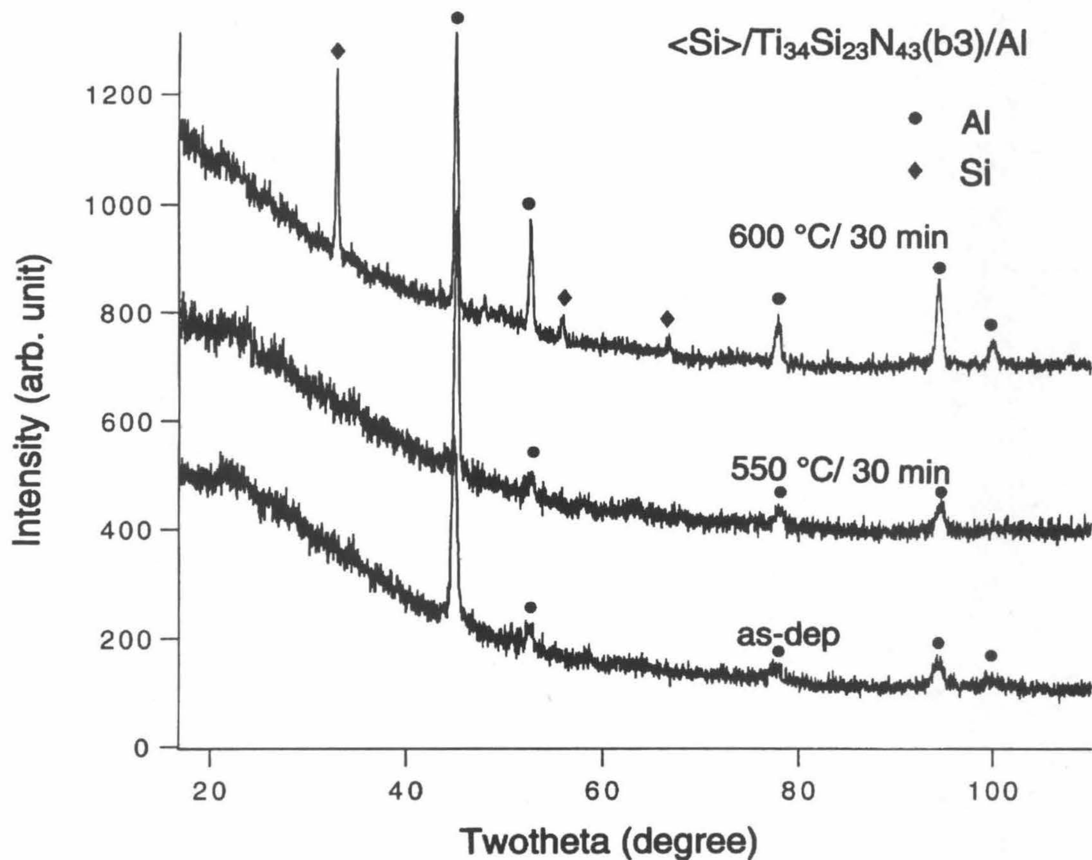


FIG. 3.3. X-ray diffraction spectra (taken with Co $K_\alpha$ radiation, $\lambda$=0.179 nm) of a sample <Si>/$Ti_{34}Si_{23}N_{43}$(b3,100 nm)/Al(360 nm), as-deposited and after 30 min annealing at 550 or 600 °C.

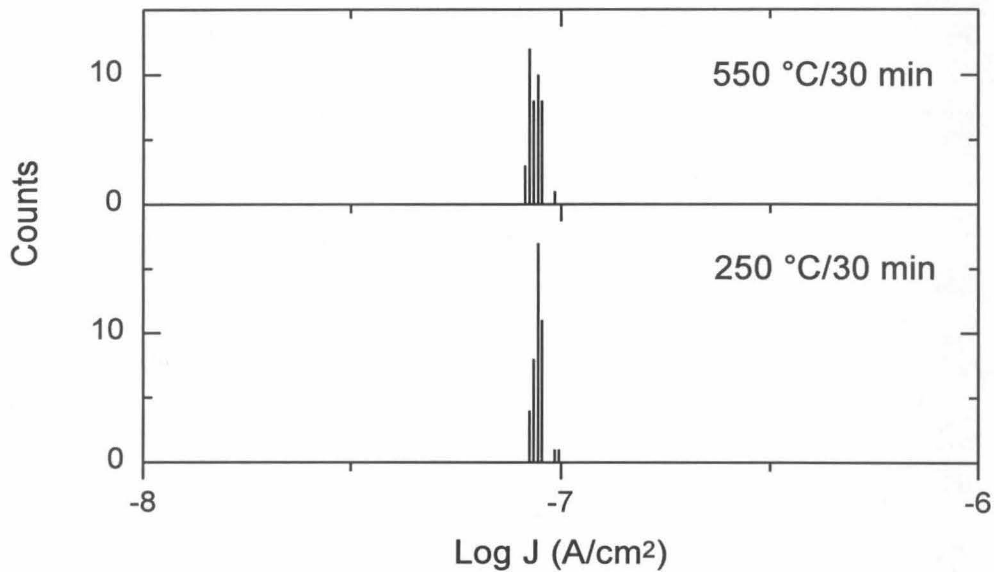


FIG. 3.4. Histograms of the measured reverse current density at -4 V bias and room temperature of 42 Si $n^+p$ shallow junctions with a 100 nm thick nanocrystalline $Ti_{34}Si_{23}N_{43}$ (b3) barrier layer and a 360 nm Al overlayer after 30 min annealing at 250 and 550 °C.

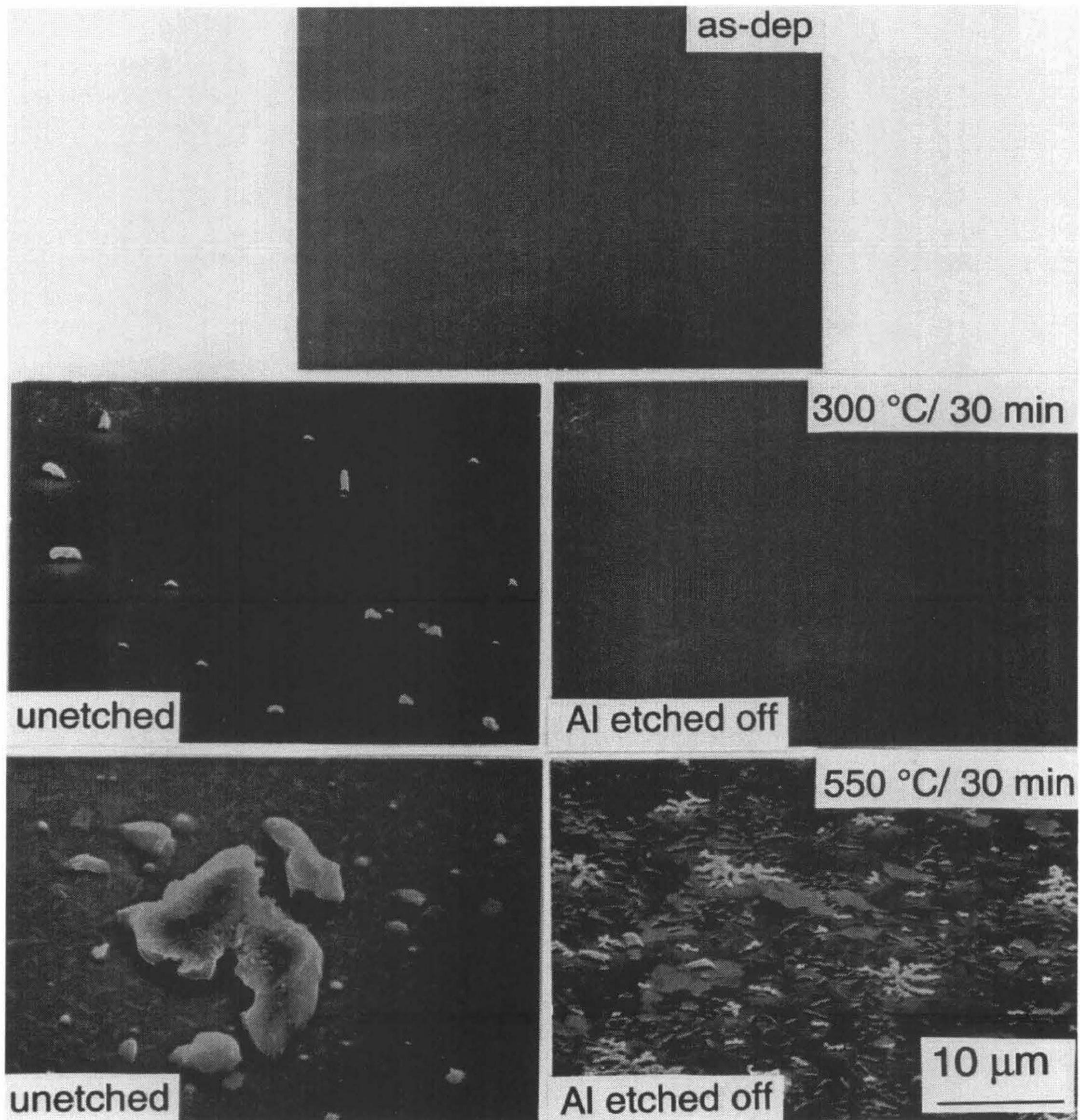


FIG. 3.5. Scanning electron micrographs of a sample <Si>/$Ti_{19}Si_{40}N_{41}$(a3,100 nm)/Al(350 nm), as-deposited (top), and after 30 min annealing at 300 or 550 °C, before (left) and after (right) selective etching in 40 % HCl for 2 min at room temperature. The barrier layer (a3) is amorphous.

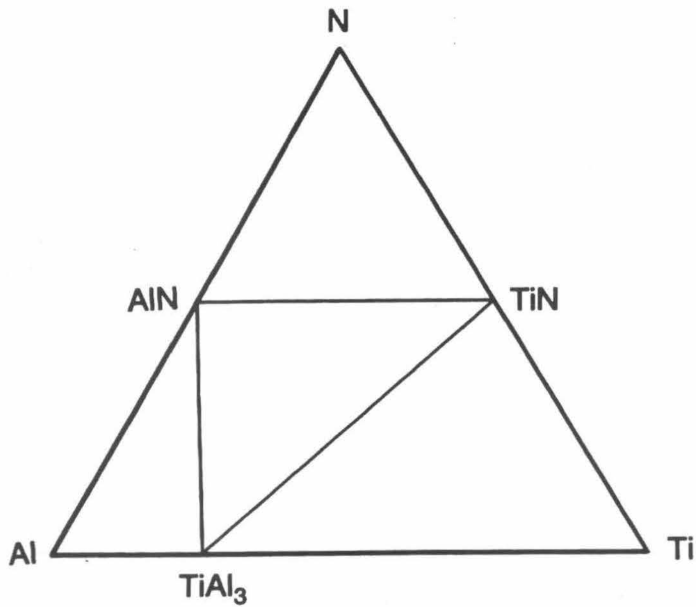


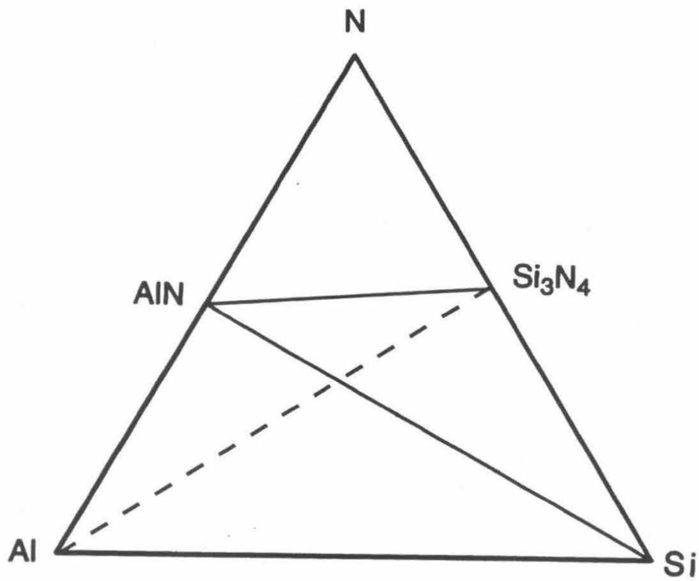


FIG. 3.6. Simplified phase diagrams of Ti-N-Al and Si-N-Al systems at 600 °C. The Al-Ti-N diagram is the simplified version of Beyer et al. [9] at 600 °C. The Al-Si-N diagram is that of Bhansali et al. for 627 °C [10].

| target | composition | maximum temperature of stability (°C) | | |
|---|---|---|---|---|
| | | Si/barrier/Al | Si/barrier/Cu | $SiO_2$/barrier/Cu |
| $TiSi_2$ | $Ti_{34}Si_{66}$(a1) | 400 | 200 | 200 |
| | $Ti_{28}Si_{56}N_{16}$ | 450 | 450 | 450 |
| | $Ti_{24}Si_{49}N_{27}$(a2) | 500 | 500 | 500 |
| | $Ti_{23}Si_{45}N_{32}$ | 500 | 550 | 550 |
| | $Ti_{19}Si_{40}N_{41}$(a3) | 500 | 850 | 900 |
| $Ti_5Si_3$ | $Ti_{62}Si_{38}$(b1) | 500 | 400 | 600 |
| | $Ti_{47}Si_{30}N_{23}$(b2) | 500 | 450 | 550 |
| | $Ti_{43}Si_{26}N_{31}$ | 500 | 400 | 550 |
| | $Ti_{34}Si_{23}N_{43}$(b3) | 550 | 850 | 900 |
| | $Ti_{31}Si_{22}N_{47}$ | 550 | 850 | 900 |
| $Ti_3Si$ | $Ti_{76}Si_{24}$(c1) | 400 | 450 | 450 |
| | $Ti_{50}Si_{17}N_{33}$(c2) | 400 | 250 | 300 |
| | $Ti_{42}Si_{14}N_{44}$ | 550 | 600 | 700 |
| | $Ti_{37}Si_{13}N_{50}$ | 550 | 650 | 800 |
| | $Ti_{35}Si_{13}N_{52}$(c3) | 550 | 700 | 850 |
| $Mo_5Si_3$ | $Mo_{36}Si_{17}N_{47}$ | 675/10 min [3.12] | 800 [2.6] | |
| $W_5Si_3$ | $W_{38}Si_{15}N_{47}$ | | 800 [2.6] | |
| | $W_{36}Si_{14}N_{50}$ | 675/10 min [3.12] | 750 [4.10] | |
| $Ta_5Si_3$ | $Ta_{36}Si_{14}N_{50}$ | 675/30 min [3.11] | 900 [4.4] | |

TABLE 3.1. Maximum temperature of stability of Ti-Si-N films about 100 nm-thick between Si and Al, Si and Cu, or thermally grown $SiO_2$ and Cu. The metal overlayers are 350 to 450 nm thick. The maximum temperature of stability is that temperature, 50 °C above which a degradation is observed upon vacuum annealing for 30 min. For details see section 3.1.

# Chapter 4 Ti-Si-N Thin Films as Diffusion Barriers Between Si and Cu

## 4.1 Experimental procedures

The experimental procedures are the same as those discussed in section 3.1. The sputter-deposition of Cu was accomplished in exactly the same way as for Al.

Films of five different compositions were deposited from each target and their barrier performance on Si substrate was evaluated with Cu overlayers (see Table 3.1). The maximum temperature of stability we quote is for 30 min vacuum annealing when, at a 50 °C higher temperature, changes in the layers can readily be detected by optical microscopy or backscattering spectrometry. If no failure was detected by the above methods at temperatures higher than 500 °C, the stability of the barriers was further tested electrically using the Si wafers patterned with the $n^+p$ shallow junction diodes, and the maximum temperature of stability, defined in analogous fashion, was then established by monitoring the change in the reverse current of the diodes at -4 V bias. The effectiveness of the barriers sandwiched between thermal $SiO_2$ and Cu is evaluated by backscattering.

The 100 nm-thick film with the best barrier performance between a (100) Si substrate and a Cu overlayer about 400 nm thick is one derived from the $Ti_5Si_3$ target. We thus begin with this type of films. The nitrogen-free titanium silicides films nonreactively deposited from the three targets are discussed in detail as well, as few results have been reported before for such barriers with Cu.

## 4.2 Results

### 4.2.1 Films from $Ti_5Si_3$ target

The maximum temperature of stability of films about 100 nm thick between a (100) Si substrate, with or without a thermally grown oxide layer, and a Cu overlayer about 400 nm thick is listed in Table 3.1. A discontinuity in this maximum temperature as a function of nitrogen concentration occurs at about 40 at.% regardless of the substrate. Below this concentration, the maximum temperature of stability varies from 200 to 600 °C, and is never lower on oxidized Si substrate than it is on bare Si substrate. Above 40 at.% nitrogen, the maximum temperature of stability jumps up to 850 and 900 °C on Si and $SiO_2$ substrates, respectively.

After annealing at 450 °C, the surface of the degraded sample <Si>/$Ti_{62}Si_{38}$(b1)/Cu with an amorphous nitrogen-free barrier changes from a shining silverish to a dark color. Backscattering spectrometry of this sample reveals that Cu is present all the way to the substrate (Fig. 4.1, top). The $\eta''$-$Cu_3Si$ [1] and the $Ti_5Si_3$ phases are recognized by x-ray diffraction.

For the same amorphous $Ti_{62}Si_{38}$ (b1)/Cu structure on oxidized silicon, no such interaction can be detected by optical microscopy, backscattering spectrometry, or x-ray diffractometry below or at 600 °C. After annealing at 650 °C, optical microscopy of the sample's surface still shows no detectable degradation. Nevertheless, the backscattering profile of the layers (Fig. 4.2, top) starts to deviate from that of the as-deposited sample: a slight increase in the background signal is observed between the Cu and the Ti signals, implying that Cu may have started to interact with the barrier layer. A further increase in

this signal is found after the sample is annealed at 700 °C, and the sample surface lightens in color. Crystallization of the barrier is observed at 500 °C by x-ray diffraction. This crystallization temperature is 200 °C below that observed without the Cu overlayer (see section 2.3a). No phases other than Cu and $Ti_5Si_3$ are detected in the x-ray diffraction spectrum after annealing at 700 °C.

With the barrier of nanocrystalline $Ti_{34}Si_{23}N_{43}$ (b3), no failure was detected by backscattering spectrometry or scanning electron microscopy after the sample was annealed below or at 850 °C on either a bare or an oxidized Si substrate. After annealing at 900 °C, the backscattering spectrum indicates no detectable intermixing of the layers on $SiO_2$ (not shown), while on Si it shows a barely detectable rise of the signal level below the low-energy edge of the Cu signal (Fig. 4.3).

The as-deposited, 850 and 900 °C-annealed samples on Si substrate were further examined by scanning electron microscopy (Fig. 4.4). The surface of the sample after 850 °C-annealing appears rough but is free of distinctive features. Circular holes up to 10 μm in diameter emerge when the sample is heated at 900 °C. Analysis by energy-dispersive x-rays shows that the region inside a hole contains significant amounts of Ti and Si, while the edge of a hole is composed mainly of Cu and contains elements at about the same relative ratio as an area outside of a hole. These results indicate that there is a sink of Cu at the center. X-ray diffraction results suggest that TiN crystallites have formed, but no Cu-Si compounds is detected. The crystallization does not take place at lower temperatures. It is related to the presence of the Cu overlayer, as the barrier itself, according to x-ray diffraction, does not crystallize until 1000 °C (see section 2.3.1).

Metallizations with the same barrier and Cu overlayer on shallow Si $n^+p$ junctions were characterized by monitoring the reverse current at -4 V bias after annealing at 250, 850, and 900 °C for 30 min. The histograms were reported in ref. 2. No increase in the reverse current is observed in 42 diodes measured up to 850 °C, compared to those annealed at 250 °C. At 900 °C, the reverse current density of about 30% of the diodes has increased, and only for a few by an order of magnitude or more. It was also reported in ref. 2 that a 10 nm-thick film of $Ti_{34}Si_{23}N_{43}$ (b3) between shallow Si junctions and Cu overlayers maintains the electrical characteristic of the diodes up to 650 °C.

This maximum temperature of stability of 850 °C (100 nm barrier) is above the Si/Cu eutectic of 802 °C. Futhermore, the $Ti_{34}Si_{23}N_{43}$ (b3) has a quite acceptable resistivity of 660 μΩcm as-deposited, and lower when annealed (see section 2.5).

### 4.2.2 Films from $TiSi_2$ target

The maximum temperature of stability of the barrier/Cu bilayers on (100) Si and on $SiO_2$ is nearly the same at a fixed barrier composition, and initially increases monotonically with nitrogen content in the barrier (Table 3.1). There is a noticeably enhanced increase above 40 at.% nitrogen, as for the $Ti_5Si_3$-derived barriers. The highest temperature of stability is also about the same (850 or 900 °C).

The nitrogen-free amorphous $Ti_{34}Si_{66}$ (a1) film fails as a barrier at as low as 250 °C, on either bare or oxidized Si substrate. At that temperature, no changes could be detected by inspecting the sample surface under the optical microscope, although backscattering spectrometry does unveil a faint onset of the intermixing of the Cu and the

barrier layers. After annealing at 300 °C, the surface of the samples still remains smooth and shiny, but has changed to a lighter color. The combined information of backscattering spectrometry (Fig. 4.1, center) and x-ray diffractometry (not shown) of the layers on Si substrate indicates that Cu has reacted with the barrier and a layer of $\gamma$-$Cu_5Si$ [3] has formed. The backscattering spectra of Fig. 4.1 (center) implies that the failure starts from the reaction between Cu and the barrier, since the depth profile of the Cu layer only changes near the barrier/Cu interface. Similar spectra were taken with the layers on oxidized Si substrate (Fig. 4.2, center). They also start to degrade at 250 °C.

The most effective barrier sputtered from the $TiSi_2$ target is that with the most nitrogen, $Ti_{19}Si_{40}N_{41}$ (a3), which is amorphous in structure. The stability of the metallization was evaluated by electrical measurement with samples on shallow Si $n^+p$ junction diodes. All the 42 diodes tested maintain a reverse current density between 4.7 and $4.9 \times 10^{-8}$ A/cm$^2$ at -4V bias after annealing at 850 °C, as those heat-treated at 250 °C for defect recovery. After sintering at 900 °C, 95% of the diodes show an increased reverse current density up to $6.6 \times 10^{-3}$ A/cm$^2$ (Fig. 4.5). Fig. 4.6 shows a typical local failure area. Local reaction spots up to 100 μm in size are formed at this temperature. No crystallization of the barrier or formation of intermetallic compound is detected by x-ray diffraction at 900 °C.

Although this film works as effectively as the $Ti_{34}Si_{23}N_{43}$ (b3) film as a barrier, it has a much higher electrical resistivity of 4200 μΩcm as deposited, and the value rises after heat treatment (see section 2.5).

### 4.2.3 Films from $Ti_3Si$ target

The maximum temperature of stability of a 100 nm barrier on a (100) Si or a $SiO_2$ substrate and with a 350 nm Cu overlayer is listed in Table 3.1. The amorphous barrier of $Ti_{76}Si_{24}$ (c1) prevents reaction of the Si substrate with the Cu overlayer up to 450 °C, which is higher than the maximum temperature of stability of the barriers nonreactively sputtered from the other two targets. However, the metallization becomes less stable when nitrogen is added to 33 at.% (c2). This circumstance is not observed in barriers deposited from the other two targets. Further increase of the nitrogen content significantly improves the effectiveness of the barrier. For a $SiO_2$ substrate, the maximum temperature of stability is higher than on Si substrate, with the possible exception at low nitrogen concentrations. The best barrier derived from the $Ti_3Si$ target is columnar $Ti_{35}Si_{13}N_{52}$ (c3). It is effective up to 700 and 850 °C respectively on Si and $SiO_2$ substrates.

Backscattering spectrometry shows no detectable intermixing of the layers in the as-deposited and 450 °C-annealed samples of <Si>/$Ti_{76}Si_{24}$(c1)/Cu with the amorphous unnitrided barrier, but the metallization fails during annealing at 500 °C, as is indicated by the altered backscattering spectrum (Fig. 4.1, bottom). Only the Cu phase is identified by x-ray diffraction. The sample surface appears free of distinctive features under optical microscopy.

The same barrier between $SiO_2$ and Cu degrades at 500 °C as well. Backscattering results unveil a depth profile similar to that on bare Si substrate (Fig. 4.2, bottom). The sample surface looks smooth under optical microscope.

The structure <Si>/$Ti_{50}Si_{17}N_{33}$(c2)/Cu degrades at 300 °C. The backscattering spectrum of the sample also shows an increased signal level between the Ti high-energy and the Cu low-energy edges. No phase other than Cu is detected by x-ray diffractometry.

Electrical measurement on Si diodes reveals that the columnar barrier $Ti_{35}Si_{13}N_{52}$ (c3) starts to fail at 750 °C (Fig. 4.7). A scanning electron micrograph of that sample shows a pustuled surface with holes on many of the blisters (Fig. 4.8). Cu and TiN are the only phases detected by x-ray diffractometry. In contrast, the same barrier and Cu layers on a $SiO_2$ substrate maintain their structural integrity up to 850 °C. The resistivity of this barrier is about 3900 μΩcm as deposited, and declines upon annealing (see section 2.5).

## 4.3 Discussion

### 4.3.1 General comments

For the purpose of the following discussion, we assume that the metallization can degrade by three distinct modes: 1. reaction between the top layer and the barrier; 2. reaction between the barrier and the bottom (substrate) layer; 3. diffusion of the top or bottom layer material through the barrier followed by reaction. Other mechanisms can be conceived that also lead to the failure of the structure, such as mechanical fracture or decomposition of the barrier. Compelling evidence for such mechanism has never been observed in the course of our work. We therefore feel justified in ignoring them.

In table 4.1, the maximum temperature of stability of the barriers $Ti_{62}Si_{38}$(b1), $Ti_{34}Si_{66}$ (a1), $Ti_{76}Si_{24}$ (c1), $Ti_{34}Si_{23}N_{43}$ (b3), $Ti_{19}Si_{40}N_{41}$ (a3), and $Ti_{35}Si_{13}N_{52}$ (c3) are listed for both a Si and a $SiO_2$ substrate. Also listed are the crystallization temperature of the barriers on a $SiO_2$ substrate, with and without the Cu overlayer, and the intermetallic compounds formed when a failure has occurred, and the possible failure mode deduced.

**4.3.2 Ti-Si films**

In the case of the amorphous $Ti_{62}Si_{38}$ (b1) barrier and a Cu overlayer, a substantial difference in the maximum temperature of stability is observed for the bare Si and the oxidized Si substrates. The former scheme fails at 450 °C, which is 200 °C lower than the latter does. This observation implies that the failure on a Si substrate is initiated by either the reaction of the barrier with the Si or the diffusion of Cu or Si through the barrier. The test with the barrier alone on a bare Si substrate indicates that they do not react at 450 °C. It is thus the transport of Cu or/and Si through the $Ti_{62}Si_{38}$ (b1) layer that initiates this failure. Although Cu penetration at 450 °C may occur in amounts too small to be detected by our techniques when the bottom layer is $SiO_2$, it may be greatly enhanced by the local Cu/Si reaction when Si lies below the barrier and a reaction is initiated locally. We recall that Cu deposited directly on Si severely reacts with it already at 300 °C [4].

The Si-rich amorphous barrier of $Ti_{34}Si_{66}$ (a1) fails at temperature as low as 250 °C, with either Si or $SiO_2$ at the bottom. The origin of this failure is unrelated to the substrate and hence likely associated with the reaction between the barrier and the Cu

overlayer, with the formation of the γ-$Cu_5Si$ phase, as indicated by the results presented in Table 4.1.

The failure of the amorphous Ti-rich $Ti_{76}Si_{24}$ (c1) barrier takes place at 500 °C no matter whether a Si or a $SiO_2$ substrate is used. No detectable alteration of the surface morphology of the sample is associated with the failure. Most likely it is the reaction of Cu with the barrier that initiates the failure. We could not identify the emerging phases from x-ray diffraction analysis.

We conclude in summary that on a Si substrate, the nitrogen-free barriers with a high content of Si or Ti fail by reaction with the Cu overlayer, while the $Ti_5Si_3$-based barrier most probably fails by crystallization of the amorphous barrier induced by Cu and its subsequent penetration to, and reaction with, the Si substrate. The Ti-rich silicide barrier $Ti_{76}Si_{24}$ (c1) maintains the integrity of the Si metallization up to 450 °C.

### 4.3.3 Ti-Si-N films

The simplified ternary phase diagrams of Cu-Si-N and Cu-Ti-N [5, 6] in the 700-1000 °C range are shown in Fig. 4.8. A key difference from those with Al (Fig. 3.6) is the existence of tie-lines between Cu and both TiN and $Si_3N_4$. We attribute the sudden rise of the maximum temperature of stability when the nitrogen concentration exceeds 40 at.% in films for all three targets to the chemical inertness of Ti-Si-N. This is evidenced by the exceptionally high maximum temperature of stability of 900 °C when the non-reactive oxide is underlying. In addition, both TiN and $Si_3N_4$ are stable in contact with Si according to the Ti-Si-N phase diagram. We consistently find by backscattering

spectrometry that the nitrogen-rich barriers are stable on Si at 900 °C (when Cu is absent). The diffusion of Cu or/and Si through the barrier layer thus becomes the only mechanism leading to the disruption of the structure.

The TiN diffusion barrier for Cu on Si has been studied in the recent past. Sputter-deposited TiN usually has a columnar grain structure, with a lateral grain size of a few tens of nanometers [7]. The system deteriorates at 700 °C or below presumably via grain boundary diffusions of Cu [8-11]. We observed a similar columnar grain structure in the film of $Ti_{35}Si_{13}N_{52}$ (c3) (section 2.3.2), which explains its disruption at a relatively low temperature of 750 °C as opposed to 900 °C for the barriers of nanocrystalline $Ti_{35}Si_{13}N_{52}$ (b3) and amorphous $Ti_{19}Si_{40}N_{41}$ (a3).

The much improved strength of barriers deposited from the $Ti_5Si_3$ and $TiSi_2$ targets with more than 40 at.% of nitrogen is most likely due to the reduced size of the TiN grains and, more importantly, to the incorporation of amorphous $SiN_x$ between grains, or a total absence of distinguishable crystalline structure. The failure of these barriers starts locally at 900 °C, as shown in the scanning electron micrographs (Fig. 4.4). We are unable to specify what features in the film had caused the local failure. The nanocrystalline barrier of $Ti_{34}Si_{23}N_{43}$ (b3) is comparable to the amorphous $Ta_{36}Si_{14}N_{50}$ [4] in terms of resistivity and barrier strength for Cu metallization.

### 4.3.4 Composition selection for an optimized diffusion barrier

With the insights gained so far on how some parameters change over the composition field of the ternary Ti-Si-N phase diagram, one can delineate where the

optimum atomic composition of a diffusion barrier between Cu and Si lies. To be effective, a diffusion barrier must, firstly, be chemically inert against the substrate and the metal overlayer. Among the equilibrium phases in the Ti-Si-N phase diagram of Fig. 2.3, Ti and Si form compounds with Cu. The experiments we conducted with $SiO_2$ substrates reveal that all three titanium silicides also are unstable with Cu and react with it at 650 °C or less (Table 4.1). Titanium and the Ti-rich silicides are not stable with Si either. On the other hand, TiN and $Si_3N_4$ are stable with both Si and Cu. These facts indicate that a stable barrier between Si and Cu needs to have TiN and/or $Si_3N_4$ as major constituents (Fig. 4.10a). Accordingly, the results indicate that for all the three Ti to Si ratios we tested, stability of the barriers improves radically when nitrogen exceeds 40 at.% (see Table 3.1).

Secondly, the barrier must be electrically conductive. Titanium nitride is a metallic conductor. Applying a bias to the substrate during sputter-deposition effectively depresses the oxygen and the void concentration in the film, and a resistivity around 50 μΩcm is usually obtainable that way. In contrast, $Si_3N_4$ is a large band-gap insulator. Films that compositionally fall in the vicinity of $Si_3N_4$ all have very high resistivities too, and films that compositionally fall near TiN all have fairly good resistivities (see section 2.5). An appropriate diffusion barrier should therefore be located compositionally away from the region near $Si_3N_4$ and close to TiN. The region of composition eliminated by this resistivity consideration is indicated in Fig. 4.10b.

Thirdly, a diffusion barrier should be free of grain boundaries or extended defects. Sputtered Ti and reactively sputtered TiN films lack this merit because of their

polycrystalline structure. We have observed by cross-sectional transmission electron microscopy that adding about 15 at.% of Si to TiN reduces its grain size to 10 nm or less, but the grains remain columnar. With 25 at.% of the Ti atoms replaced by Si, the size of the grains is further reduced to 3 nm or less and the nano-grains are buried in an amorphous matrix. For yet higher Si concentrations (~ 40 at.%), the nanograins disappear entirely and the structure becomes uniformly amorphous (see section 2.3.1). To avoid extended defects, the composition range indicated schematically in Fig. 4.10c should thus be shunned.

When the three requirements, stability (with Cu and Si), resistivity, and microstructure are considered together, the allowable composition field that remains is sketched in Fig. 4.10d. That field is near or slightly below the TiN-$Si_3N_4$ tie-line. How far towards $Si_3N_4$ the optimum lies depends on the required thickness of the barrier layer and its area.

## 4.4 Conclusion

Of the Ti-Si-N films reactively sputtered from a $Ti_5Si_3$, a $TiSi_2$ or a $Ti_3Si$ target, $Ti_{34}Si_{23}N_{43}$ (b3) is the most effective diffusion barrier between Si and Cu. The as-deposited film has an electrical resistivity of 660 μΩcm and a nanocrystalline structure.

A 100 nm film of $Ti_{34}Si_{23}N_{43}$ (b3) between shallow $n^+p$ junction diodes and Cu overlayers maintains the integrity of the diodes up to 850 °C upon 30 min vacuum annealing. The metallization fails locally at 900 °C. This ternary alloy is obviously superior to TiN films of the same thickness.

The $Ti_{34}Si_{23}N_{43}$ (b3) alloy derives its high effectiveness as a diffusion barrier from its microstructure where TiN nanocrystals are randomly immersed in an amorphous matrix of $SiN_x$. A $Ti_{35}Si_{13}N_{52}$ (c3) film is less effective than $Ti_{34}Si_{23}N_{43}$ (b3), probably owing to its columnar structure which provides fast diffusion path for Cu. An amorphous film of $Ti_{19}Si_{40}N_{41}$ (a3) is equally effective as $Ti_{34}Si_{23}N_{43}$ (b3), but its resistivity is excessive for most barrier applications in advanced semiconductor devices.

For interconnection lines and via holes that are themselves only a few multiples of 100 nm, diffusion barriers must be limited to thickness of the order of 10 nm. A reactively sputtered 10 nm-thick nanocrystalline $Ti_{34}Si_{23}N_{43}$ (b3) film has been shown to prevent the degradation of shallow junction diodes up to 650 °C for 30 min vacuum annealing [3]. This performance is above current stability requirement and demonstrates the potential usefulness of these films at sub-0.25 μm dimensions. Preliminary research further indicates that Ti-Si-N films can be synthesized by metal-organic chemical vapor deposition [12,13]. These films are superior to reactively-sputtered TiN as barrier for Cu electrodes to <Si>/$SiO_2$ capacitors, and at a gain in conformal step coverage.

## REFERENCES

1. No ASTM card avalable, diffraction lines deduced from crystal structure.

2. J.S. Reid, X. Sun, E. Kolawa, and M-A. Nicolet, IEEE Eletron. Devices Lett. **15**, 298 (1994).

3. ASTM card: 4-0841

4. E. Kolawa, J.S. Chen, J.S. Reid, P.J. Pokala, and M-A. Nicolet, J. Appl. Phys. **70**, 1369 (1991).

5. A. Brahansali, presented in S.-Q. Wang, I. Raaijmakers, B.J. Burrow, S. Suthar, S. Redkar, J. Appl. Phys. **68**, 5176 (1990).

6. F. Weitzer, K. Remschnig, J.C. Schuster, and P. Rogl, J. Mater. Res. **5**, 2152 (1990).

7. See, for example, N. Kumar, J.T. McGinn, K. Pourrezaei, B. Lee, and E.C. Douglas, J. Vac. Sci. Technol. A**6** (3), 1602 (1988).

8. N. Cheung, H. von Seefeld, and M-A. Nicolet, proceedings of the Symposium on Thin Film Interfaces and Interconnections, edited by J.E.E. Baglin and J.M. Poate (The Electrochemical Society, Inc., Princeton, New Jersey, 1980), p323.

9. J.O. Olowolafe, Jian Li, J.W. Mayer, and E.G. Colgan, Appl. Phys. Lett. **58**, 469 (1991).

10. J.S. Reid, Ph.D. thesis, California Institute of Technology, 1995 (unpublished).

11. J.O. Olowolafe, C.J. Mogab, R.B. Gregory, and M. Kottke, J. Appl. Phys., **72**, 4099 (1992).

12. P.M. Smith, J.S. Custer, A.W. Maverich, D.A. Roberts, J.A.T. Norman, A.K. Hochverg, G. Bai, J.S. Reid, and M-A. Nicolet, *Advanced Metallization and Interconnect Systems for ULSI Applications in 1995*, Mater. Res. Soc. (1996).

13. G. Bai, S. Wittenbrock, V. Ochoa, R. Villasol, C. Chiang, T. Marieb, D. Gardner, C. Mu, D. Fraser, and M. Bohr, *Mat. Res. Soc. Symp. Proc.* (1994).

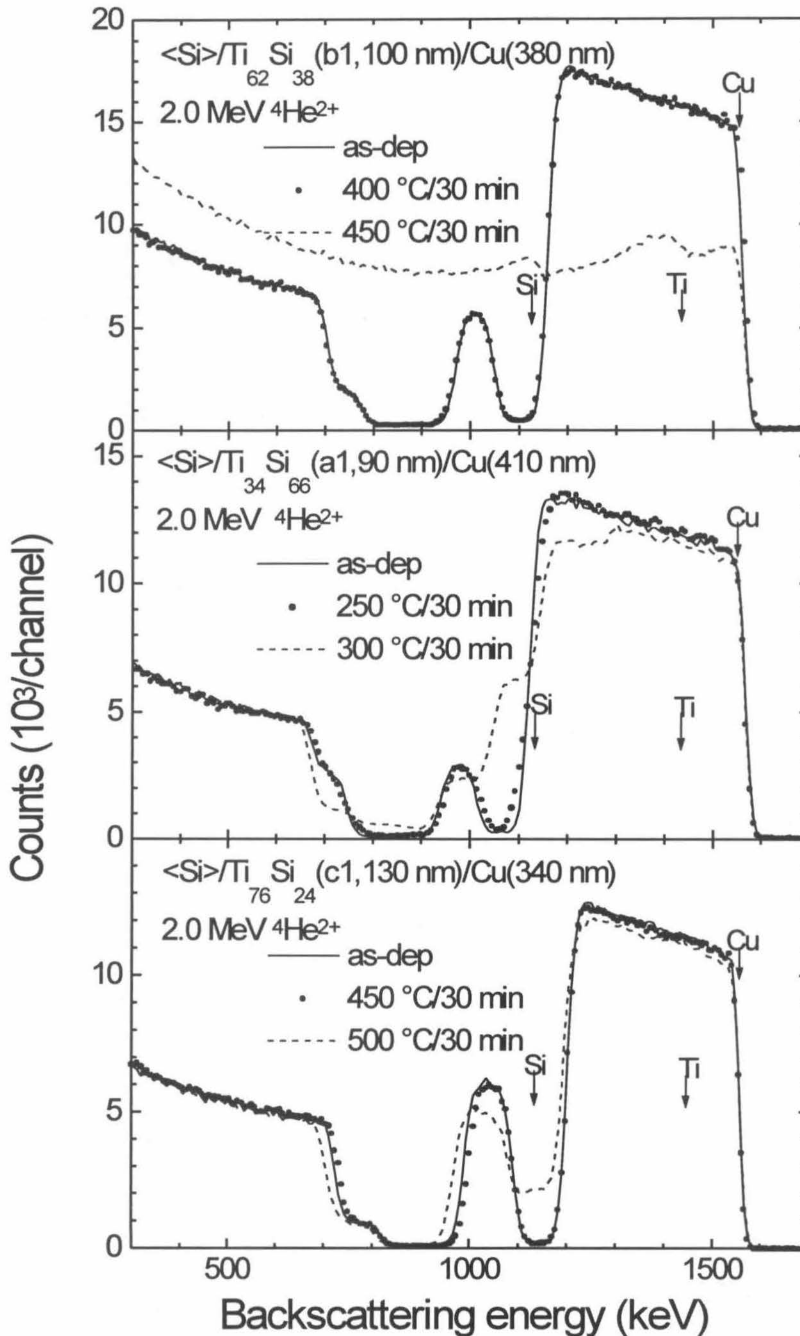


FIG. 4.1. 2.0 MeV $^4He^{2+}$ backscattering spectra of a sample <Si>/$Ti_{62}Si_{38}$(b1,100 nm)/Cu (380 nm), as-deposited and after 30 min annealing in vacuum, at 400 or 450 °C (top). *I dem* for a sample <Si>/$Ti_{34}Si_{66}$(a1,90 nm)/Cu(410 nm), as-deposited and for 250 or 300 °C (center). *I dem* for a sample <Si>/$Ti_{76}Si_{24}$(c1,130 nm)/Cu(340 nm), as-deposited and for 500 or 550 °C (bottom) (5 °-off normal beam incidence; scattering angle of detected particles is 170 °).

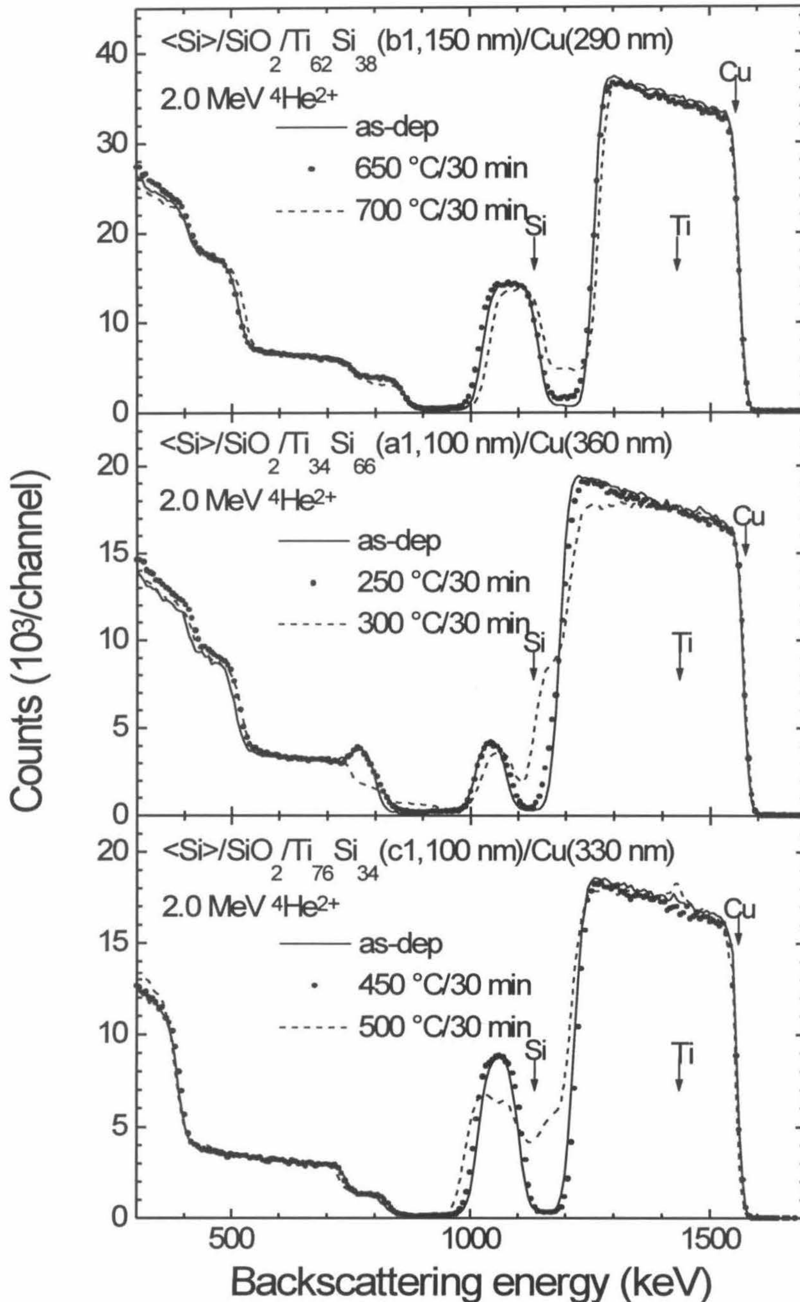


FIG. 4.2. 2.0 MeV $^{4}He^{2+}$ backscattering spectra of a sample <Si>/$SiO_2$/$Ti_{62}Si_{38}$(b1,150 nm)/Cu (290 nm), as-deposited and after 30 min annealing in vacuum, at 400 or 450 °C (top). *I dem* for a sample <Si>/$SiO_2$/$Ti_{34}Si_{66}$(a1,100 nm)/Cu(360 nm), as-deposited and for 250 or 300 °C (center). *I dem* for a sample <Si>/$SiO_2$/$Ti_{76}Si_{24}$(c1,100 nm)/Cu(320 nm), as-deposited and for 500 or 550 °C (bottom) (5 °-off normal beam incidence; scattering angle of detected particles is 170 °).

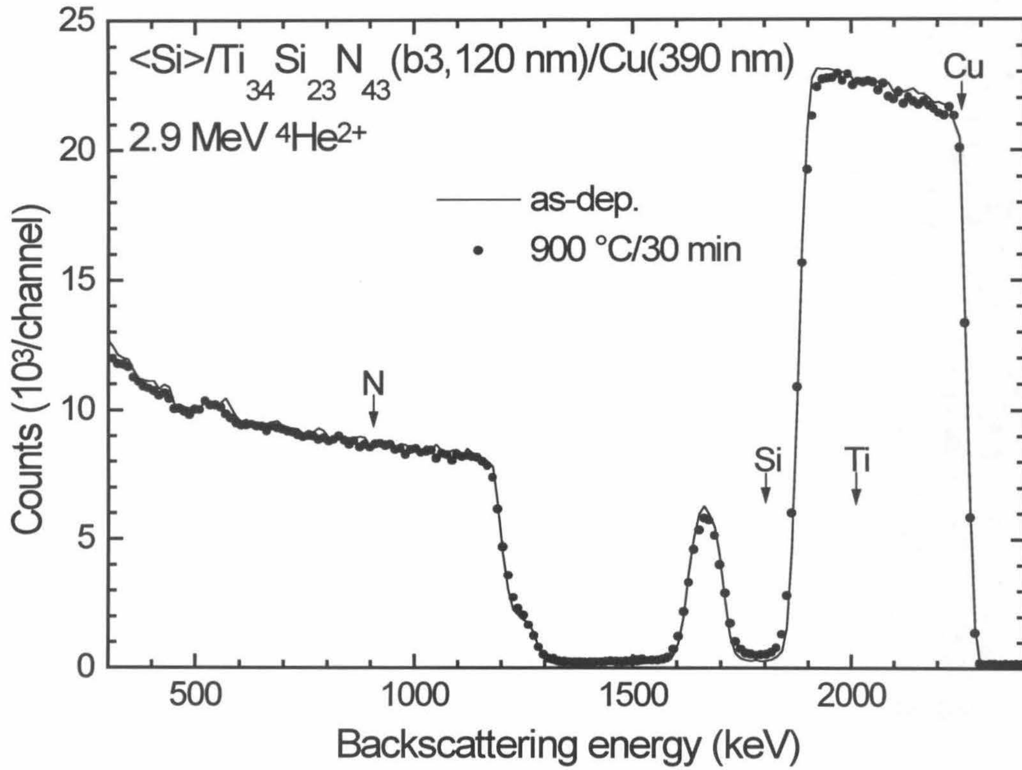


FIG. 4.3. 2.9 MeV $^4He^{2+}$ backscattering spectra of a sample <Si>/$Ti_{34}Si_{23}N_{43}$(b3,120 nm)/Cu(390 nm), as-deposited and after 30 min annealing in vacuum at 900 °C (5 °-off normal beam incidence; scattering angle of detected particles is 170 °).

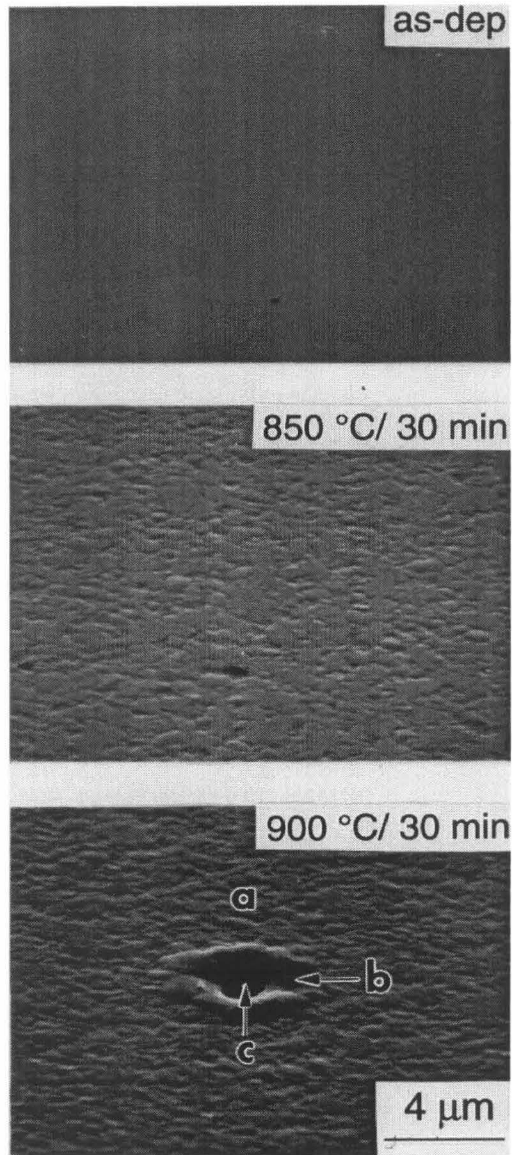


FIG. 4.4. Scanning electron micrographs of a sample <Si>/$Ti_{34}Si_{23}N_{43}$(b3,~100 nm)/Cu(~400 nm), as-deposited and after 30 min annealing at 850 or 900 °C.

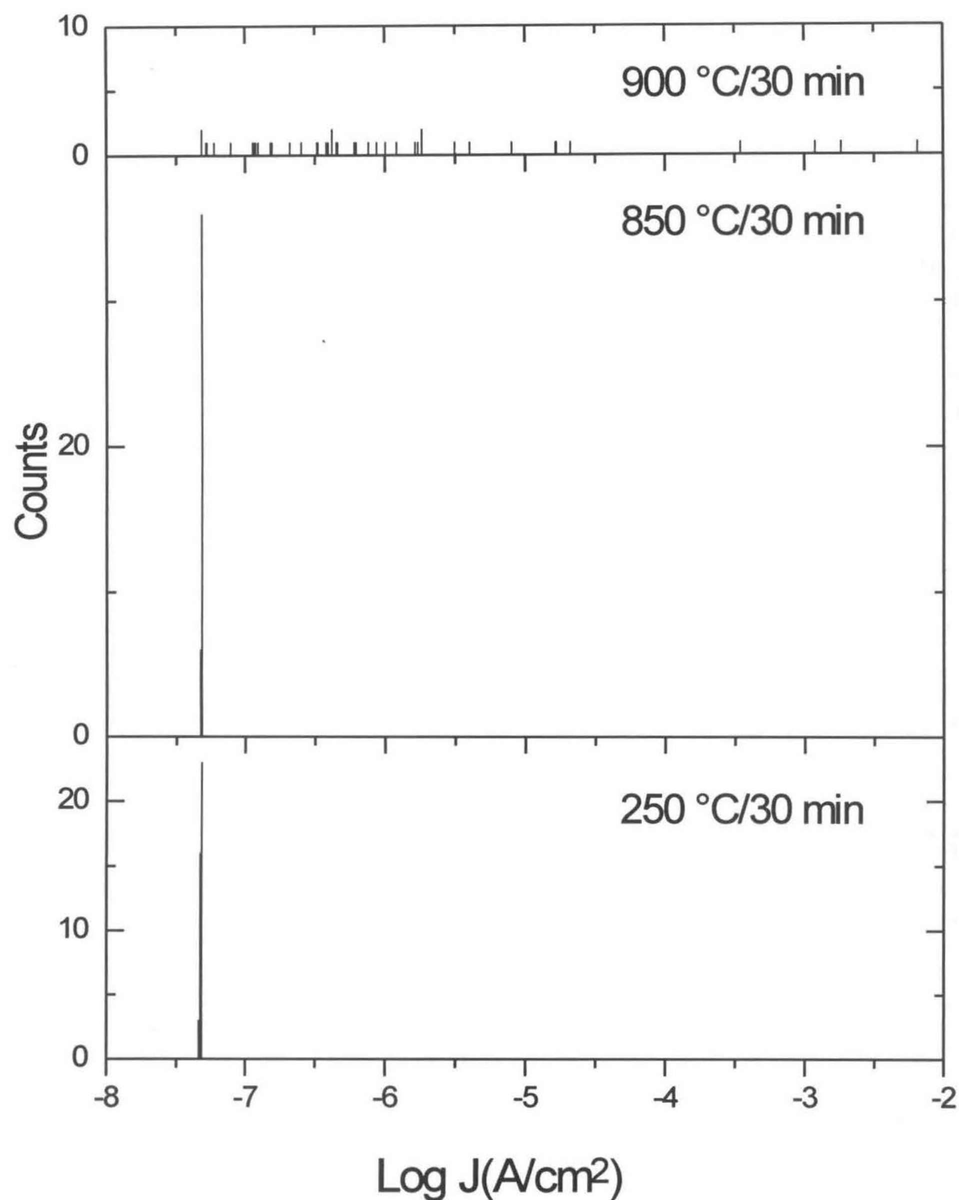


FIG. 4.5. Histograms of the measured reverse current density at -4 V bias and room temperature of 42 Si $n^+p$ shallow junctions with a ~100 nm thick amorphous $Ti_{19}Si_{40}N_{41}$ (a3) barrier layer and a ~400 nm Cu overlayer after 30 min annealing at 250, 850, and 900 °C.

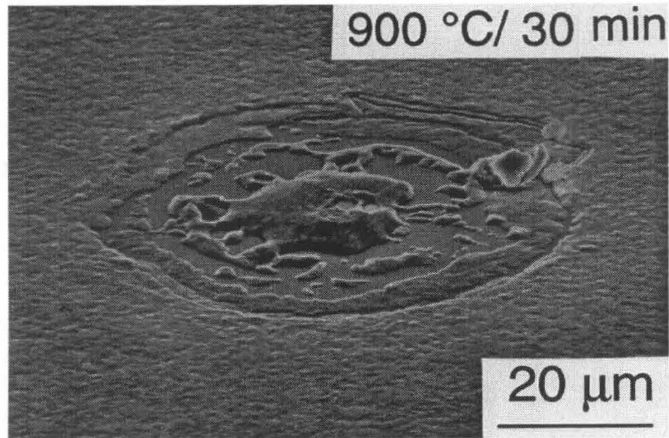


FIG. 4.6. Scanning electron micrograph of a sample <Si>/$Ti_{19}Si_{40}N_{41}$(a3,~100 nm)/Cu (~350 nm), after 30 min annealing at 900 °C.

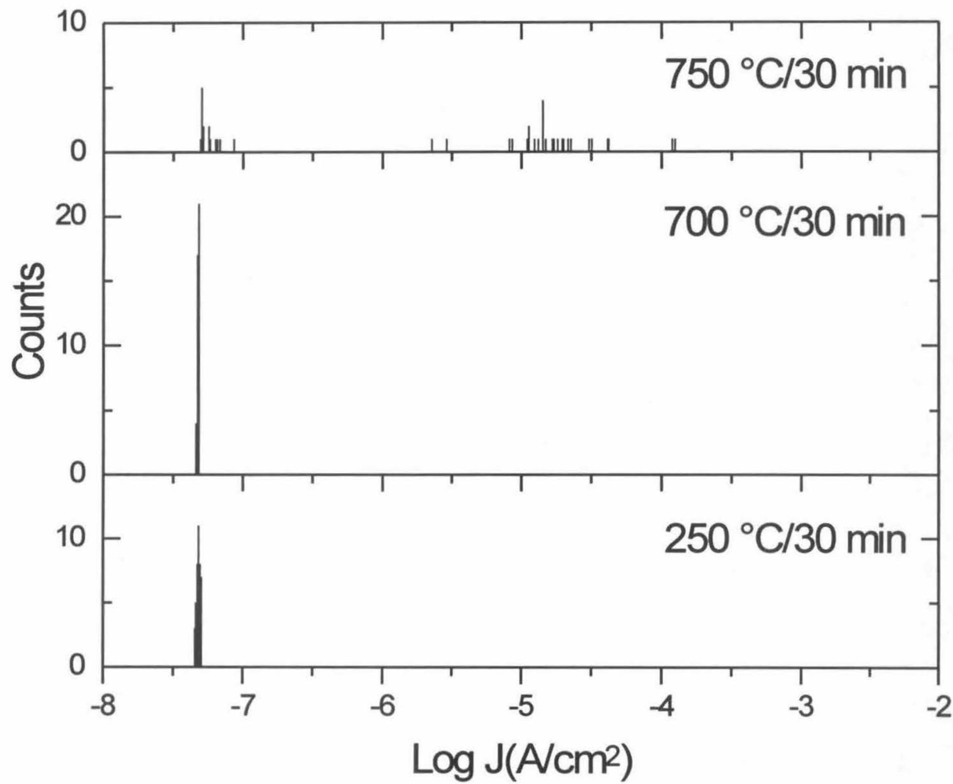


FIG. 4.7. Histograms of the measured reverse current density at -4 V bias and room temperature of 42 Si $n^+p$ shallow junctions with a ~100 nm thick columnar $Ti_{35}Si_{13}N_{52}$ (c3) barrier layer and a ~350 nm Cu overlayer after 30 min annealing at 250, 700, and 750 °C.

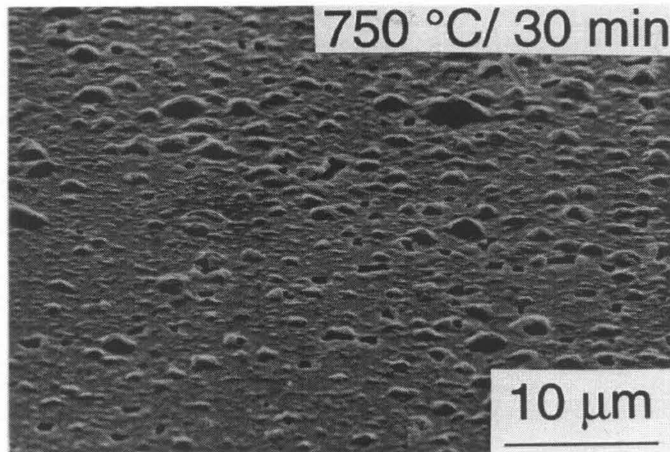


FIG. 4.8. Scanning electron micrograph of a sample <Si>/$Ti_{35}Si_{13}N_{52}$(c3,~100 nm)/Cu (~350 nm), after 30 min annealing at 750 °C.

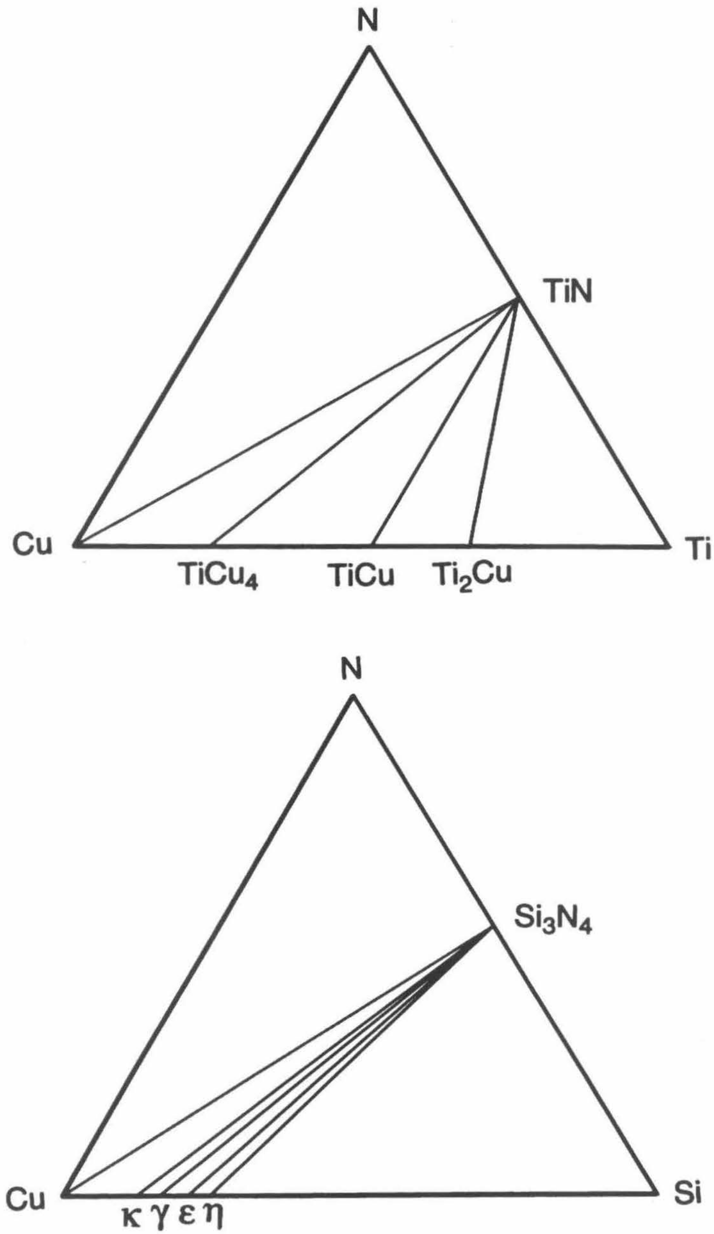


FIG. 4.9. Simplified Cu-Ti-N and Cu-Si-N phase diagrams, suggested by Bhansali et al. [5] and Weitzer et al. [6] at 700-1000 °C and 700 °C, respectively.

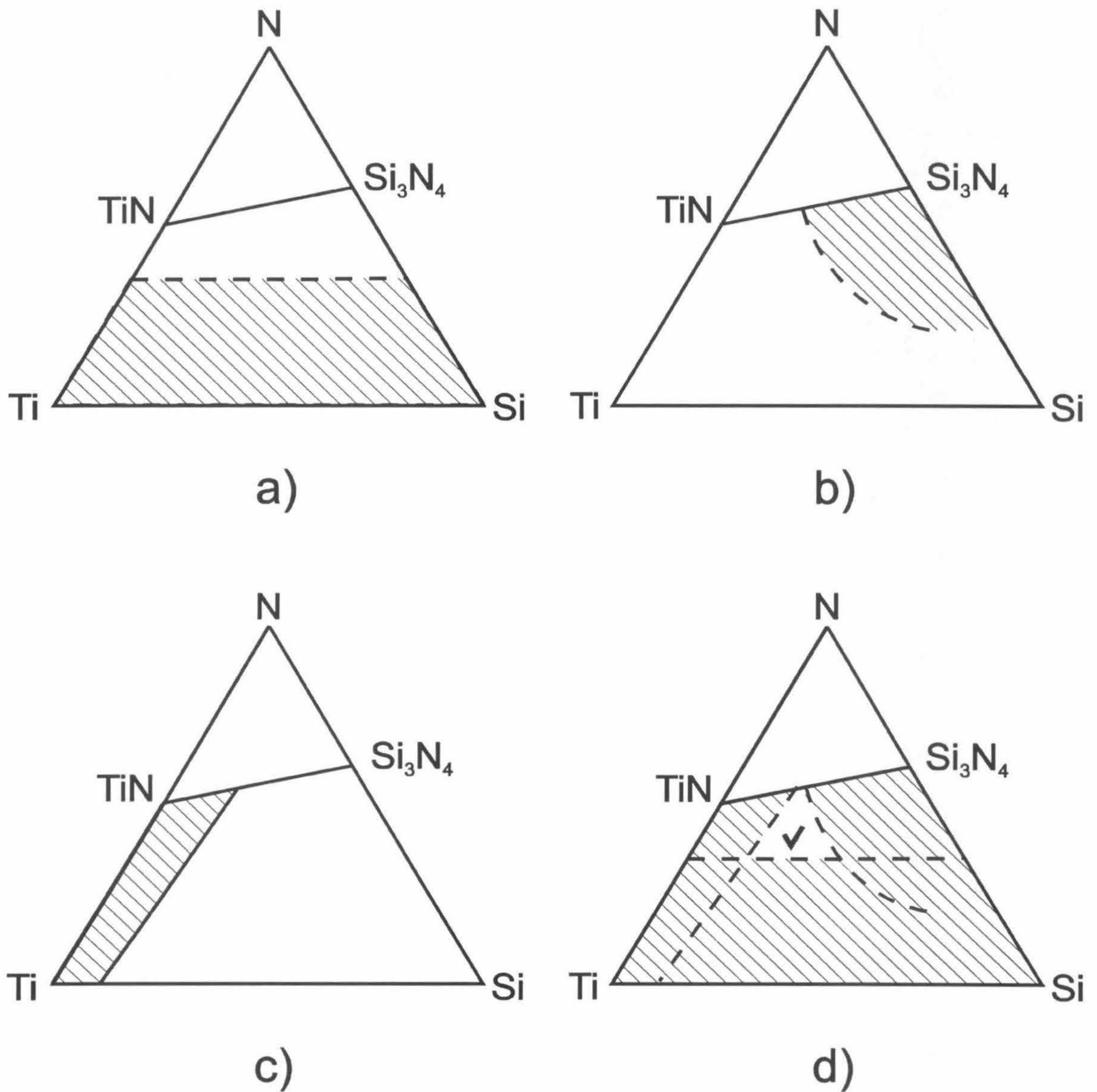


FIG. 4.10. Schematic of composition regions in a Ti-Si-N phase diagram: a) unstable region; b) high resistivity region; c) polycrystalline region; d) field marked with cross is the allowable region for a diffusion barrier.

| film | <Si>/barrier/Cu | | <Si>/$SiO_2$/barrier/Cu | | x-ray crys. temp. on $SiO_2$.(°C) | | possible failure mode (on <Si>) |
|---|---|---|---|---|---|---|---|
| | max. temp. of stability (°C) | phases formed at 50°C above | max. temp. of stability (°C) | phases formed at 50°C above | without Cu | with Cu | |
| $Ti_{62}Si_{38}$ (b1) | 400 | η″-$Cu_3Si$ | 600 | none | 700 | 500 | diffusion |
| $Ti_{34}Si_{66}$ (a1) | 200 | γ-$Cu_5Si$ | 200 | γ-$Cu_5Si$ | 500 | ≥ 200 | reaction |
| $Ti_{76}Si_{24}$ (c1) | 450 | none | 450 | none | 500 | ≥ 450 | reaction |
| $Ti_{34}Si_{23}N_{43}$ (b3) | 850 | none | 900 | - | 1000 | 900 | local |
| $Ti_{19}Si_{40}N_{41}$ (a3) | 850 | none | 900 | - | 1000 | ≥ 900 | local |
| $Ti_{35}Si_{13}N_{52}$ (c3) | 700 | none | 850 | none | * | * | diffusion |

Table 4.1. Maximum temperature of stability of ~100 nm-thick Ti-Si and Ti-Si-N diffusion barriers between Si and ~400 nm Cu, or $SiO_2$ and ~400 nm Cu, the intermetallic compounds detected by x-ray diffraction at 50 °C above the maximum temperature of stability, x-ray crystallization temperatures of the films on $SiO_2$ substrate with or without Cu overlayer, and failure mode deduced.

* as-deposited film is polycrystalline by x-ray diffraction

# II. Oxidation, Diffusion, and Crystallization of an Amorphous $Zr_{60}Al_{15}Ni_{25}$ Alloy

## 1. Introduction

Metallic glasses are metallic alloys solidified from a melt whose x-ray and electron diffraction patterns show no sharp peak. Microscopically, their atomic structure lacks long range translational symmetry [1]. Metallic glasses possess a number of interesting and potentially useful properties. It was first reported in 1959 that a metallic glass is obtainable in the form of a foil by rapid quenching at a cooling rate of ~ $10^6$ K/s [2].

The glass transition temperature of metallic glasses is usually monitored by the steep increase in the specific heat that characterizes the transition from the state of a glass to that of an undercooled liquid, and sometimes by the rapid decrease of the viscosity through $10^{12}$ $Nsm^{-2}$ ($10^{13}$ poise) [1,3], both with increasing temperature.

Two measurements are used to evaluate the glass forming ability of metallic glasses: the supercooled liquid region (or $\Delta T_x$, the temperature span between the glass transition and the crystallization temperature), and the reduced glass transition temperature (the ratio of the glass transition temperature to the melting temperature). Inoue et al. have concluded that there is a clear tendency that $T_g/T_m$ increases with $\Delta T_x$ in some La, Mg, and Zr-based alloys [4]. It has also been shown that the critical cooling rate for the glass formation, $R_c$, decreases with increasing $T_g/T_m$ and $\Delta T_x$ [4].

Being amorphous, metallic glasses possess a number of attractive properties like high corrosion resistance, high mechanical strength and good ductility, and low temperature dependence of resistivity. Some Fe, Co, and Ni-based alloys are soft magnetic material with Curie temperatures well above room temperature. Moreover, a good combination of these properties makes them unique materials in certain applications. For example, their mechanical property together with the high corrosion resistance make them suitable for protective coatings for machine parts and chemical plants. The high permeability of some Co-based metallic glasses, combined with their high wear-resistance, are exploited for recording heads. It is obvious that their application will greatly widen if metallic glasses can be obtained in a bulk form.

Recently, great progress has been made through the active search for practically processable bulk metallic glasses. The group of Inoue and Masumoto has introduced families of La [5,6], Mg [7,8] and Zr [9-11]-based alloys, with excellent glass-forming ability and high thermal stability. They can be formed by casting at a cooling rate of $10^3$ K/s or less. Two alloys, namely, ZrTiNiCuBe [12,13] and TiZrCuNi [14], have been developed by Prof. Johnson's group at Caltech, which have the highest glass-forming ability ever reported. They possess a reduced glass transition temperature of 0.67 and 0.58 respectively, and can be processed by copper-mold casting at a dimension of millimeters to centimeters.

Among these alloys, there are a few Zr-based alloy groups, like ZrAlNi [9], ZrAlCu [10], ZrAlNiCu [11] and ZrTiNiCuBe [12]. It is well-known that Zr is highly reactive with oxygen. It is therefore of general interest and also of practical relevance to

study the mechanism of oxidation and its possible effects on nucleation of crystalline phases near the glass transition temperature. Such studies are also relevant to atomic diffusion, and to assessing the relationship between viscosity and diffusivity in the supercooled liquid [1,3]. The present study examines the temperature-dependent behavior of the amorphous $Zr_{60}Al_{15}Ni_{25}$ alloy in an oxygen atmosphere.

The $Zr_{60}Al_{15}Ni_{25}$ alloy has a glass transition temperature of 710 K (437 °C), a crystallization temperature of 787 K (514 °C), and a reduced glass transition temperature of 0.64. This alloy has been chosen for this investigation because the three elements are well separated in atomic number, so that their signals in a backscattering spectrum are clearly distinguishable. Secondly, the particular atomic composition selected has the highest supercooled liquid region (77 K) among all amorphous Zr-Al-Ni alloys [4]. Also, the $Zr_{60}Al_{15}Ni_{25}$ alloy contains mainly transition metals and no noble metals, lanthanide, or beryllium. This metallic glass has a greater tensile strength and a higher glass transition and crystallization temperatures than those of the Mg- and La- based alloys [15]. This alloy is a practically promising material and is also a convenient vehicle on which to study the oxidation of a metallic glass.

## 2. Experimental procedures

$Zr_{60}Al_{15}Ni_{25}$ ingots were prepared by induction melting on a water-cooled copper boat under a Ti-gettered argon atmosphere. Small pieces of the initial ingot were levitation-melted in an rf field. The samples were subsequently quenched into thin foils

in a pure argon-filled twin-piston rapid quencher. The thickness of these foils is about 50 μm.

The foils were exposed to dry oxygen in an open-ended quartz-tube furnace over a temperature range of 310 °C to 450 °C. The oxygen gas flow was adjusted to 100 $cm^3$/min. A few other samples were annealed in a vacuum furnace at a pressure of less than $1\times 10^{-6}$ Torr.

Backscattering spectrometry using 2.0 MeV and 6.2 MeV $^4He^{2+}$ ions was performed to analyze the depth profiles of the elements. To study the structure of the as-quenched and annealed foils, 12°-glancing-angle x-ray diffraction using Co $K_\alpha$ radiation ($\lambda$=0.179 nm) was applied. The microstructure and composition of the samples were also studied by transition electron microscopy and analyzed by energy-dispersive x-ray analysis. The transition electron microscopy specimens were prepared by a microtome technique.

## 3. Oxidation between 310 and 390 °C

### 3.1 Oxide composition and growth law at 370 °C, with kinetic modeling

Figure 1 shows the backscattering spectra of $Zr_{60}Al_{15}Ni_{25}$ foils, as-quenched, and annealed at 370 °C for various duration. The signal of the light element Al is barely resolved over the background of the Zr and the Ni yields. Spectra of the annealed samples reveal that the Zr is oxidized, as the reduced height of its signal proves. In addition, an oxygen plateau appears at the low-energy part. The constant height of the Zr and the O signals after oxidation suggests a uniform composition *of the oxide.* The Ni

edge moves to lower energies, indicating that Ni is expelled from the growing oxide layer. The Ni yield also rises above its prior height just to the left of its edge (below 1500 keV). This excess signal broadens with annealing duration, but its maximum height stays constant, which implies that the Ni concentration near the interface increases to a fixed value, independent of oxidation duration. Whether the Al is oxidized or not cannot be directly discerned, but can be inferred from the height of the Zr surface signal. Taking the height of this signal before oxidation, $H_{Zr}^{alloy}$, as reference, the heights $H_{Zr}^{ZrO_2}$ and $H_{Zr}^{ZrO_2+Al_2O_3}$ that correspond to the oxide of pure $ZrO_2$, or of both $ZrO_2$ and $Al_2O_3$ can be derived. Their values are marked on the right axis in Fig. 1. The signal height of $H_{Zr}^{ZrO_2+Al_2O_3}$ matches the experimental Zr signal, which suggests that the surface oxide layer consists of a mixed oxide of $ZrO_2$ and $Al_2O_3$ containing roughly the same Zr to Al cation ratio as the original glassy alloy. The thickness of the oxides was calculated from the energy shift of the Ni high-energy edge. The square of the oxide thickness is found to be proportional to the annealing duration. The details are presented in the section 3.2.

The yield of the Ni signal just to the left of its high-energy edge in the backscattering spectra is constant for all annealing durations considered. Correspondingly, the steady-state Ni concentration within the alloy near the interface is about 35 at.%. This observation suggests that Ni reaches a chemical equilibrium at the alloy/oxide interface.

Since both the Zr and Al are uniformly distributed throughout the oxide, it is possible that oxygen is the dominant moving species in this reaction, and that the oxidation takes place at the oxide/alloy interface. The other less likely case is that Zr and

Al migrate through the oxide at certain rates, that will maintain an unchanged Zr to Al atomic ratio upon their oxidation at the surface. Most likely, the scenario for the oxidation process at 370 °C is the following: oxygen transports through the oxide layer to the interface, where it reacts with Zr and Al, while Ni diffuses back into the amorphous alloy. The experimentally observed parabolic growth of the oxide layer (section 2.3) indicates that the oxidation is not controlled by interfacial reaction but is transport-limited. According to the above interpretation of the backscattering spectrometry results, two diffusion processes are involved: the diffusion of oxygen in the oxide, and that of nickel in the alloy. The progression of the oxidation is then controlled by the slower of these two processes.

First, we model the system one-dimensionally at interfacial chemical equilibrium when it is the Ni diffusion into the alloy that limits the growth rate. We assume that the Ni concentration is zero in the oxide, is $C_1$ at the interface, and is $C_0$ far away from the interface, where $C_0$ is the initial concentration of Ni in the alloy. Both C's are independent of time with $C_1$ larger than $C_0$. Let the coordinate x' that moves with the interface be zero at the interface and positive below. Under these conditions, the Ni concentration C(x', t) is a complementary error function

$$C(x',t) = C_0 + (C_1 - C_0)\mathrm{erfc}\left(\frac{x'}{\sqrt{4D_{Ni}^{alloy}t}}\right), \qquad (1)$$

where t is the annealing duration, and $D_{Ni}^{alloy}$ is the Ni diffusivity in the alloy. The position of the interface, x(t), which also represents the thickness of the oxide layer, is

measured in a stationary coordinate system with the sample surface at the origin. After a short time interval dt, the amount of Ni rejected from the alloy layer is $\gamma C_0 dx$, where $\gamma$ is the conversion factor from the oxide thickness to the thickness of the consumed alloy, and is equal to the ratio of Zr or Al atomic density in the oxide to that in the alloy. This amount must equal the total increase of the Ni below the interface, i.e.,

$$\gamma\, C_0 dx = dt \int_0^{\infty} \frac{\partial}{\partial t} C(x', t) dx' \qquad (2)$$

Substituting C(x', t) into the above equation and integrate, we obtain for the speed of the Ni front

$$\frac{dx}{dt} = \frac{1}{2} \frac{C_1 - C_0}{\gamma\, C_0} \sqrt{\frac{D_{Ni}^{alloy}}{t}}\,, \qquad (3)$$

or

$$x^2 = 2K_{Ni}^{alloy} t \qquad (4)$$

The transport constant

$$K_{Ni}^{alloy} \equiv \frac{1}{2} \left(\frac{C_1 - C_0}{\gamma\, C_0}\right)^2 D_{Ni}^{alloy} \qquad (5)$$

is proportional to the Ni diffusivity in the alloy.

Secondly, we consider the case in which the diffusion of oxygen limits the growth rate. We model the process by assuming a fixed oxygen concentration in the oxide at the

surface ($C_1'$) and at the interface ($C_0'$). The oxygen arrives at the oxide alloy interface with a flux of

$$j = D_O^{Oxide} \frac{(C_1' - C_0')}{x}, \quad (6)$$

assuming a quasi-steady-state condition for the growth, i.e., linear oxygen concentration distribution in the oxide layer. The oxidation reaction with the Zr and Al consumes a number of oxygen atoms in the amount of jdt per unit area during the time increment dt. Correspondingly, the gain of oxygen atoms in the oxide (per unit area) equals Ndx, where N is the elemental atomic density of oxygen in the oxide layer. For mass conservation,

$$j = N \frac{dx}{dt}. \quad (7)$$

Combining eq. (6) and (7), the progression of the oxidation front follows a parabolic rate equation [16,17],

$$x^2 = 2K_O^{Oxide} t, \quad (8)$$

where the transport constant $K_O^{Oxide}$ is related to the oxygen diffusivity $D_O^{Oxide}$ by

$$K_O^{Oxide} \equiv \frac{C_1' - C_0'}{N} D_O^{Oxide}. \quad (9)$$

Equation (4) and (8) predict the same growth kinetics for a process limited by the diffusion of either nickel into the alloy or oxygen through the oxide. However, the

experimentally observed Ni-enrichment at the interface indicates that the Ni diffusion is the slower process. The following considerations give further support for this interpretation.

The Ni diffusion in amorphous $Zr_{50}Ni_{50}$ has been studied by Hoshino et al., who found a diffusivity of $7.1 \times 10^{-19}$ m$^2$/s at 370 °C [18]. For an order-of-magnitude estimate of the transport constants $K_{Ni}^{alloy}$, we adopt this diffusivity value, a Ni concentration of 25 at. % inside the alloy ($C_0$), and one of 35 at.% at the interface ($C_1$). Setting $\gamma = 1$, the ratio

$$\frac{K_{Ni}^{alloy}}{D_{Ni}^{alloy}} = \frac{1}{2}\left(\frac{C_1 - C_0}{\gamma\, C_0}\right)^2 \qquad (10)$$

is 0.08. Neglecting the change in the Zr atomic density with depth into the alloy, $K_{Ni}^{alloy}$ is about $6 \times 10^{-20}$ m$^2$/s.

Paljevic et al. have studied the oxidation kinetics of the polycrystalline phase $Zr_3Al$ under conditions similar to this experiment (atmosphere pressure, dry oxygen flow) [19]. A transport constant of $4.7 \times 10^{-18}$ m$^2$/s for oxygen in the polycrystalline oxide is extrapolated for 370 °C from their Arrhenius plot obtained with data from 440 to 530 °C. We take this number for an order-of-magnitude approximation of the transport constant $K_O^{oxide}$.

By these estimates, $K_{Ni}^{alloy}$ is about two orders of magnitude smaller than $K_O^{oxide}$. Combining such evaluation with the experimental observation of a steady-state Ni enrichment at the interface, we propose that the oxidation process is controlled by the Ni back diffusion.

**3.2 Activation energy of growth process from 310 to 390 °C**

Backscattering spectra (not shown) of the samples oxidized between 310 °C and 390 °C depict similar depth profiles as described above for 370 °C. X-ray diffractometry and transmission electron microscopy studies have shown that the oxide layer and the alloy in all samples remain amorphous.

Figure 2 shows, for several temperatures, a linear relation between the square of the oxide thickness and the annealing duration. Only two points are included at 410 °C , as the oxide remains amorphous only for 1 hour or less at that temperature (see section 4). Least-squares fits are also presented. To convert the shift of the Ni edge in the backscattering spectra to the oxide thickness, the atomic density of amorphous Zr-Al-O is required. This density is calculated approximately from a linear combination of the densities of amorphous $ZrO_2$ and crystalline $Al_2O_3$ according to the 4:1 Zr to Al cation ratio. The molecular density of the amorphous $ZrO_2$ was taken as $2.18\times10^{22}$ cm$^{-3}$ [20]. For $Al_2O_3$, we used the molecular density of $2.34\times10^{22}$ cm$^{-3}$ of the $\alpha$-$Al_2O_3$ phase [21]. The resulting atomic density for the amorphous Zr-Al-O phase is $6.90\times10^{22}$ cm$^{-3}$. The transport constants were derived from the slope of the least-square fits.

The logarithms of these constants as a function of the reciprocal temperature are shown in Fig. 3. The data can be fitted by a straight line

$$\ln\frac{K}{K_0} = -\frac{E_a}{kT}, \qquad (9)$$

where the value of $K_0$ is $(2.8\pm0.3)\times10^{-5}$ m$^2$/s, and the activation energy $E_a$ equals 1.7±0.05 eV/atom (164 kJ/mol).

The Arrhenius plots for the transport constants $K_{O}^{Zr\text{-}Al\text{-}O}$ and $K_{Ni}^{Zr\text{-}Ni}$ estimated from ref. 18 and 19 are also shown in Fig. 3. The activation energy of 1.7 eV/atom obtained here is higher than, but close to, the activation energy of $K_{Ni}^{Zr\text{-}Ni}$ (1.45 eV/atom), while it is substantially higher than that of $K_{O}^{Zr\text{-}Al\text{-}O}$ (1.18 eV/atom) [18]. This observation further supports, albeit indirectly, the conclusion that the growth of the amorphous zirconium-aluminum-oxide is very likely limited by the Ni diffusion into the alloy.

**4. Oxidation at 410 °C and above**

**4.1 Oxidation at 410 °C**

The backscattering spectra of samples oxidized at 410 °C for various durations (Fig. 4) are similar to those of Fig. 1 for oxidation at 370 °C and reveal the same layered structure.

X-ray diffraction spectra of an as-quenched foil and of one annealed for 1 hour at 410 °C depict only a broad signal characteristic of an amorphous phase (Fig. 5). The transmission electron micrograph (Fig. 6a) shows that an oxide layer (lightly contrasted region) has formed after one hour of annealing. The non-planar interface between the oxide and the alloy (indicated by dashed line) is an artifact of the sample preparation. Both the layer and the substrate are fully amorphous. The horizontal scratches (direction of microtoming) and the band-shaped vertical structure in the cross-sectional micrographs are marks left by the diamond knife and are typical for microtomed samples [22].

The depth distribution of the metal elements in the oxide and beyond was obtained by energy dispersive x-ray analysis from a cross-sectional specimen of a foil annealed for one hour at 410 °C (Fig. 7). The diagram shows the relative intensities of the $NiK_{\alpha}$, $ZrK_{\alpha}$ and $AlK_{\alpha}$ signals as a function of depth. The interface, defined as the point at half-maximum Ni concentration, is indicated in the diagram. The measured intensities do not change beyond 200 nm from the surface where the corresponding concentration is $Zr_{60}Al_{15}Ni_{25}$. It is not possible to derive the atomic compositions of the elements in the oxide from these data because oxygen cannot be detected by energy dispersive x-ray analysis in our setup using a Be window. In agreement with backscattering spectrometry, the Ni content within the experimental resolution is zero in the surface layer, and increases rapidly near the interface, reaching a maximum near 130 nm in depth. The transition region has a thickness of about 60 nm. The thickness of the surface oxide layer is about 110 nm. The discrepancy with the value measured by backscattering spectrometry (160 nm) may be caused by a lateral non-uniformity of the oxide layer, and/or the error in the estimated density used to derive the thickness from the backscattering spectrum.

The x-ray spectrum of a foil oxidized for two hours reveals Bragg peaks (Fig. 4) of a cubic $ZrO_2$ phase and an intermetallic compound $Zr_6NiAl_2$ [23]. An estimate based on the Debye-Scherrer formula indicates that the average grain size of the $ZrO_2$ particles is only a few nanometers.

The transmission electron micrographs of this sample (Figs. 6b and 6c) reveal many nanocrystals embedded in the amorphous oxide layer near the interface (arrow c).

These nanocrystals were too small for unambiguous energy-dispersive x-ray analysis or electron diffraction analysis, but they probably correspond to the $ZrO_2$ phase discerned in the x-ray spectrum. A cluster of grains is also observed across the interface in the middle of the micrograph B (arrow a). Energy dispersive x-ray analysis reveals that this cluster contains a crystalline Ni-rich ZrNiAl phase, which is not detected by x-ray diffraction because of its small volume fraction. Crystalline particles of the $Zr_6NiAl_2$ phase (arrow b) are embedded in the matrix of the amorphous alloy.

### 4.2 Oxidation at 430 °C

X-ray diffraction results indicate that the alloy crystallizes at 430 °C after 1 hour of heat treatment in oxygen (Fig. 8). The diffraction spectrum reveals the presence of the phases $ZrO_2$ and $Zr_6NiAl_2$, which are already seen at 410 °C. After 4.5 hours, three additional peaks develop, which possibly result from the diffraction of $Zr_5Ni_4Al$. Backscattering spectrometry yields spectra similar to those observed at lower temperatures.

### 4.3 Oxidation at 450 °C

Oxidation experiments were also performed at 450 °C. The backscattering spectra of these samples contain no distinctive features that are readily interpreted. It is very likely that at this temperature the oxide and the alloy are both polycrystalline and the oxidation proceeds rapidly and non-uniformly.

## 5. Oxidation at 290 °C and below

Oxides formed at 290 °C or below can be resolved by backscattering spectrometry only if the oxidation proceeds for days or even longer.

We carried out such oxidation experiment with a hot stage in air. The power applied was set manually by a commercial dimmer. The temperature was monitored and the dimmer was adjusted from time to time to avoid significant deviations from the desired temperature. The fluctuation is about 5 to 10 °C in both directions. Oxidation has been carried out for 41 days at temperatures ranging from 200 to 295 °C. The elemental depth profiles derived from the backscattering spectra show that Ni is still absent in the oxide (Fig. 9).

The thickness of the oxides was derived from the spectra, as described in section 3.2. The corresponding transport constants derived for 255, 275, and 295 °C are shown on the Arrhenius plot from 310 to 410 °C (Fig. 10). The point at 200 °C is omitted because of the large experimental error in the thickness determination. The constants attained in this manner are consistent with the Arrhenius plot derived from the data at 310 °C and above. We thus conclude that the oxidation mechanism remains the same down to 255 °C.

## 6. Remarks on preferential oxidation

The oxidation of alloys is usually more complicated than that of pure metals. Birchenall, in a review paper [24], discussed the case when the alloy contains a relatively active element and a more noble one. In such a case, according to Birchenall, preferential

oxidation of the active element may take place and the back-diffusion of the noble element may become rate-controlling, provided that its rate is lower than that of the oxidant in the oxide, and also that the alloy does not dissolve an appreciable amount of oxygen.

The oxidation process of the polycrystalline $Ge_xSi_{1-x}$ system has recently been described in details [25]. In this binary system, silicon dioxide is thermodynamically more stable than $GeO_2$ [26]. However, at low temperature, the motion of Ge and Si is frozen and the oxidant reacts with both Ge and Si as it reaches the interface by diffusion. As the temperature increases, the oxidation transitions gradually from a uniform to a preferential one. At the transition temperature (~ 700 °C), the Ge-Si-O formed has a higher Si to Ge ratio than the alloy. When the transition is complete, Ge is fully rejected from the oxide and accumulates behind the oxide.

In the amorphous alloy $Zr_{60}Al_{15}Ni_{25}$, Zr is the most reactive and Ni, the most noble element in terms of oxidation, based on a comparison of the free energy of formation per mole atoms for the corresponding stable oxides ($ZrO_2$, $Al_2O_3$, and NiO) at low temperatures [26]. Nickel is also expected to be the most mobile among the three elements due to its small atomic size compared to Zr and Al. We consistently observed the diffusion of Ni into the alloy at temperatures between 310 °C and 410 °C. According to the discussion in section 3, the diffusivity of Ni in the alloy is lower than that of the oxygen in the oxide. Thus the transport of Ni can limit the oxidation rate of the alloy $Zr_{60}Al_{15}Ni_{25}$.

A preferential oxidation of Zr over Al is not observed at temperatures below 410 °C. In this temperature range, the Al and Zr atoms are kinetically frozen and the chemical equilibrium of the oxide with the metal phases is suppressed. As temperature rises, the diffusivities increase. It is expected that Al, the second smallest element, will eventually be rejected from the oxide. This may be the situation starting to develop at 410 °C after two hours, where the nucleation and growth of $ZrO_2$ particles is observed. Another possibility is that the $ZrO_2$ particles precipitate out of the zirconium-aluminum oxide. Such a process is unrelated to the progression of the oxidation front. We consider this situation to be unlikely because the $ZrO_2$ particles are only located within a layer adjacent to the interface, and not throughout the oxide. Isolated particles of a preferential oxide have also been observed in oxidized Fe-Ni alloys [27].

Being a ternary system, the $Zr_{60}Al_{15}Ni_{25}$ alloy conceptually can have two transition temperatures. The first one could be below 200 °C, where all three elements are oxidized simultaneously below this temperature. Above the first transition temperature, Ni becomes mobile and is gradually excluded. This is described in section 3. The second transition takes place at 410 °C, when Al begins to migrate out from the oxide during oxidation.

At the same time when the $ZrO_2$ nanocrystals form, the entire amorphous alloy starts to nucleate. To examine the relationship between the nucleation of the crystalline intermetallic alloy and the formation of the $ZrO_2$ nanophase, an unoxidized foil was annealed in vacuum at 410 °C for two hours. Transmission electron micrograph of this foil (not shown) reveals grains embedded in the amorphous matrix of the alloy, like in a

sample annealed in oxygen ambient. The sizes of the grains are about the same as those observed in the oxidized samples. The positions of the peaks in the x-ray diffraction spectra of these two foils are exactly the same except for the presence or absence of two $ZrO_2$ peaks. We thus reach the conclusion that the $Zr_6NiAl_2$ grains are formed inside the alloy of samples annealed in both vacuum and oxygen atmosphere and that the crystallization of the amorphous $Zr_{60}Al_{15}Ni_{25}$ alloy at 410 °C is independent of the oxidation.

**7. Oxidation of $Zr_{72.5}Al_{15}Ni_{12.5}$ at 330 °C**

As developed so far the oxidation process of $Zr_{60}Al_{15}Ni_{25}$ can be described by a simple model. In this final section, we show that a relatively minor change in alloy composition complicates the results significantly. We have oxidized an alloy with a lesser concentration of Ni of 12.5 at. %. The sample still preserves an amorphous structure after quenching and subsequent oxidation at 330 °C. Figure 11 shows two backscattering spectra of amorphous $Zr_{60}Al_{15}Ni_{25}$ and amorphous $Zr_{72.5}Al_{15}Ni_{12.5}$ both oxidized at 330 °C for 2 hours together with that of the as-quenched foil of $Zr_{72.5}Al_{15}Ni_{12.5}$. The energy of the $^4He^{2+}$ beam was set at 6.2 MeV to take advantage of the enhanced scattering cross section of oxygen in the 6.0 to 6.2 MeV range [28]. The resonance oxygen signal indicates that the surface oxide layers have about the same thickness, but additionally, oxygen is detected below the interface in the Ni-lean sample. From the spectrum, we estimate that the oxygen content in this sample drops

monotonically below the oxide layer from 20 to 25 at. % at the interface to 0 at. % some 70 nm inside the alloy.

This result implies an elevated content of oxygen in the Ni-lean alloy. It is quite conceivable that the oxygen just below the interface exists as a solid solution in the amorphous alloy. On the other hand, the diffusion rate of Ni in the alloy is almost independent on the composition of the alloy, since the oxides have about the same thickness for both alloys.

## 8. Conclusion

Preferential oxidation is observed at the surface of amorphous $Zr_{60}Al_{15}Ni_{25}$ alloy foils. Zr and Al are uniformly oxidized at temperatures ranging from 200 °C to 390 °C with the Zr/Al ratio in the oxide similar to that in the alloy. The alloy and the oxide remain fully amorphous. We suggest that the growth of the oxide is controlled by the Ni back-diffusion in the alloy. At 410 °C, the intermetallic compound $Zr_6NiAl_2$ nucleates homogeneously in the alloy and a Ni rich ZrNiAl phase nucleates near the alloy/oxide interface. At the same time, $ZrO_2$ forms in the oxide layer near the interface.

This study supports literature reports that in some alloys which contain a relatively reactive element and a relatively noble one, a transition temperature exists from uniform to the preferential oxidation. The oxidation is homogeneous below this temperature. As temperature rises, the mobility of the noble specie increases, and this element is excluded from the alloy at the interface. The growth of the oxide layer could be controlled by the diffusion of the rejected noble element in the alloy.

The onset of crystallization for the amorphous alloy takes place at 410 °C. This crystallization is independent of the oxidation progression.

**REFERENCES**

1. F. Spaepen, in *Physics of Defect*, editted by R. Balin et al., North-Holland, Amsterdam, (1981).

2. W. Klement, Jr., R.H. Willens, P. Duwez, Nature, **187**, 869 (1960).

3. P. Chaudharid, F. Spaepen, and P.J. Steingardt, in *Glassy Metalls II*, editted by H. Beck, and J.-J. Güntherodt, Springer-Verlag, New York (1983) p127.

4. A. Inoue, T. Zhang, and T. Masumoto, Mater. Trans. J. Non-Cryst. Solids, **156**, 473 (1993).

5. A. Inoue, T. Zhang and T. Masumoto, Mater. Trans. JIM **30**, 965 (1989).

6. A. Inoue, H. Yamaguchi, T. Zhang, and T. Masumoto, Mater. Trans. JIM **31**, 104 (1990).

7. A. Inoue, K. Ohtera, K. Kita, and T. Masumoto, Jpn. J. Appl. Phys. **27**, L2248 (1988).

8. S.G. Kim, A. Inoue, and T. Masumoto, Mater. Trans. JIM **31**, 929 (1990).

9. A. Inoue, T. Zhang, and T. Masumoto, Mater. Trans. JIM **31**, 177 (1990).

10. A. Inoue, T. Zhang, and T. Masumoto, Mater. Sci. Eng. **A178**, 255 (1994).

11. T. Zhang, A. Inoue and T. Masumoto, Mater. Trans. JIM **32**, 1005 (1991).

12. A. Peker, and W.L. Johnson, Appl. Phys. Lett. **63**, 2342 (1993).

13. A. Peker, and W.L. Johnson, Mater. Sci. Eng. **A179**, 173 (1994).

14. X.H. Lin, and W.L. Johnson, J. Appl. Phys. **78**, 6514 (1995).

15. Y. Wasedam, in *Novel Application of Anomalous X-ray Scattering for Structural Characterization of Disordered Materials*, Springer-Verlag, Heidelberg (1984), p75.

16. P. Kofstad, *Nonstoichiometry, Diffusion, and Electrical Conductivity in Binary Metal Oxide* (Wiley-Interscience, New York, 1972), Chap. 8.

17. K. Hauffe, *Oxidation of Metals*, (Plenum, New York, 1965) p128.

18. K. Hoshino, R.S. Averback, H. Hahn, and S.J. Rothman, J. Mater. Res. **3**, 55 (1988).

19. M. Paljevic, and Z. Ban, J. Lessc. Met. **95**, 105 (1983).

20. K. Sugiyama, Y. Waseda, and S. Kudo, ISIJ International, **31**, 1362 (1991).

21. *CRC Handbook of Physics and Chemistry*, 64th ed., editted by R.C. Weast, M.J. Astle, and W.H. Beyer (CRC press, Boca Raton, Florida, 1984).

22. D.H. Kay, *Techniques for Electron Microscopy*, 2nd ed. (F.A. Davis, Philadelphia, 1965), Chap. 8.

23. O. Kubaschewski, C.B. Alcock, and P.J. Spencer, *Materials Thermochemistry*, 6th ed. (Pergamon Press, Oxford, 1993).

24. C. E. Birchenall, *Oxidation of Alloys* (American Society for Metals, Metal Park, OH, 1970), Chap. 14.

25. S.-G. Park, W.S. Liu, and M-A. Nicolet, J. Appl. Phys. **75**, 1764 (1994).

26. I. Barin, *Thermochemical Data for Pure Substances* (VCH Verlagsgesellschaft mbH, D-6940 Weinheim, Germany, 1989).

27. K. Sachs, J. Iron Steel Inst. **187**, 93 (1957).

28. Z. Zhuying, in *High Energy and Heavy Ion Beams in Materials Analysis*, edited by C. J. Maggiore, M. Nastasi, J.C. Barbour, and J.W. Mayer (Materials Research Society, Pittsburgh, 1990).

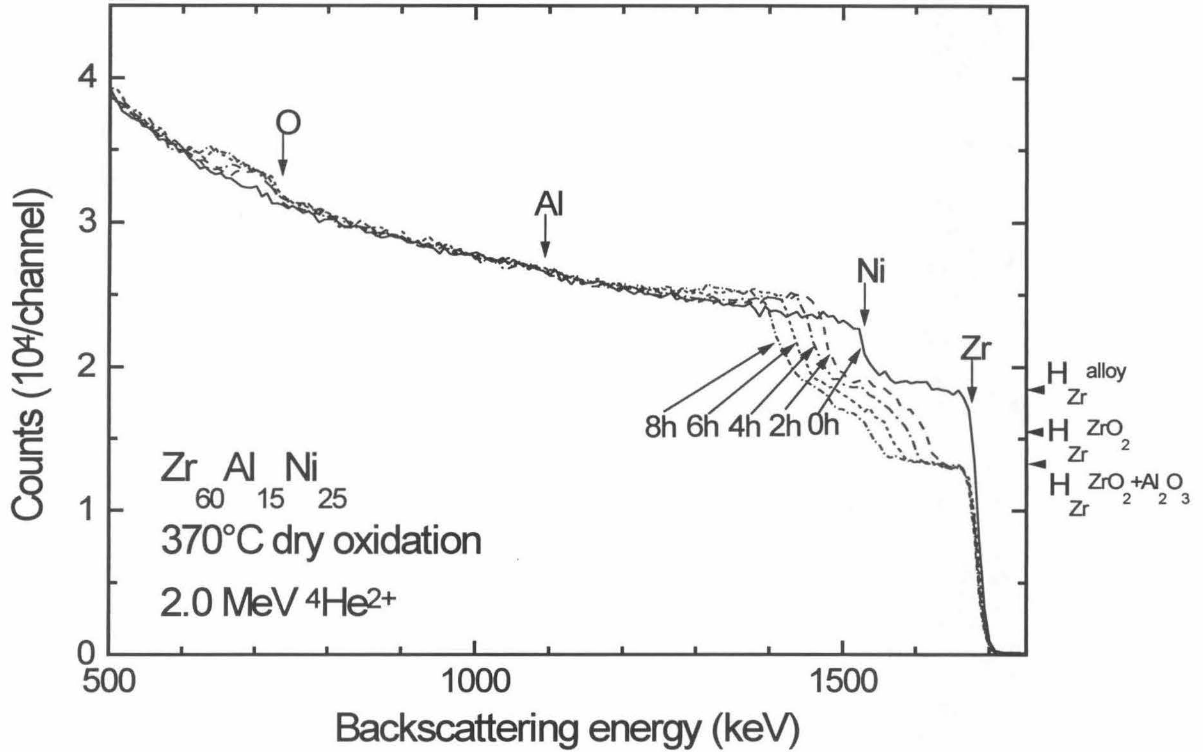


FIG. 1. Backscattering spectra of $Zr_{60}Al_{15}Ni_{25}$ amorphous foils before and after annealing in dry oxygen at 370 °C for various duration. (The incident beam is normal to sample surface; scattering angle of detected particles is 170 °) The levels marked on the right axis are explained in the text.

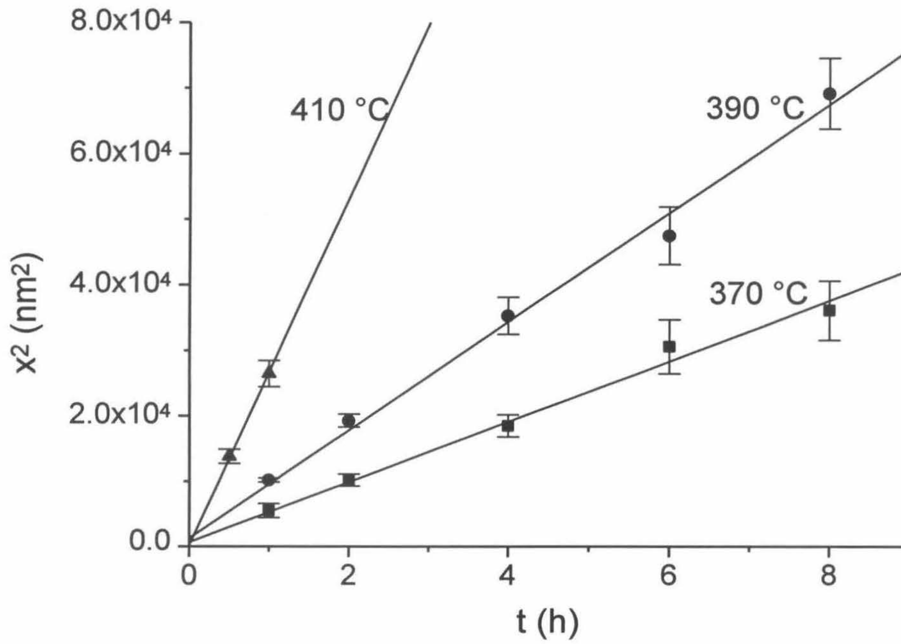


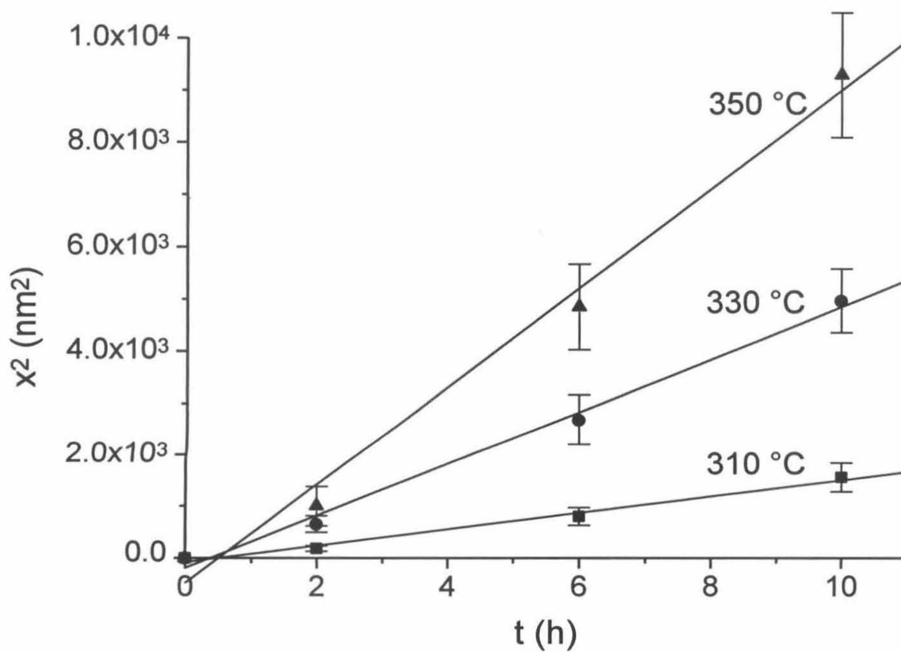


FIG. 2. The square of the oxide thickness, x, vs. oxidation duration at temperatures from 310 °C to 410 °C.

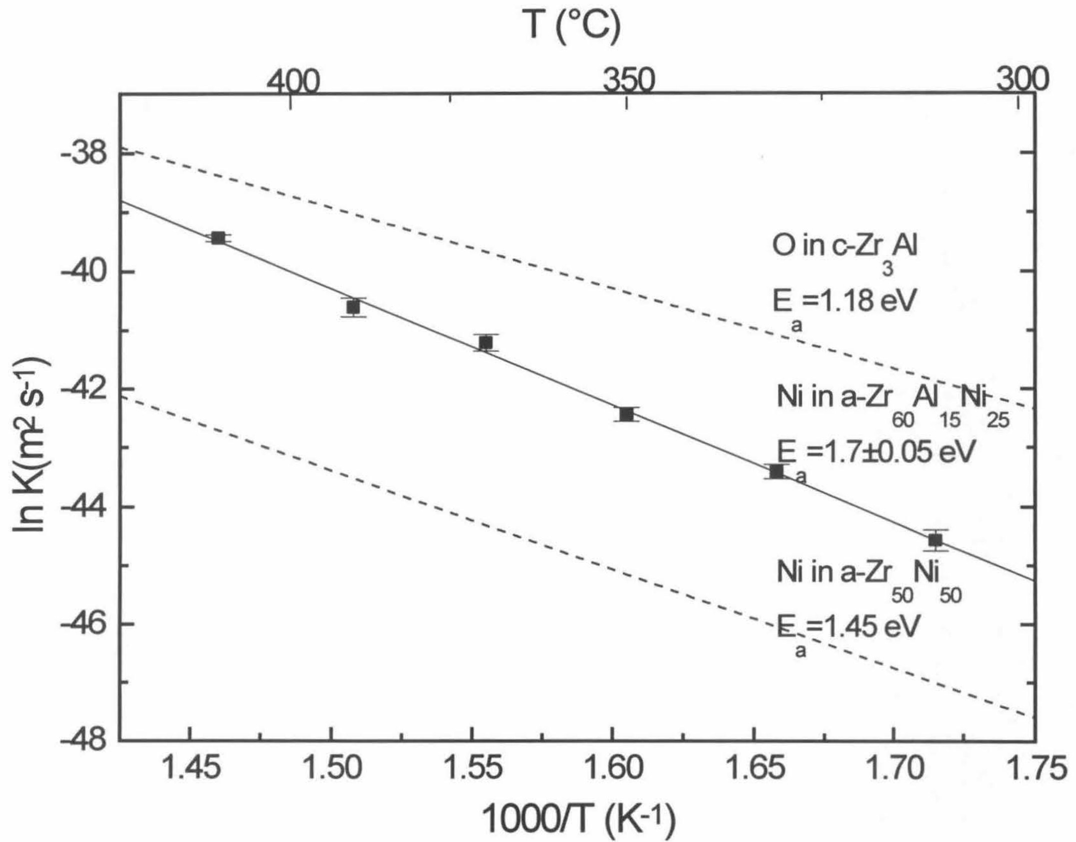


FIG. 3. Arrhenius plot of the transport constants obtained from Fig. 2 from 310 °C to 410 °C. Added for comparison as dashed lines are: (i) calculated values of the effective diffusion constants for Ni in amorphous $Zr_{50}Ni_{50}$ based on diffusivity data of Hoshino et al. [18], and (ii) experimental values for oxygen in the polycrystalline oxide of $Zr_3Al$ extrapolated from data of Paljevic at al. [19].

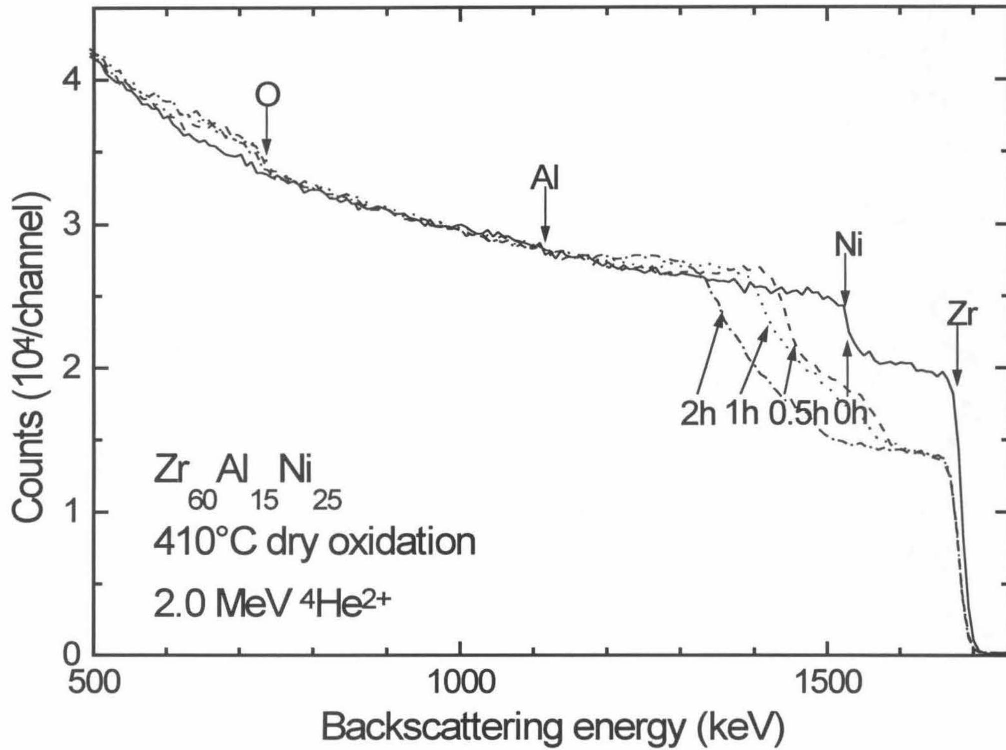


FIG. 4. Backscattering spectra of $Zr_{60}Al_{15}Ni_{25}$ amorphous foils before and after annealing in dry oxygen at 410 °C for various duration. (The incident beam is normal to sample surface; scattering angle of detected particles is 170 °)

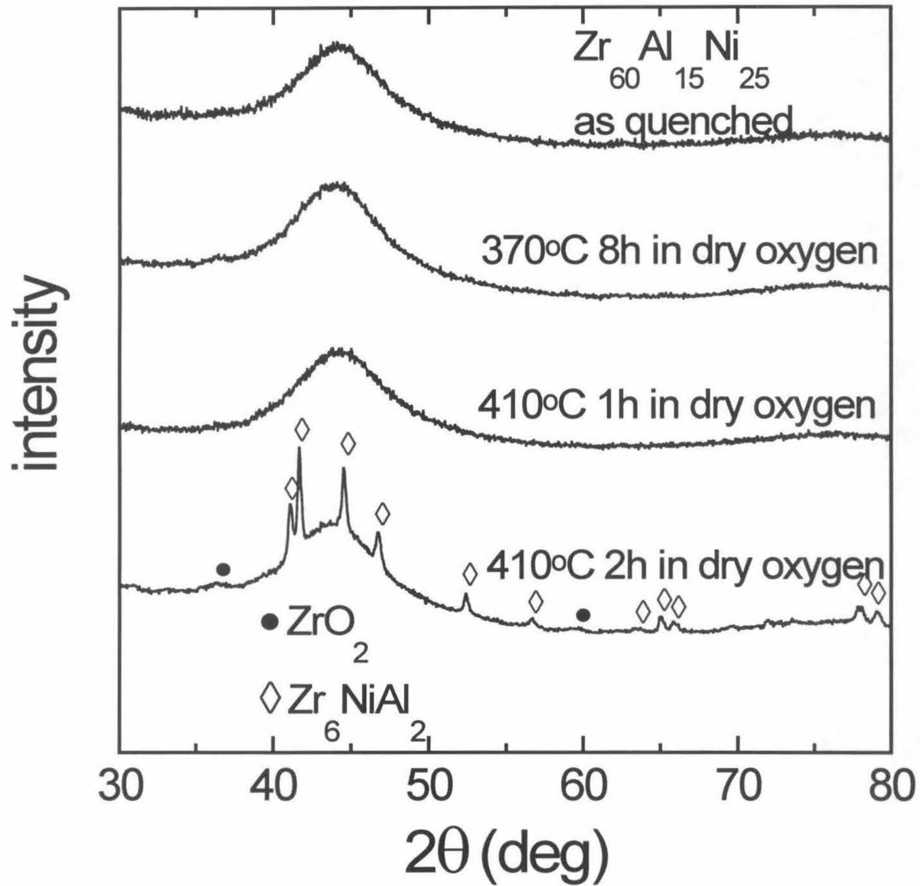


FIG. 5. X-ray diffraction spectra of foils before and after annealing in dry oxygen at 370 °C for 8h and at 410 °C for 1 h and 2 h. (Co $K_{\alpha}$, $\lambda = 0.179$ nm.)

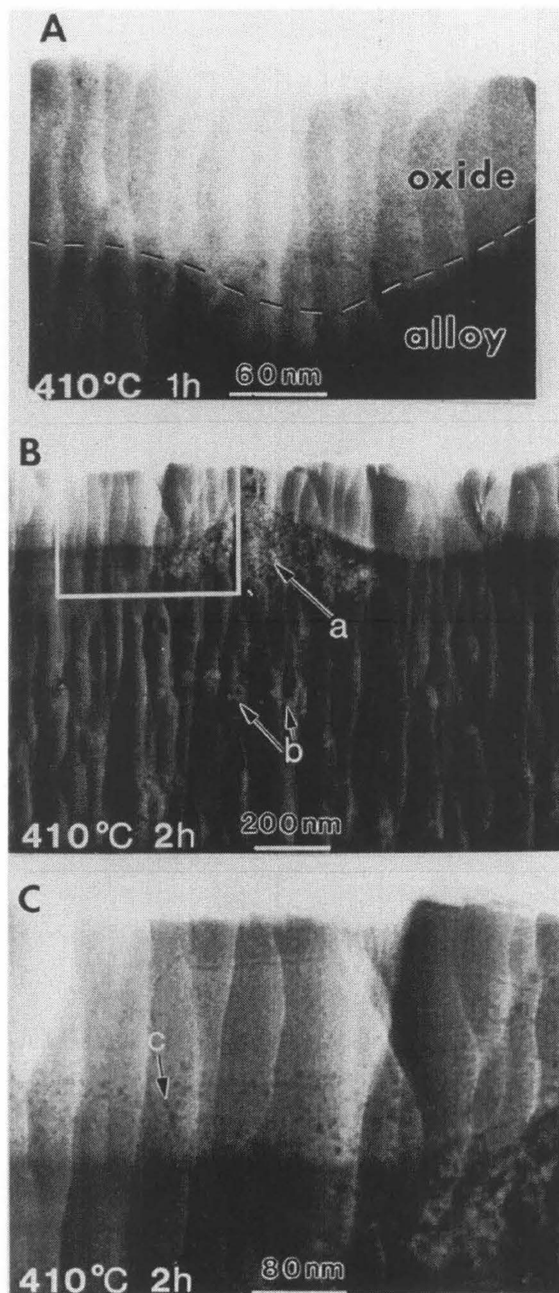


FIG. 6. Bright-field transmission electron micrographs of foils after annealing at 410 °C in dry oxygen for 1 h (A) and 2 h (B). Fig. C shows the framed area in Fig. B. Arrows used in Figs. B and C point to: a. a cluster of $Zr_5Ni_4Al$ nanograins at the interface, b. nanocrystalline $Zr_6NiAl_2$ phase inside the alloy, c. nanocrystalline $ZrO_2$ particles embedded in the amorphous oxide near the interface. The non-planar interface between the oxide and the alloy (dashed line in A) is an artifact of the sample preparation.

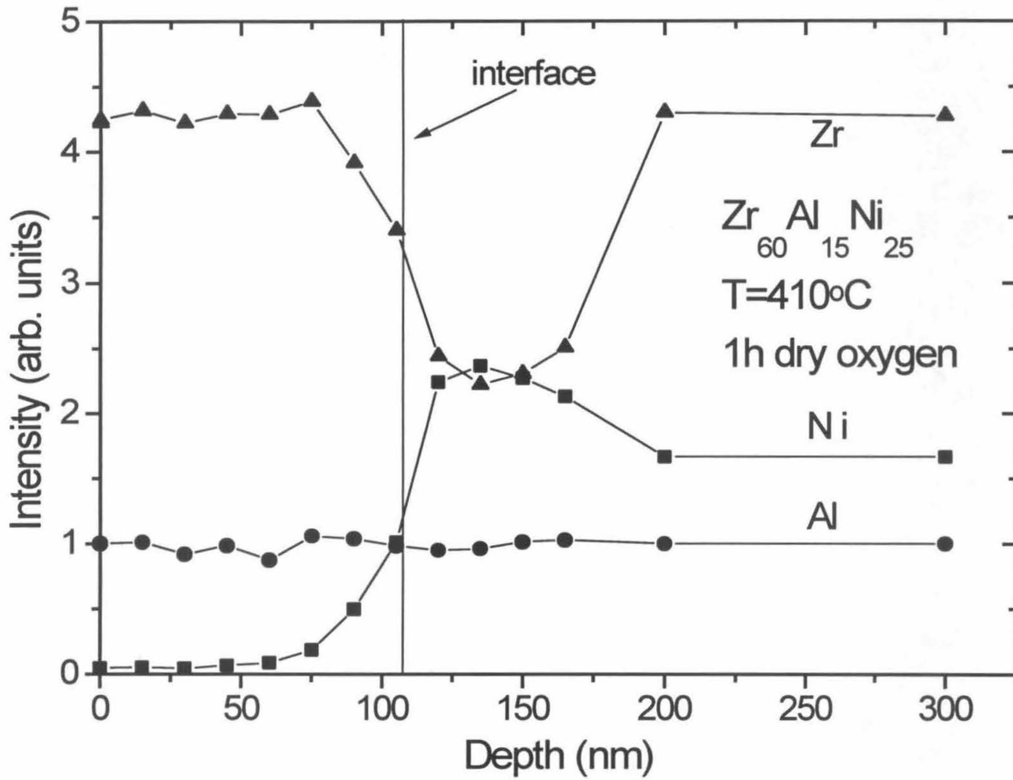


FIG. 7. Relative intensities of the $NiK_{\alpha}$, $ZrK_{\alpha}$ and $AlK_{\alpha}$ signals from energy-dispersive x-rays analysis as a function of depth for a sample annealed in dry oxygen at 410 °C for 1 h.

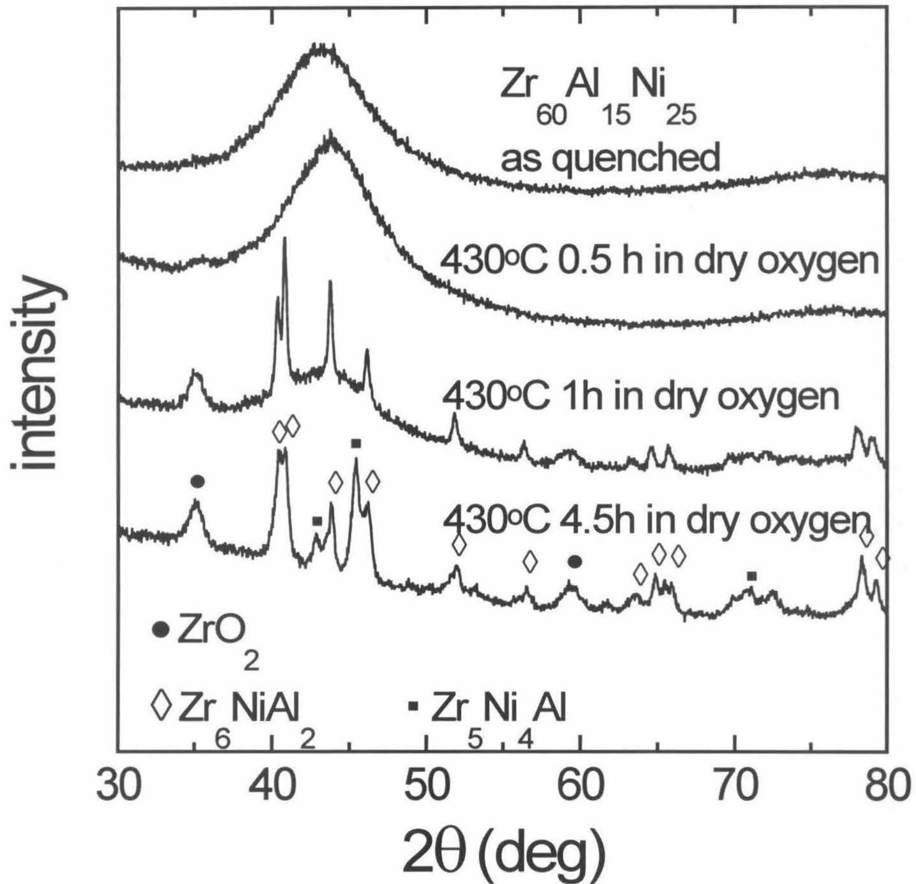


FIG. 8. X-ray diffraction spectra of foils before and after annealing in dry oxygen at 430 °C for 0.5 h, 1 h and 4.5 h. (Co $K_{\alpha}$, $\lambda = 0.179$ nm.)

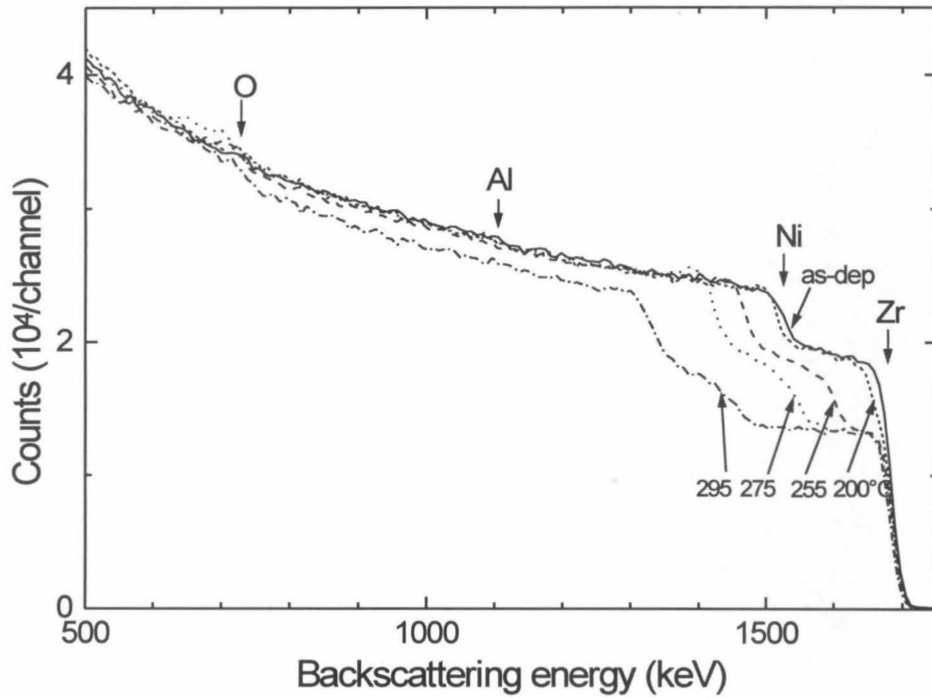


FIG. 9. Backscattering spectra of $Zr_{60}Al_{15}Ni_{25}$ amorphous foils before and after annealing in dry oxygen at 200-295 °C for 41 days. (The incident beam is normal to sample surface; scattering angle of detected particles is 170 °)

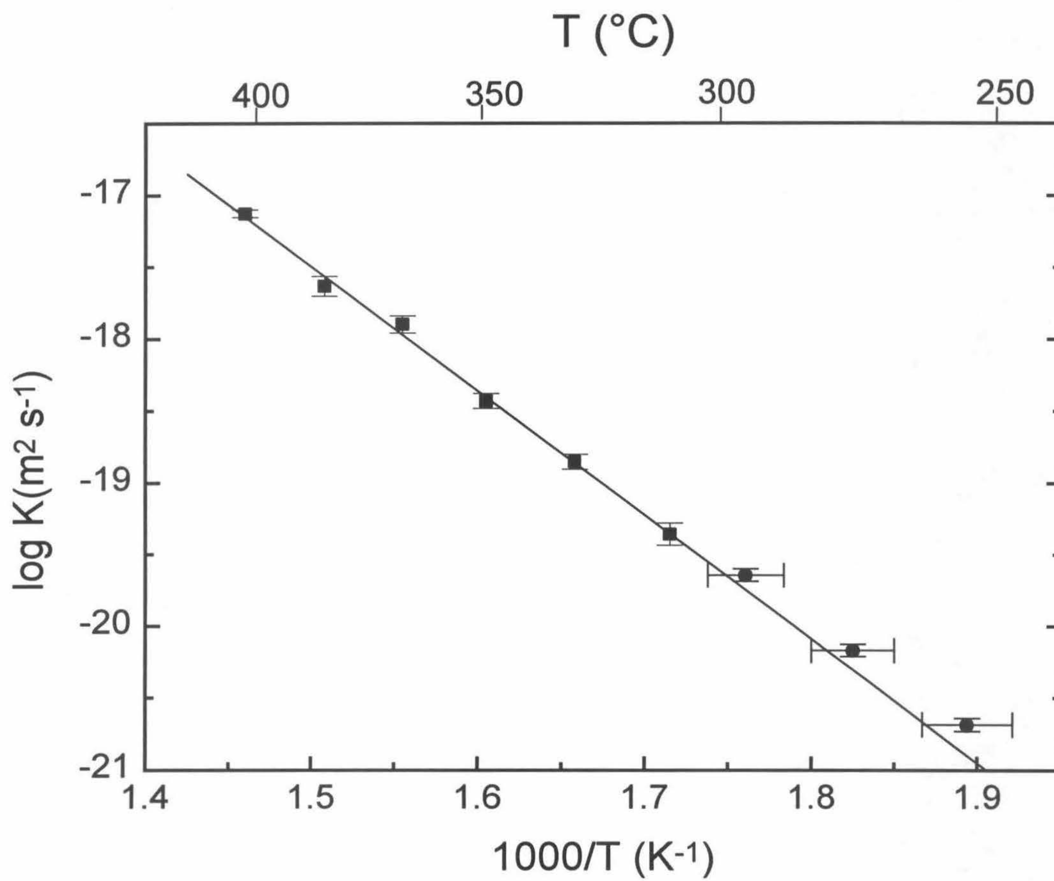


FIG. 10. Transport constants from 255 to 295 °C shown in the Arrhenius plot from 310 to 410 °C.

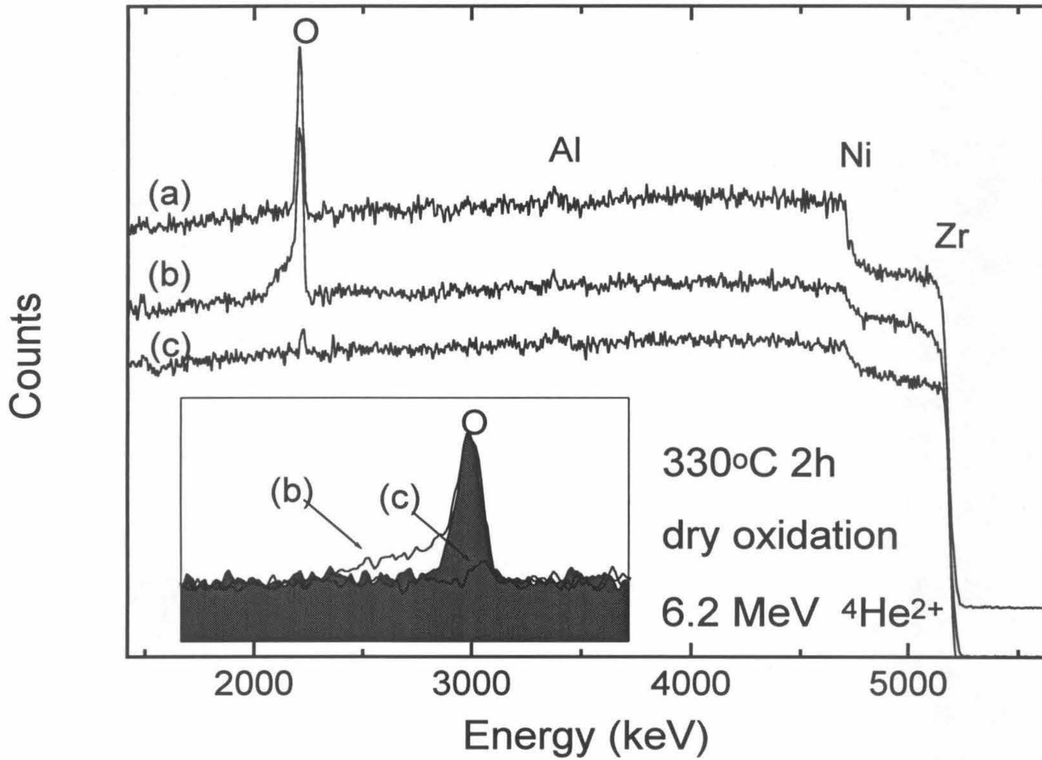


FIG. 11. 6.2 MeV $^4He^{2+}$ backscattering spectra (incident beam normal to sample surface, scattering angle of detected particles is 177 °) of amorphous foils $Zr_{60}Al_{15}Ni_{25}$ (a), and $Zr_{72.5}Al_{15}Ni_{12.5}$ (b), both annealed at 330 °C for 2 h in dry oxygen. For comparison, a spectrum of the as-prepared $Zr_{72.5}Al_{15}Ni_{12.5}$ sample is plotted in (c). The spectra are shifted vertically for clarity. The insert shows an enlarged portion of the unshifted spectra near the oxygen signal.